Loss mechanisms in hollow-core optical fibers

Eric Numkam Fokoua*, Seyed Abokhamis Mousavi, Gregory T. Jasion, David J. Richardson, and Francesco Poletti[1]

[1] *Optoelectronics Research Centre, University of Southampton, Southampton SO17 1BJ, United Kingdom*
* *Eric.Numkam-Fokoua@soton.ac.uk*

Abstract: Over the past few years, progress in hollow-core optical fiber technology has reduced the attenuation in these fibres to levels comparable to those of standard silica-core single mode fibers at telecom wavelengths. The sustained pace of progress has sparked renewed interest in the technology, and created the expectation that they will one day become the most transparent optical waveguides across all spectral regions. Here, we review and analyze the various physical mechanisms that drive attenuation in hollow-core optical fibers. We distinguish between the somewhat legacy hollow-core photonic bandgap technology and the more recent antiresonant hollow-core fibers. Since these two fiber types exploit different guidance mechanisms from conventional solid-core fibers to confine light in a hollow of gas-filled core, their propagation loss is also dominated by different phenomena, which we analyze in detail. We first discuss intrinsic loss mechanisms in perfect and idealized fibers. These include confinement or leakage loss, absorption and scattering within the gas filling or from within the glass microstructure surrounding the core, and roughness scattering from the air-glass interfaces within the fibers. The latter contribution is analyzed rigorously, clarifying inaccuracies in the literature where an inadequate scaling rule has often been used. We then explore the extrinsic contributions to loss and discuss the impact of random microbends, as well as that of other perturbations and nonuniformities which may result from imperfections in the fabrication process. These effects impact the loss of the fiber predominantly by scattering light from the fundamental mode into lossier higher order modes. Although often neglected, ensuring these contributions are minimized is important for realizing sub 0.1 dB/km loss hollow-core fibers. We briefly analyze the impact of macrobending and present general scaling rules for all loss mechanisms and combine them to examine the performance of recently reported fibers. We lay some general guidelines for the design of low loss hollow core fibers for operation at various spectral regions and conclude the paper with a brief outlook on the future of this transformative technology.

© 2022 Optical Society of America

Contents

List of Symbols and abbreviations

The following list describes several symbols and abbreviations that will be later used within the body of this manuscript:

α attenuation coefficient

β Propagation constant

κ Spatial frequency

$|\psi_k\rangle$ k^{th} optical mode supported by the fiber

λ Wavelength of light in vacuum

ω $= \frac{2\pi c}{\lambda}$, optical frequency

ζ material loss suppression factor

c Speed of light in a vacuum

k $= \frac{2\pi}{\lambda}$, vacuum wavenumber

u_{nm} m^{th} zero of the Bessel function $J_{n-1}(x)$

7c, 19c, 37c... hollow-core photonic bandgap fibers with seven, nineteen, thirty-seven, ... cells core defects respectively

ARF Antiresonant fiber

HCF Hollow-core fiber

MTF Mechanical transfer function

NANF Nested Antiresonant Nodeless Fiber

PBGF Photonic bandgap fiber

PSD Power spectral density

1. Introduction

A little over twenty years ago, it was reported for the first time that thirty five percent of light emitted from a laser had been successfully transmitted in the fundamental mode of a forty millimeter-long sample of a new optical fiber featuring an air-filled core [1]. This most exciting development was the first reported attempt at demonstrating that concepts of photonic crystals and associated photonic bandgaps could be exploited for light confinement and guidance in long and flexible hollow-core optical waveguides. Pioneering theoretical works by Yablonovich [2] and John [3] which inspired work on the fiber, had independently shown that dielectric structures incorporating three-dimensional wavelength-scale periodic refractive index distributions could inhibit the existence of certain photonic states (characterized by frequency ω and wavevector $\mathbf{k}$). In perfect analogy with the electronic bandgaps in solid-state physics, such structures would not permit even spontaneous emission due to the absence of allowed photonic states, and could thus be used to engineer strong localization of light within a purposely created defect [2, 3]. Adopting these concepts, it was shown that with a 2D periodic arrangement extending infinitely in a third dimension, an out-of-plane photonic bandgap could be realized and thus exploited for light guidance in a suitably engineered core defect. Such an out-of-plane bandgap was possible even with a refractive index contrast as low as that between air and silica [4, 5]. Because of this legacy of adapting concepts from photonic crystals, such fibers came to be known generically as photonic crystal fibers [6–8].

This first demonstration of light guidance in an air core sparked genuine optimism and ushered in an era of intensive research into hollow-core optical fiber technology. The enthusiasm for this technology was justified because light guidance in air either completely removes many of the material imposed limitations of conventional optical fibers, or suppresses them by several orders of magnitude, whilst uniquely enabling many novel photonics applications by virtue of some unique properties of their own [9, 10].

First, the absence of a solid material in the core greatly reduces the likelihood of the core of the fiber incurring damage by dielectric breakdown from high intensity radiation. At the same time, this also virtually eliminates the Kerr optical nonlinearity present in conventional solid-core optical fibers and vastly improves the power handling ability of hollow-core fibers, making them ideally suited for the delivery of high-energy, continuous wave or pulsed laser light [11–15]. The nearly three orders of magnitude lower optical nonlinearity implies the removal of the serious impediment of nonlinear noise in optical fibre telecommunications systems, a fundamental limitation to the data-carrying capacity of conventional fiber based systems [16, 17].

Secondly, by virtue of its group index being very close to 1, a hollow-core fiber guides light with near-vacuum latency, a property emerging as increasingly important in many data communications applications [18]. Indeed, low latency is advantageous for the deployment and functioning of 5G networks, where timing requirements are stringent [19–24], or in data centers and even supercomputers [25–28]. Moreover, as the optical field of the guided mode inside the hollow-core does not interact strongly with the solid material, the low latency is complemented by very low group velocity dispersion and is remarkably resilient to changes in the environment, particularly temperature [29–31]. This unique property makes hollow-core fibers ideal for applications in high precision interferometry, synchronization and time and frequency metrology [32, 33].

Thirdly, removing the solid material from the core of the fiber makes it an ideal platform for the study of light-matter interactions in liquid or gaseous phases, both in the linear and nonlinear regimes [34, 35]. Here, the long interaction lengths and the simultaneous confinement of light and fluid materials have led to the realization of many applications including frequency conversion [36], the generation of supercontinua [37], pulse shaping [38], etc. Low loss confinement of light in a hollow-core also opens up the possibility of levitating and guiding particles over long distances in such structures [39–41].

Most importantly however, the excitement about hollow-core fiber technology was largely born out of the hope that the removal of the solid material from the core of the fiber would result in lower propagation losses than achievable in standard single mode fibers. Attenuation in the latter is fundamentally imposed by Rayleigh scattering arising from density fluctuations characterizing the disordered nature of glass [42, 43]. Such disorder may be quantified through the the fictive temperature which is typically higher in fiber than in bulk silica [44]. Over the years, the gap between the fictive temperatures of bulk glass and fiber has narrowed significantly and it is now widely acknowledged that significant loss reduction below ~0.14 dB/km in silica fibers is unlikely. Further loss reduction must therefore employ a medium less susceptible to scattering and with its nearly three orders of magnitude lower density, air is the perfect such medium (and vacuum arguably an even better one). In addition to such low scattering, low-loss guidance in air/vacuum is possible at wavelengths where glass is opaque, if the fibers can be designed to avoid a strong overlap between the guided mode field and the solid material. This opens up prospects for low-loss optical guidance in spectral regions spanning from the UV to the mid-infrared, all on a single solid material platform. Despite all these promising prospects, achieving hollow-core fiber loss levels comparable to or lower than conventional fibers has proved a formidable challenge until recently [45].

Within a few years of the first report of a hollow-core fiber, researchers soon discovered that the physical mechanisms exploited to guide light in a hollow core introduce some unique loss mechanisms. First, unlike conventional fibers where total internal reflection ensures that the guided optical modes are truly confined, guiding light in microstructured fibers in general, and in hollow-core fibers in particular, is always accompanied by some leakage, i.e., the modes are leaky and a fraction of the optical power flows away from them as they propagates along the fiber axis [46, 47] . This leads to *leakage* or *confinement* loss, akin to what results for example from partial reflection when a conventional solid core fiber is bent and some of the light lost through refraction. One fundamental aspect of the leakage loss is that it increases with the order of the transverse mode, leading to differential loss between guided modes. Secondly, in hollow-core fibers, the presence of many air-glass interfaces gives rise to a unique *surface scattering* mechanism which contributes to loss. Researchers realized early on that in photonic bandgap fibers for example, these interfaces despite being extremely smooth (sub-nanoscale intrinsic roughness), can lead to substantial scattering loss when the mode propagates over long distances. This was found to impose a somewhat fundamental limit to the loss that can be achieved in these fibers [48, 49]. In the newer type of hollow-core antiresonant fibers, this contribution appears to no longer be the dominant one, but still plays a role in determining the total loss of the fiber.

In addition to these two distinct and unique loss mechanisms, other intrinsic loss mechanisms present in solid-core fibers also contribute to the loss of hollow-core ones. The first is *Rayleigh scattering* which may originate in the glass or in the hollow regions when they are filled with air or other gases. Rayleigh scattering from gases is nearly three orders of magnitude lower than in glass, making its contribution negligible. In hollow-core fibers, a very small fraction of the optical power is guided in the glass. This highly suppresses loss contributions from Rayleigh scattering within the glass regions. The second is *absorption* which may also originate in the glass or inside a potential filling gas. Like scattering, glass absorption is highly suppressed due to the small overlap between the guided mode field and the glass material. Absorption in potential filling gases depends on the specific gas composition and the operating wavelength, but can in principle be eliminated by evacuating the fiber.

A range of extrinsic loss mechanisms present in solid-core fibers also affect the loss of hollow-core fibers. For example, leakage loss increases when the fiber is bent or deployed in a coiled configuration for applications like sensors or interferometers. This is known as *macrobend* loss. When the fiber axis deviates locally from a straight path due to random lateral loads applied to it, for example when wound on a drum with a rough surface or pressing against a rough strength member in a cable, it incurs additional loss known as *microbending*. In addition to these bend-induced loss mechanisms, random fluctuations in the fiber manufacturing process result in small structural perturbations or non-uniformities of the fiber structure. As in solid-core fibers, the consequence of such perturbations is to cause intermodal power transfer between the core-guided modes and between these core-guided modes and radiation modes, leading to additional loss.

The aim of this article is to present as complete a picture as is currently possible of what is understood or indeed misunderstood about the physical mechanisms that contribute to loss in hollow-core fibers. The mechanisms providing the dominant contribution to loss are inextricably linked to the relevant guidance mechanism and fiber type. We will distinguish broadly between two families of fibers. The first guide light via a photonic bandgap effect, and here too, the distinction can be made between 1D photonic bandgap fibers whose cladding consists of an omnidirectional dielectric mirror [50], and 2D photonic bandgap fibers whose cladding features a two-dimensional periodic honeycomb-like structure [1]. The second family of fiber typically feature a cladding made of an arrangement of thin glass membranes and guide light via a mechanism known as antiresonance or often referred to as inhibited coupling [51, 52]. Whilst these may not encompass all types of hollow-core fiber, we focus on 2D photonic bandgap fibers and antiresonant fibers because of their demonstrated potential for sub 1 dB/km loss at wavelengths from the visible to the near infrared. We place greater attention still on antiresonant fibers which have been the focus of intense research in the last few years and have now demonstrated sub 0.2 dB/km loss in multi-kilometre spans [45]. We start with a brief overview of the current status of performance in both fiber types.

1.1. Current status of photonic bandgap fibers

In photonic bandgap fibers (PBGFs), the cladding region typically consists of a periodic arrangement of dielectric materials in the transverse direction. The choice of these dielectric materials and their arrangement determines the region of the space of photonic states, i.e the range of frequencies and wavevector $(\omega, \mathbf{k})$ in which the cladding does not support any state. This region is known as the photonic bandgap, in analogy with electronic bandgaps in solid state physics [2, 3]. When a suitable defect is introduced in this arrangement, for example to form the core of the fiber, it is able to support states which are not allowed in the cladding region and which therefore remain confined and guided along the fiber length.

A distinction can be made between fibers with 1D bandgaps, or so-called Bragg fibers and and those with 2D photonic bandgaps. In the former, the hollow-core is surrounded by a cladding consisting of alternating layers of two different materials, often with a high refractive index contrast, which provides omnidirectional reflectivity [50, 53]. Because of the requirement of high-index contrast and the small layer thicknesses needed for operation at visible or near infrared wavelengths, such fibers have been most successful for operation at longer wavelengths in the infrared, particularly at the 10.6 µm emission wavelength of CO2 lasers [50]. Excellent reviews into their properties can be found in [54]. Here however, we focus on fibers with 2D bandgaps and simply refer to them as hollow-core photonic bandgap fibers (HCPBGFs). In these fibers, the hollow-core is surrounded by a cladding consisting of a periodic array of air holes embedded in a silica matrix. Such fibers have been intensely researched for applications at wavelengths spanning from the visible to mid-IR. Some example of cross-sections images of photonic bandgap fibers reported in the literature are shown in Fig.1 and excellent reviews into how these fibers guide light and their key properties can be found in [9, 10].

It is now well understood that the cladding of HC-PBGFs which most often consists of a triangular lattice of hexagonally shaped air holes, is in fact made up of three *resonator* types which when isolated, support optical modes of their own (as characterized by $(\omega, \mathbf{k})$). These *resonators* are: the glass nodes which are the areas with concentrated glass mass between any three neighbouring holes, the interconnecting thin glass struts and the air holes themselves [10, 67, 68]. Figure 2 illustrates how the interaction between the modes of these resonators when brought together, leads to the formation of the photonic bandgap. The size of the nodes is key in determining the spectral position of the photonic bandgap, whilst their average spacing determines its width. When brought in close proximity, the modes of the individual nodes near cut-off overlap spatially with each other, leading to the formation of bands of allowed photonic states separated by regions of forbidden ones, in perfect analogy with energy band formations and energy gaps in lattices of closely spaced atoms [10]. In principle, when the arrangement of nodes is perfectly periodic, one expects multiple forbidden guidance regions. The addition of the thin glass membranes, necessary for physical support, however, modifies this simple picture by typically closing all but the fundamental bandgap of the nodes. The size of the resulting air holes determines how far below the air line the photonic bandgap extends. This now widely accepted interpretation of photonic bandgap formation has been called the photonic tight-binding model, again, in analogy with the same concept in solid state physics [9].

In the two decades following the first demonstration of light guidance in an all-silica hollow-core fiber, steady progress was made in the development of photonic bandgap fiber technology. The early challenge facing researchers was that of achieving uniform and regular microstructured claddings with sufficiently high air-filling fractions to support wide bandgaps and low-loss guidance. These steps allowed loss reduction from dB/cm levels to dB/m performances. In 2003, a team at Corning reported success in increasing the cladding's air filling fraction from below 50% to above 90%, resulting in the loss reducing to 13 dB/km at 1500 nm in a fiber with a core made by omitting seven unit cells (7c) at the centre of the structure [55].

It was thought at first that the attenuation in these fibers resulted from possible longitudinal variations of the structure which may lead to the loss of the bandgap and from the coupling to surface modes [69, 70]. It soon emerged, however, that surface scattering from the air-glass interfaces rather than the Rayleigh scattering as in conventional fibers, was the dominant loss

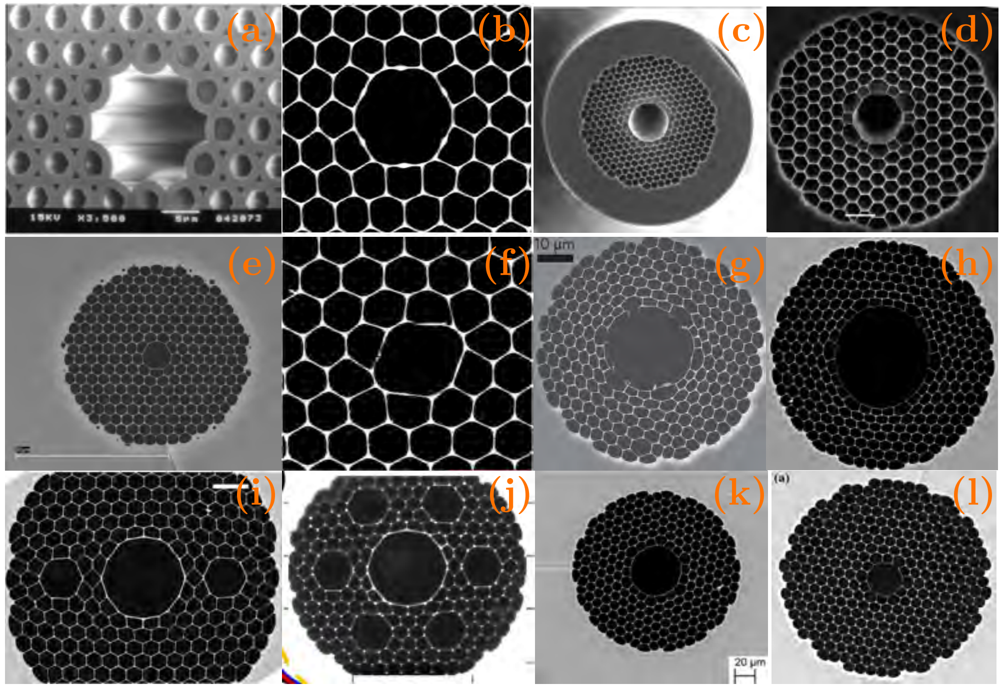

Fig. 1. Examples of photonic bandgap fibers from the literature. (a) First reported fiber from [1], (b) low-loss 7c fiber from Corning [55] (c) Low-loss 19c fiber from Mangan *et al*. [56] (d) Surface-mode free 7c fiber from Amezcua-Correa *et al.* [57]. (e) Single mode 3c bandgap fiber from Petrovitch *et al.* [58]. (f) highly birefringent 4c fiber from Chen *et al.* [59] (g) Surface-mode free 19c fiber from Poletti *et al*. [18] (h) First 37c fiber used for mode-division multiplexed data transmission [60–62]. (i) Polarization maintaining fiber [63] (j) 19c fiber with improved single-modedness [19] (k) Low-loss 19c fiber for mid-IR operation [64] (l) Commercially available 7c fiber from NKT photonics used by many research groups [65, 66]

mechanism and imposed fundamental limits on the achievable losses in these fibers [49, 56, 71, 72]. These surfaces possess intrinsic residual roughness of thermodynamic origin in the form of frozen-in thermally excited capillary waves, which is as fundamental as the density fluctuations giving rise to Rayleigh scattering in conventional fibers [49, 73]. Despite being extremely small (<0.1 nm roughness rms), this roughness was shown to be capable of causing dB/km level loss. Its fundamental nature implies it cannot be completely removed by current fabrication processes. Further loss reduction therefore required reducing the strength of the guided optical field at the air-glass interfaces. This was achieved by enlarging the core defect to remove nineteen unit cells (19c) and using a thick core wall, chosen to be in *antiresonance* at the wavelength of operation. This approach was successful and led to the lowest ever reported loss figures in these fibers, 1.2 to 1.7dB/km [49, 56, 71].

However, using such thick core boundary walls comes at the expense of reducing the operational bandwidth which narrowed to only ~20 nm due to the introduction of surface modes (these are lossy modes supported by the nodes or struts at the core boundary, see Section 2.4 and references [69, 70, 74]). Such narrow bandwidths severely limit the application prospects for these fibers [49, 56]. Theoretical and numerical work later indicated that the operational bandwidth of the fiber could be preserved with acceptable loss penalties if the core wall was approximately half the thickness of the cladding struts [57]. With this understanding and through further

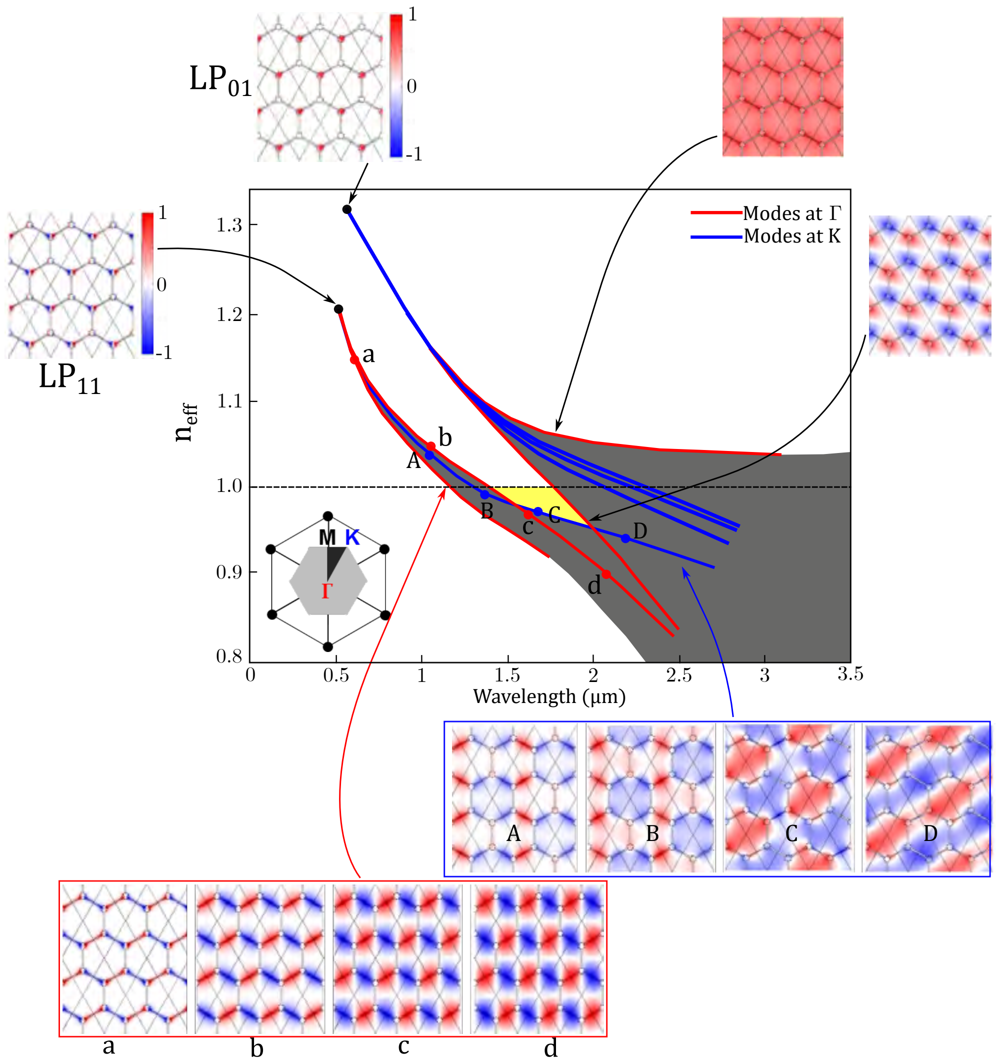

Fig. 2. Illustration of photonic bandgap guidance in a triangular lattice of holes cladding (adapted from [68]). At short wavelengths and above the light line ($n_{eff} = 1$), the *nodes* are effectively isolated and support discrete modes labelled LP here for simplicity. As the wavelength increases and the discrete modes in the nodes expand spatially, they start overlapping and forming bands of allowed states (grey areas). Near the light line ($n_{eff} = 1$) where the nodes modes are effectively at cut-off, the modes expand further, overlapping with the struts and air holes regions. However, the gap between the LP_{01} and LP_{11} bands in the nodes extend below the light line, forming the photonic bandgap region (yellow) where no states are allowed in the periodic structure but where an air-core can support guided modes.

improvements in increasing air-filling fractions, researchers at Bath reported a similar 7c fiber with a loss reduced to 9.5 dB/km [57]. This loss would later be reduced to 3.5 dB/km in a 19c fiber operating by our team at Southampton, over a bandwidth as large as 160 nm and this remains to date the fiber offering such a record combination of loss and operation bandwidth near 1550 nm [75]. Because of its unique features, this fiber was among the first to be used to demonstrate high-capacity, low-latency wavelength division multiplexed data transmission

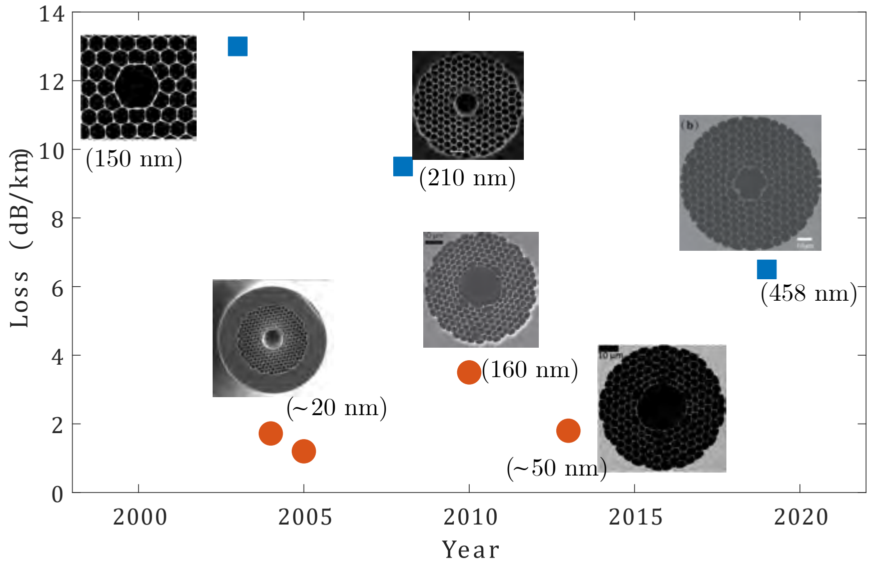

Fig. 3. Loss progression in hollow-core photonic bandgap fibers over the years. The blue squares indicate 7c fibers (From left to right [55], [57], [79]) and the orange dots 19c fibers (from left to right [49, 56], [75] and [80]). For each fiber, the number in the parantheses report the measured operational low loss bandwidth.

in a hollow-core fiber [18]. Along with these breakthroughs, remarkable progress was made in the fabrication of such fibers, with demonstrations of the ability to draw them in lengths up to 10 kilometres [76], aided by accurate modelling of the fluid dynamics of the fiber draw process [77, 78].

Enlarging the core of the fiber by removing a further ring of holes (18 unit cells) appeared to be the next necessary step to reduce the loss in these fibers beyond the reported figures. Reported fibers with 37c core sizes did not however achieve the expected lower losses [60]. Beyond the practical difficulty of controlling the fiber structure with such large cores, we believe that the role of other loss mechanisms, particularly of extrinsic origin such as microbending which become significant for larger core sizes, or the longitudinal variations of the structure (particularly its core), were not considered and had not yet been properly understood. Providing a comprehensive analysis that encompasses such contributions is the aim of this paper.

1.2. Current status of antiresonant fibers

After a few years of intense research into HCPBGFs, researchers at the University of Bath reported a hollow-core fiber that appeared to achieve $\tilde{d}$B/m loss levels over octave-spanning spectral bandwidths not expected if a photonic bandgap was the underlying guidance mechanism [51]. It would later emerge that unlike photonic bandgap fibers, these fibers with a Kagomé-like cladding relied on a combination of inhibited coupling to *low density of states* cladding modes and antiresonance from the thin glass membranes making up the cladding [34, 51]. One marked difference with photonic bandgap fibers as it was soon discovered, is that the addition of further rings of air-holes to the structure did not seem to reduce the loss of the fibers which numerical modeling showed was dominated by leakage or confinement loss [81, 82]. This realization led to many reports of fibers with effectively a single ring of air holes in the cladding but with relatively uncompromised loss performance [83, 84].

In this class of fibers, there is no accumulation of glass at the intersection of the thin membranes to form the *nodes* we identified as key for photonic bandgap guidance (except arguably on the core boundary where they have a negative impact on loss, see Section 2.4). Instead, the thin glass membranes themselves are the *resonators* that dictate the overall guidance in the fiber. When they are of equal thickness t and refractive index n, they are effectively transparent to resonant wavelengths given by [34]:

$$\lambda_m = \frac{2t}{m}\sqrt{n^2 - 1}, \; , m = 1, 2, 3, ... \tag{1}$$

Wavelengths between these resonances however, can be confined and guided in the core with low loss. In analogy therefore to Fabry-Perot interferometers where the condition under which reflectivity is optimal is called antiresonance, these fibers have been referred to as *antiresonant* fibers (ARFs), and we adopt this terminology throughout this paper.

In the years following their introduction, antiresonant fibers were perceived as generally suffering from much higher loss than the photonic bandgap fibers, although they offered wider, often octave-spanning operational bandwidths. Furthermore, the spectral loss of such fibers showed spurious loss peaks and dips across the transmission bands due to the relatively thicker nodes at the intersection of the membranes, particularly those on the core boundary [34,81,96,97]. A step change in this type of fiber occured when it was realized that the loss reduced substantially if the core boundary was such that these nodes were positioned far away from the center of the core, with the core boundary curved inwards, leading to the so-called hypocycloid core Kagomé fibers or negative curvature fibers [85]. Introducing such a core boundary design and combining it with the knowledge that further cladding rings of air holes did not play an important role in reducing the loss led to much simplified designs consisting of a single ring of cylindrical tubes, contacting at first and non-touching later [83, 86, 87]. Despite their simple structure, such antiresonant fibers have shown remarkable improvements in performance and are now outperforming photonic bandgap fibers on many accounts, including achievable attenuation and operational bandwidths. Excellent reviews into how these fibers guide light can be found in refs [35, 98–100] and Fig. 4 shows cross-sections of example antiresonant fibers reported in the literature.

In ARFs, scattering from surface roughness plays a minor role in determining the fiber attenuation because at antiresonant wavelengths, the electromagnetic field intensity near the air-glass interfaces is minimized due to destructive interference between incident and reflected waves on the thin glass membranes [71, 101]. This is the very same principle exploited to achieve the lowest loss to date in bandgap fibers, albeit at the cost of severely limited operational bandwidth due to the introduction of surface modes [49, 71]. In ARFs with noncontacting tubes however, no such penalty is present and scattering from surface roughness is low across all the available operational window. So far, loss appears instead to be dominated by contributions from confinement loss.

Figure 5 shows some examples of recently reported antiresonant fibers with minimum loss at wavelengths spanning from 500 nm to 5 µm. As can be seen, fibers with the simple cladding geometry made of non-contacting and non-nested tubes (henceforth referred to as tubular fibers) are in effect the most prevalent type and offer losses below that of pure silica at almost all wavelengths, except in the range from 800 nm to about ~2 µm. Loss in this spectral range is dominated by leakage. An important step for further confinement loss reduction in ARFs operating in this highly technologically relevant spectral region was a proposal to reduce the leakage loss by introducing nested tubes to enhance light confinement in the hollow-core [102]. At the same time, ensuring no contact points between the sets of nested tubes led to the seminal introduction of the nested antiresonant nodeless fiber or NANF concept [101]. Contact points, if present, would introduce spurious resonances with negative impact on loss . Two years after these theoretical proposals, a group in Beijing reported a fiber based on a similar concept of enhancing the reflection to lower the confinement loss [91], achieving a minimum loss of ~2 dB/km near 1512 nm, but still suffering from small spurious loss peaks due to the presence of small nodes in

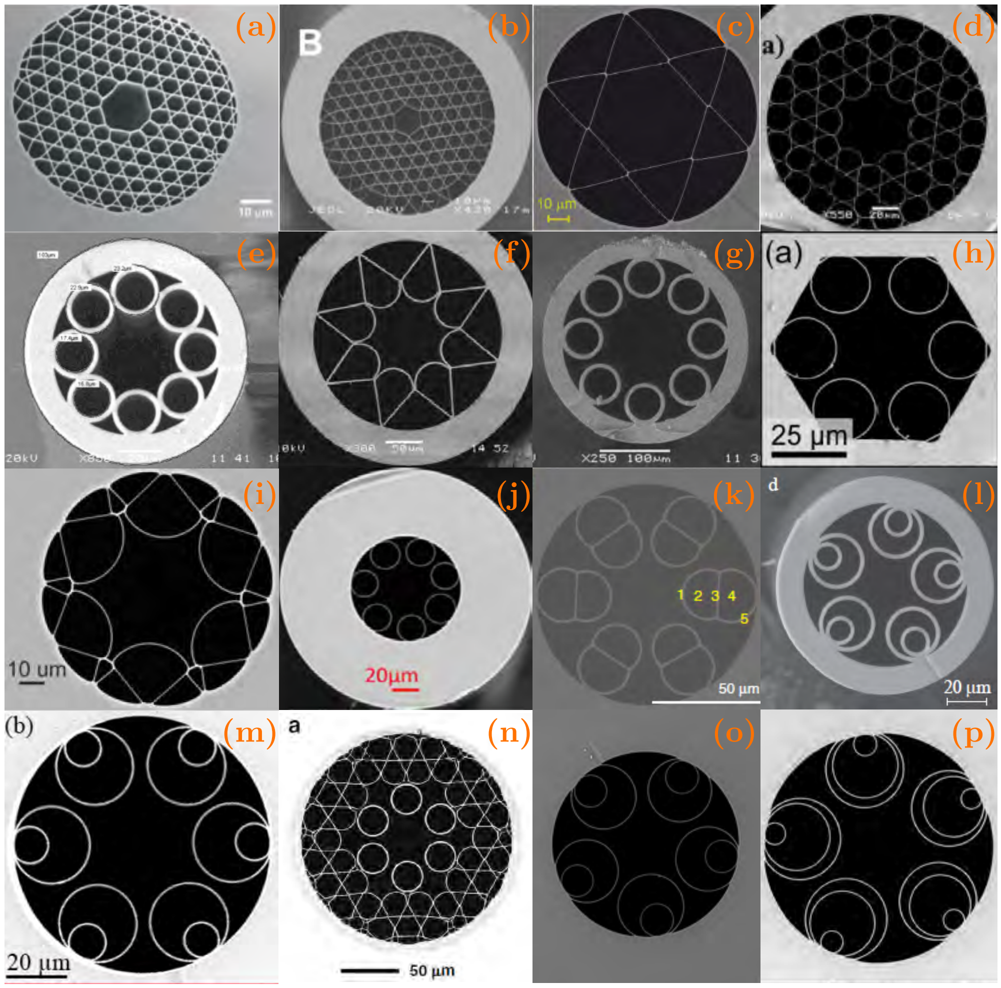

Fig. 4. Example antiresonant hollow-core optical fibers fro mthe literature: (a) Kagomé fiber from [51], (b) Large pitch single cell core Kagomé fiber from [34], (c) Antiresonant hexagram hollow-core fiber [84], (d) Hypocloid-core Kagomé fiber from [85], (e) Negative curvature fiber from [86], (f) Negative curvature fiber from [83], (g) *Revolver* hollow-core optical fiber from [87], (h) Effectively single mode 6-tube fiber from [88], (i) Lotus fiber from [89] (j) Low-loss tubular fiber with octave spanning bandwidth from [90], (k) Conjoined-tube fiber from [91] (l) Nested fiber from [92] (m) First sub dB/km NANF from [93] (n) Hybrid cladding fiber from [94] (o) Low-loss (0.22 dB/km) 5-tube NANF from [95] (p) Record low-loss double nested antiresonant fiber from [45]

the conjoined-tube design.

Subsequently, research efforts in producing NANFs have brought hollow-core ARF technology on the cusp of genuine breakthroughs. Their lowest attenuation now stands at 0.174 dB/km , 20% above that of pure silica core single mode fibers in the telecommunications C-band, but comparable to commercial germanium-doped core single mode fibers [45,95,109]. Furthermore, these fibers are now the most transparent fibers ever made in all other spectral regions including the visible, the important wavelengths of 850 nm and 1060 nm as well as in the mid infrared [110,111]. Such low loss values are ushering in an era of flexible, long length optical fibers and cables with near vacuum optical properties, something unachievable in conventional glass-core fibers.

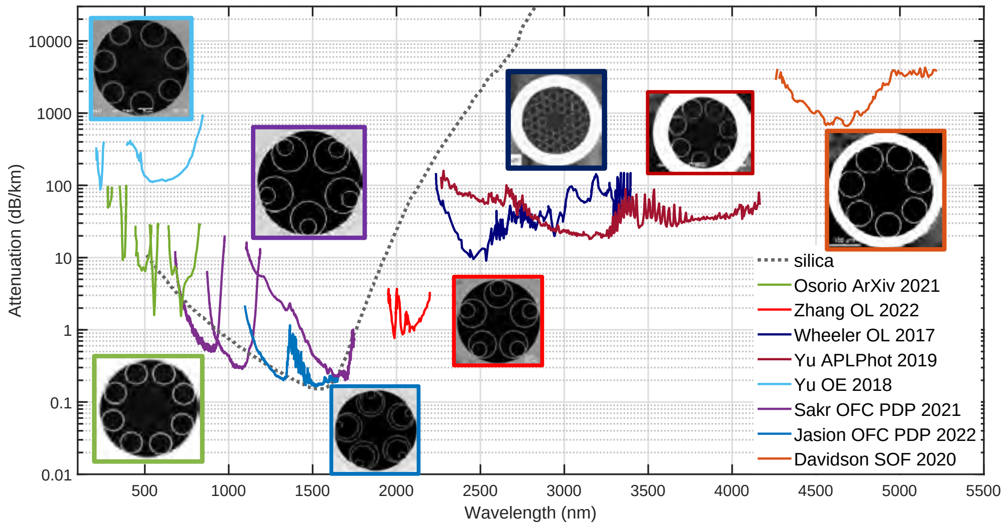

Fig. 5. Lowest loss antiresonant fibers reported in the literature. From left to right, cyan: Yu *et al.* [103], green: Osório *et al.* [104], purple: Sakr *et al.* [95], blue: Jasion *et al.* [45], red: Zhang *et al.* [105], dark blue: Wheeler *et al.* [106], dark red: Yu *et al.* [107], orange: Davidson *et al.* [108]. The dashed black line shows the loss of bulk silica for comparison.

The advent of such low losses has prompted a greater need for a deeper understanding of the mechanisms that will ultimately limit the attenuation in these fibers. Such a complete picture must encompass the known intrinsic loss contributions from leakage and surface scattering, and also take into account extrinsic loss mechanisms such as microbending as well as the coupling between fundamental and lossy higher-order modes arising from a range of perturbations along the fiber length.

The remainder of this paper is aimed at providing such a picture and is organized as follows: the first part discusses the *intrinsic* loss mechanisms where section 2 is devoted to confinement loss, reviewing its origins, interpretations and dependence on the guiding mechanisms. This is followed by a discussion of the material absorption in section 3. In sections 4 and 5, we discuss scattering contributions to loss, first from bulk contributions in either the glass or the gas within the hollow regions, followed by scattering from surface roughness. This first part is completed by a brief discussion of how these intrinsic mechanisms affect the higher order core-guided transverse modes and lead to mode-dependent loss in section 6. The second part explores *extrinsic* contributions to loss, starting with the impact of random microbends in section 7 and other potential random perturbations in section 8. In section 9, we discuss macrobend loss occurring when the fiber is deployed at a constant curvature diameter such as in a coil. In the final part of the paper, we bring all these contributions together to discuss the loss performance in state of the art hollow-core fibers in section 10 . The scaling rules derived throughout the paper are used to make projections for potentially achievable losses in antiresonant fibers in section 11. Section 12 presents our take on the future prospects of this exciting technology, followed by concluding remarks in section 13.

Part I
Intrinsic loss mechanisms

2. Confinement or Leakage loss

In standard solid-core single or multimode fibers, the core has a higher refractive index than the surrounding cladding and light is confined and guided in the core region by virtue of total internal reflection. This is known as index guiding. In a ray-optics picture, confined rays are incident on the core-cladding interface at an angle greater than the critical angle and therefore, as per Fresnel's law, undergo perfect lossless reflection. As a result, solid-core index-guiding fibers do not suffer from leakage loss. The situation changes however for higher order modes at wavelengths longer than their cut-off or when the fiber is bent. When this is the case, the rays only experience partial reflections at the core/cladding interface and thus suffer power loss due to refraction. These rays have been called leaky, and the associated loss is therefore termed leakage or confinement loss [112].

From the perspective of optical modes, the guided modes in such solid core fibers have real propagation constants β_k that satisfy $n_2 k_0 \leq \beta_k \leq n_1 k_0$, i.e., that must be larger than the wavenumber in the cladding with refractive index n_2. Therefore, they are strictly confined and not subject to leakage. Below a mode's cutoff frequency, some solutions to Maxwell's equations possess complex propagation constants, corresponding to fields that continuously lose power as they propagate [112, 113]. The confinement or leakage loss coefficient is then expressed as the imaginary part of the propagation constant:

$$\alpha(\text{dB/m}) = \frac{20}{\log 10} \Im(\beta) \tag{2}$$

In hollow-core fibers, perfect reflection at the *core/cladding boundary* does not occur. Regardless of the chosen guidance mechanism, hollow-core fibers typically have a silica jacket with a higher refractive index than the central hollow-core region. As a result, any core-guided mode has a lower propagation constant than the wavenumber in the outermost silica layer, and thus is subject to tunneling or leakage [54]. The guidance mechanism however, is crucial in determining the relative contribution this loss mechanism to the total loss of the fiber and in devising adequate strategies to reduce it. It is known for example that in photonic bandgap fibers, leakage loss can be reduced to arbitrarily low levels simply by adding further rings of air-holes in the cladding [47, 114]. In antiresonant fibers, a demonstrated route to loss reduction has been the addition of nested elements [101]. Below, we review the key physical insights to help understand the physical origin of this loss contribution in hollow-core fibers.

2.1. Understanding leakage loss as partial reflection

One of the ways in which leakage loss can be understood, regardless of the guiding mechanism involved, is by conceiving it as the result of partial reflection at the *boundary* between core and cladding. When this is the case, the residual refraction means that optical power radiates away from the core region. This interpretation from the ray optics picture implies that leakage loss in hollow waveguides can be estimated from an effective reflection coefficient at each reflection. To illustrate this interpretation, we consider the simplest hollow-core fiber possible, a circular hollow region surrounded by an infinitely extending dielectric region first studied by Marcatili and Schmeltzer [115] (see Fig. 6. Let us consider such a waveguide made of an air-filled core of radius a surrounded by silica. When $a \gg \lambda$ (λ is the wavelength), the real part of the propagation constant for the EH_{nm} mode is given as [115]:

$$\Re(\beta_{mn}) = \frac{2\pi}{\lambda}\left\{1 - \frac{1}{2}\left(\frac{u_{nm}\lambda}{2\pi a}\right)^2\right\} \tag{3}$$

where u_{nm} the mth zero of the Bessel function of the first kind $J_{n-1}(x)$. From the real part of the propagation constant, one works out that the incidence angle of corresponding light rays is simply:

$$\theta_i = \frac{\pi}{2} - \arccos\frac{\mathcal{R}(\beta_{nm})}{k_0} \simeq \frac{\pi}{2} - \left(\frac{u_{nm}\lambda}{2\pi a}\right). \tag{4}$$

Here, $k_0 = 2\pi/\lambda$ is the free-space wavenumber. After some simple algebra, one can show using Fresnel's equation that for this incident angle when the ray is s (therefore TE) or $p-$polarized (TM), the power reflection coefficient per reflection is:

$$R_s \approx 1 - \frac{4}{\sqrt{n^2-1}}\left(\frac{u_{nm}\lambda}{2\pi a}\right) \tag{5}$$

$$R_p \approx 1 - \frac{4n^2}{\sqrt{n^2-1}}\left(\frac{u_{nm}\lambda}{2\pi a}\right) \tag{6}$$

where n is the refractive index of the glass material. A meridional ray with the incident angle above undergoes a number N of reflections per unit distance given by:

$$N = \frac{\tan\left(\pi/2 - \theta_i\right)}{2a} \approx \frac{u_{nm}\lambda}{4\pi a^2} \tag{7}$$

Combining the equations above, one finds that the linear power loss coefficient per unit length of the ray is simply:

$$\alpha_s = -N\log(R_s) \approx \left(\frac{u_{nm}}{2\pi}\right)^2 \frac{\lambda^2}{a^3}\frac{2}{\sqrt{n^2-1}} + O(\lambda^3/a^4) \tag{8}$$

$$\alpha_p = -N\log(R_p) \approx \left(\frac{u_{nm}}{2\pi}\right)^2 \frac{\lambda^2}{a^3}\frac{2n^2}{\sqrt{n^2-1}} + O(\lambda^3/a^4) \tag{9}$$

From this simple picture of partial refraction, we are thus able to reproduce exactly the expressions derived by Marcatili and Schmeltzer obtained through solving Maxwell's equations [115], giving credence to this intuitive understanding of leakage loss. The same treatment above also reproduces exactly expressions derived for a dielectric tube waveguide [116] and by extension those from a multilayered model structure with l alternating glass/air layers as examined by Bird [117] which state that to the leading order,

$$\alpha_{TE}(dB/m) = \frac{20}{\ln 10}\left(\frac{u_{nm}}{2\pi}\right)^{l+2}\left(\frac{1}{\sqrt{n^2-1}}\right)^{l+1}\left(\frac{\lambda^{l+2}}{a^{l+3}}\right)\prod_{i=1}^{m}\frac{1}{\sin^2(\phi_i)} \tag{10}$$

$$\alpha_{TM}(dB/m) = \frac{20}{\ln 10}\left(\frac{u_{nm}}{2\pi}\right)^{l+2}\left(\frac{n^2}{\sqrt{n^2-1}}\right)^{l+1}\left(\frac{\lambda^{l+2}}{a^{l+3}}\right)\prod_{i=1}^{l}\frac{1}{\sin^2(\phi_i)} \tag{11}$$

where ϕ_i are the transverse phase accumulated across each successive layer labelled i. The loss of hybrid modes is the average of the two. From these expression, the hollow dielectric

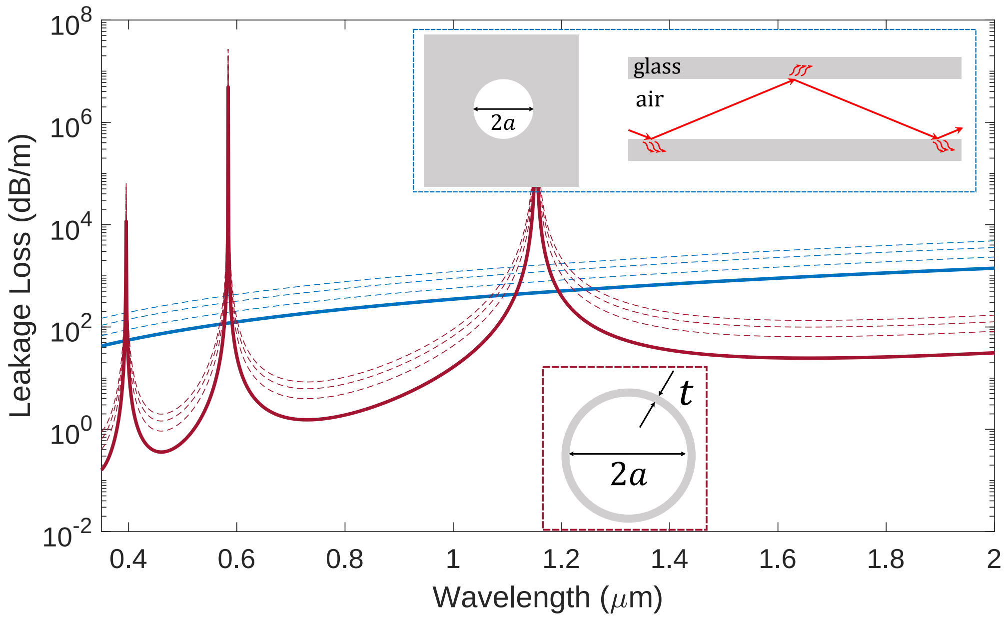

Fig. 6. Leakage loss from a hollow dielectric waveguide and dielectric tube waveguide estimated through the prism of partial reflection at the air/glass interfaces. The solid lines show the loss of the lowest loss LP_{01}-like mode and the dashed lines the calculated loss for the LP_{11}-like modes (the TM_{01} is the highest loss mode, the HE_{21} modes are degenerate and the TE_{01} has the lowest loss.

waveguide of Marcatili would correspond to $l = 0$ and a thin tube to $l = 1$. We plot in Fig.6 the confinement loss for the fundamental mode (solid colored curves) and LP_{11} like modes (dashed lines) for the hollow dielectric waveguide and a silica tube of thickness $t = 550nm$. Note how for the tube, the loss show the resonance peaks described by Eq.(1), corresponding to $\phi_1 = 2\pi t\sqrt{n^2 - 1}/\lambda = m\pi$ [117].

Whilst these model structures are only simplifications of practical fibers, they convey some important features of the loss properties in hollow-core fibers. The first is that leakage can be made arbitrarily low by increasing the core size. This comes, as we shall see, at the cost of the fiber supporting an increasingly high number of modes and a dramatic increase in bend-induced penalties. Secondly, leakage loss for higher order modes is higher than that of the fundamental mode. In the simple ray optics picture, the corresponding light rays are incident on the core cladding interface with increasingly more oblique angles and this is reflected in the analytical expression through the loss scaling as u_{nm}^2 ($u_{nm} = 2.4048, 3.8317, 5.1356, 5.5201, 6.3802, \ldots$). Thirdly, the polarization of the modes is important as the loss of TM modes is n^2 times higher than that of the TE modes of the same order. Finally and more importantly, higher reflectivity coefficients of the cladding can lead to much lower losses. In photonic bandgap fibers, the reflectivity generally increases with the number of cladding rings, reaching unity when infinitely many rings are incorporated. The same holds in antiresonant fibers too. From the model structures studied by Bird, we see from Eqs.(10) and (11) that the addition of more antiresonant layers leads to reduced loss. In practical fibers, this takes the form of additional nested tubes such as in the NANF, or further reflective layers such as in the conjoined tube structures lead to orders of magnitude lower losses.

2.2. Coupling/inhibited coupling interpretation

It has recently been shown that with knowledge of the reflectivity of a given cladding design (which one can only calculate numerically for more complex designs), the simple ray optics formalism above can give accurate predictions of the leakage loss of the fiber [118]. However, despite its appealing simplicity, the ray picture does not capture all of the intricacies of leakage loss and its dependence on fiber parameters in most practical cases. This is exacerbated by the fact that the reflectivity of the cladding in most cases can only be obtained numerically, making it difficult to easily draw useful conclusions such as the dependence of loss and mode-dependent loss on fiber parameters.

An alternative interpretation, also credited as key to the guiding mechanism in antiresonant fibers, is the so-called inhibited coupling interpretation [34, 119]. Here, the complex structure of a hollow-core fiber is regarded as an arrangement of different *waveguides* which would support their own modes with defined propagation constants and loss when isolated. These *waveguides* are the central hollow-core, the cladding structure which may be further subdivided into its own constituent waveguides, and the surrounding silica jacket. Let us refer to these modes as $|\psi_{\text{core}}\rangle$, $|\psi_{\text{cladding}}\rangle$ and $|\psi_{\text{jacket}}\rangle$, respectively. A low-loss core-mode propagating alongside the continuum of lossy and leaky cladding and jacket modes has been likened to the quantum mechanical concept of bound state in the continuum [120, 121]. Let us now assume that a core mode $|\psi_k\rangle$ propagates alongside a cladding or jacket mode $|\psi_l\rangle$ which has loss coefficient α_l. In this case, a coupled mode theory formalism has been invoked to show that for sufficiently long propagation distances, the core mode suffers additional loss given by [69, 70]:

$$\alpha \propto \frac{\alpha_l |\kappa_{k,l}|^2}{(\Delta\beta_{k,l}/2)^2 + |\kappa_{k,l}|^2} \tag{12}$$

where $\Delta\beta_{k,l}$ is the difference between the propagation constants of the core and cladding modes and $\kappa_{k,l}$ is a coupling coefficient or overlap integral between their corresponding mode fields. One can therefore postulate that if were to know the loss and propagation constants of all the cladding modes, the leakage loss of a core mode labelled p could be written as a superposition of the losses due to coupling to cladding and jacket modes:

$$\alpha_k = \sum_l \frac{\alpha_l |\kappa_{k,l}|^2}{(\Delta\beta_{k,l}/2)^2 + |\kappa_{k,l}|^2} \tag{13}$$

where the summation is across all the discrete cladding modes and takes the meaning of an integral when such modes form a continuum.

Despite their almost deceptive simplicity, these expressions offer a powerful insight. First, if core and lossy cladding modes possess a similar propagation constant, i.e. $\Delta\beta \sim 0$, then as long as the coupling between the two is not zero, the loss of the core mode tends asymptotically towards the loss of said cladding mode. This offers the prospect of designing cladding features to strip out undesired higher order core modes for example, by engineering them so that they support lossy modes with the same propagation constant as undesired the core mode under consideration. This is the underlying principle used to achieve effective single-mode operation in bandgap structures [122–125], and in antiresonant fibers [88].

Secondly, the propagation of a core mode is unaffected by the presence of lossy cladding modes, even if they have the same phase constant, provided their coupling strength κ is zero. Since the coupling between core and cladding modes is related to a spatial overlap integral, it is apparent that if the modes are highly localized, i.e., they occupy different regions of the cross-section with vanishing overlap between the tails of their transverse profiles, then the core mode cannot be affected. This is the case for example in photonic bandgap fibers. The periodic cladding supports no modes with the same propagation constant as the core modes, however, some radiation modes of the silica jacket fulfill this condition. More rings of air-holes outside the core ensures sufficiently large physical distance between the core and jacket, allowing the tail of the core modes to decay substantially, thereby limiting their overlap, resulting in confinement loss being negligible. The coupling integral can also be drastically reduced and made vanishingly small if the transverse phase profile of one of the modes changes very rapidly whilst that of the other does not, in effect rendering the modes orthogonal. This, it has been argued, is the case for example when the innermost boundary of the core in kagomé fibers is curved so as to look convex from the core [85, 121, 126–128]. The introduction of such a *negatively* curved core boundary indeed resulted in dramatic loss reduction in this type of fiber [85]. We note however that an important feature of such a core boundary is that it pushes glass *nodes* at the core boundary away from the center of core, thereby significantly reducing the overlap between core modes and the lossy modes localized therein. This effect is the same as the dramatic loss reduction in going from a cladding formed of contacting thin glass tubes to non-contacting ones, removing entirely the local glass *nodes* [101].

Whilst conceptually straightforward, the great difficulty in estimating the loss of the fiber using the expressions above lies in the fact that a large number of modes, which cannot be obtained analytically in any practical case, must be included for an acceptable approximation. In most cases, the difficulty and computational cost in obtaining those modes is greater than that of solving numerically for the leakage loss directly. Yet, the physical insight is of paramount importance in improving fiber designs.

2.3. Dependence on guidance mechanism and cladding design

The extent to which leakage contributes to loss in hollow-core fibers is inextricably linked to the adopted guidance mechanism. For the remainder of the paper, we will focus on 2D photonic bandgap and antiresonance guiding fibers. Specifically, we will often compare side by side the performance of a model photonic bandgap fiber with a nineteen cell (19c) core defect and a model NANF with the same core diameter. The structural parameters for these illustrative examples used throughout the paper are described in Fig.7.

In photonic bandgap fibers, increasing the number of cladding rings outside of the hollow-core is an effective way of reducing the confinement loss to arbitrarily low levels. As a rule of thumb, each additional ring of cladding air holes reduces the leakage loss by an order of magnitude, which can thus in principle be reduced to zero exactly if an infinite number of cladding rings are included. However, the number of cladding rings required to keep the leakage loss at a negligible level is highly dependent on the size of the core and key structural parameters of the cladding, namely the thickness of the glass struts in the cladding and the size of the glass nodes [10, 47, 80, 114]. The interpretation of leakage loss as emanating from coupling between core and lossy cladding modes offers a helpful insight here. Thicker cladding struts make the demarcation between *nodes* and struts difficult. They support modes with higher effective index at the bottom of the bandgap (see Fig.2), resulting in effect in shallower and narrower photonic bandgaps and therefore a reduced $\Delta\beta$ between the fundamental core mode and lossy cladding modes. It can be understood alternatively as thicker cladding struts providing more direct pathways for the fields of the core modes to overlap with the cladding radiation modes, thus resulting in loss. To illustrate this point, we show in Fig.8 the confinement loss calculated for the fundamental mode in two different photonic bandgap fibers with a nineteen cell core defect (henceforth 19c). Both fibers have the same core diameter and air-filling fraction. The first is the structure described in Fig.7 and in the second, the struts are twice as thick, with the size of the cladding nodes adjusted so that the toal mass of glass in the cross-section is conserved. One can see that with this small readjustment of the cladding structure, the second fiber with thicker struts has a remarkable four orders of magnitude higher confinement loss and a narrower operating bandwidth.

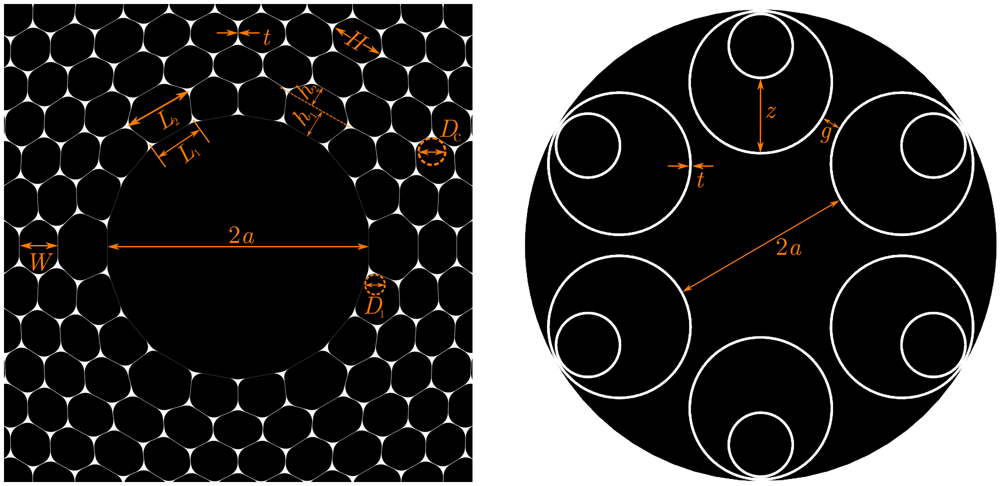

Fig. 7. Structural parameters of the example photonic bandgap fiber (PBGF, left) and NANF (right) used throughout the paper. The structure of the PBGF is optimized for low loss operation as described in [129]. Its key parameters are a core diameter $2a = 29.6\mu m$, an average cladding strut thickness $t = 47nm$, average cladding hole width $W = 4.7\mu m$ and average cladding hole fillet diameter $Dc = 0.63W$. The nodes on the core boundary are equidistant to give the core an almost circular shape and the core wall is half as thick as the cladding struts. For the NANF, we use a core diameter $2a = 30\mu m$, a cladding membrane thickness $t = 550nm$, a gap between the large tubes $g = a/5 = 3\mu m$ and the size of the first cladding cavity $z = 0.8a$.

In antiresonant fibers, particularly the widely used tubular and nested variety, away from the resonant wavelengths in the thin glass membranes at which the loss is sharply peaked (as shown in Fig.6) and away from anticrossing events discussed in the following section, leakage is mediated by the coupling to modes located in the air regions either enclosed by the tubes or the spaces between them, which can easily escape to radiation due to the physical contact with the glass jacket. This important insight provides an explanation as to how the leakage loss can be reduced further or increased for undesirable higher order core modes. By choosing the size of cladding tubes so that the $\Delta\beta$ between their modes and that of a higher order core mode is near zero, extremely high loss can be imposed on said higher order core modes often resulting in effectively single-mode operation as explored in many prior publications [88, 130, 131]. On the other hand, by partitioning these hollow regions of the cladding and making them smaller, the modes they support would have a larger $\Delta\beta$ with the core modes, resulting in lower leakage loss for the core modes [132]. We plot in Fig.9 the confinement loss calculated for two ARFs with 30 µm core diameter. The first is a tubular fiber with a cladding made of 7 non-contacting tubes and the the second fiber is the NANF whose parameters we described in Fig.7. Both fibers have the same core diameter, gaps between outer tubes and membrane thickness. The computed confinement loss is shown here across the fundamental antiresonance window, i.e wavelengths longer than the first resonance at 1.1 µm . We can see how the addition of the nested tube results in a dramatic reduction in leakage loss.

2.4. Role of modal anticrossings

In hollow-core fibers, the termination of the *cladding* around the central core plays a vital role in determining the leakage loss of the fiber. This is because such a core *boundary* may support optical modes with similar propagation constant to the core modes and which easily radiate

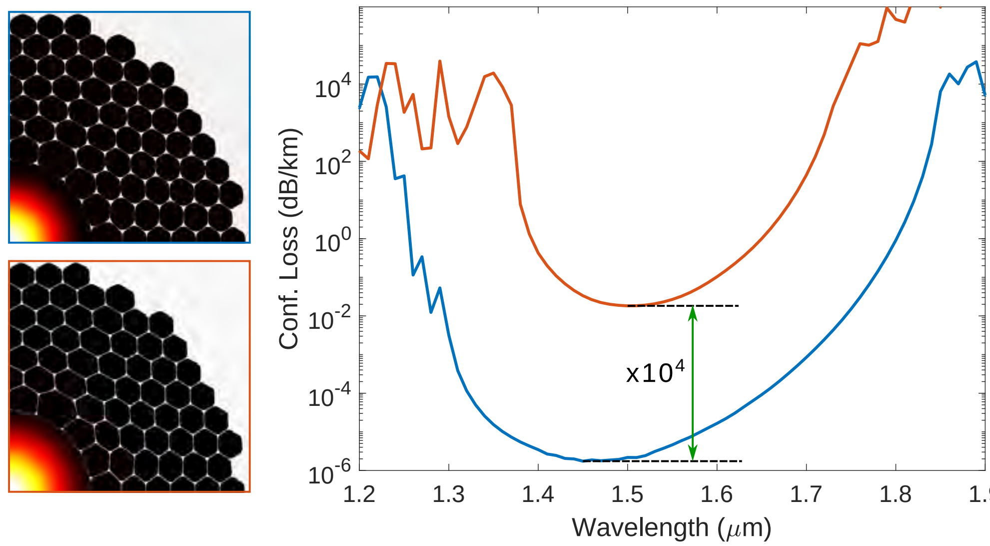

Fig. 8. Leakage loss in photonic bandgap fibers: impact of cladding strut thickness. The two fibers modelled here have the same core diameter of 29.6 μm. The cladding strut is 47 nm thick in the first fiber (blue, other parameters defined in Fig. 7), and 94 nm thick in the second fiber (orange). Note how the extremely low leakage loss (10^{-6} dB/km) in the first fiber fiber increases dramatically with strut thickness.

directly to lossy cladding or jacket modes. Depending on the symmetry of the modes involved, this can lead to crossings or avoided crossing events (anticrossings) with with core guided modes, resulting in a dramatic effect on the attenuation [98].

In PBGFs, the impact of such *surface* modes was recognized early on. The phenomenological Lorentzian of equations (12) and (13) above was derived when studying how these surface modes affect the attenuation of the fundamental mode in the fibers [69, 70, 133]. As it turns out, the core boundary in PBGFs is an extremely sensitive region which must be designed carefully in order to avoid high leakage loss, the related dramatic reduction in operational bandwidth as well as all other loss contributions [134, 135] . Simple prescriptions have been made to this effect, for example, using a core boundary that is half as thin as the cladding struts. This ensures that the modes they support fall outside of the photonic bandgap [57]. A more complete consideration however, also showed that the glass nodes at the core boundary must be of the same size as those in the cladding for optimum suppression of surface modes [68]. To illustrate the drastic effect surface modes can have on leakage loss in PBGF, we plot in Fig.10 The dispersion map for the PBGF of Fig.7, but where surface modes are introduced deliberately through a three times thicker core wall and also smaller nodes on the core boundary. These modifications result in surface modes that anticross with the fundamental mode near 1.42 μm and also in a markedly increased leakage loss at shorter wavelengths.

In antiresonant fibers, the core boundary is an equally critical region which must be designed carefully in order for the leakage to remain low. As discussed above, the introduction of a *negative curvature* core boundary in Kagomé fibers physically pushes the glass nodes away from the core, reducing the overlap between their modes and the core guided modes, and resulting in low loss and a smooth transmission spectrum free of spurious peaks [136].

In antiresonant tubular fibers or NANFs, the cladding is made of non-contacting sets of cylindrical glass tubes and there are no glass nodes. However, the thin, tubular glass membranes also support modes of their own. Away from the resonances, the modes supported by the

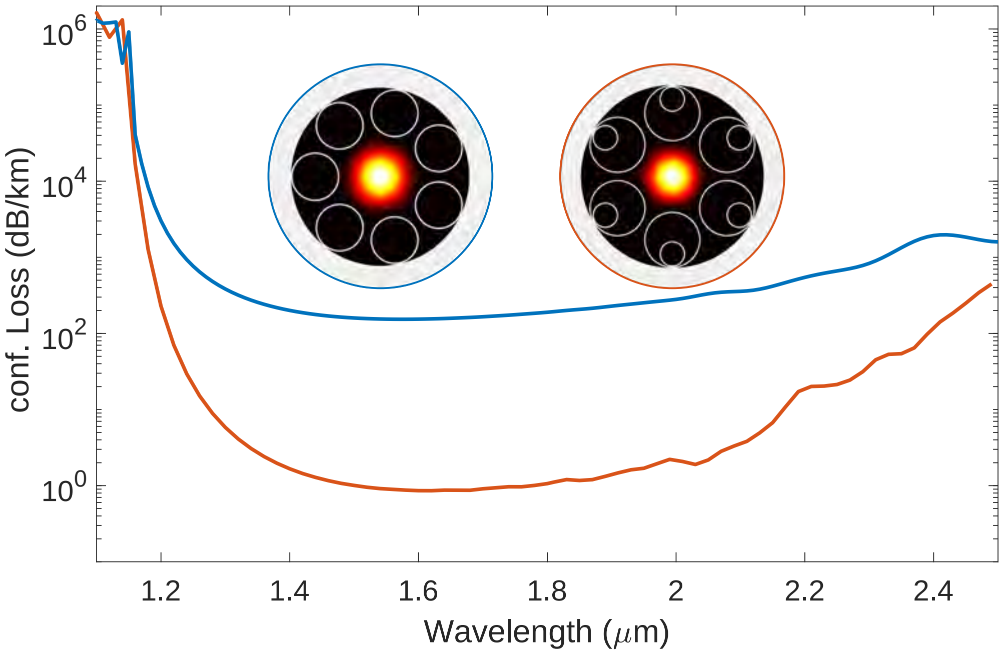

Fig. 9. Leakage loss in two example hollow-core antiresonant fibers. The first is a 7-tube tubular fiber and the second a 6-tube nested antiresonant fiber (NANF). Both fibers have a core diameter of 30μm and feature thin cladding tubes with 550 nm thickness. The gap between the tubes in both cases is kept at 3μm, one tenth of the core diameter.

glass membranes have a transverse phase profile $\sim e^{-im\theta}$ (θ is the angular position around the membrane) that changes rapidly (i.e. large m) and as a result have a vanishingly small overlap with core guided modes [82, 121, 137, 138]. The loss of the fibers in that region therefore is free of spurious peaks across the transmission bandwidth. However, as we approach the resonance wavelengths particularly from shorter to longer wavelengths the transverse phase of the membrane modes do not change as rapidly. Furthermore, as these membrane modes approach their cut-off, they expand and can have a strong overlap with the core modes, leading to the appearance of peaks in the leakage loss curves as a result. These peaks have the same phenomenological Lorentzian signature described above, see [139, 140]. The proximity of cladding tubes to one another creates, just as in the tight binding model, a band of allowed membrane modes, as described in [138]. It is the interaction between core and membrane modes that ultimately limits the useful bandwidth over which low loss can be achieved. We typically find that in antiresonant fibers with non-contacting tubular membranes, the spectral loss curve shows spurious peaks in the normalized frequency range $m \le f \le m + \frac{1}{2}$ where m is an integer ($f = 2t\sqrt{n^2 - 1}/\lambda$). Such small peaks are visible in the confinement loss plots in Fig .9 for the NANF of Fig.7 beyond the wavelength of 2 μm but are less prominent in that of the tubular fiber. To further illustrate this, we show the dispersion map for this NANF in Fig. 11 where we plot the normalized effective index $(n_{eff} - 1)\pi^2 f^2$ against the normalized frequency f for the first fifty modes of the fiber solved for with a finite element mode solver. We also show the computed leakage loss with a finer wavelength resolution where the spurious peaks of the loss curve due to avoided crossings is more apparent. One could therefore say that in nodeless antiresonant fibers, *surface modes* appear at the long wavelength edge of each transmission window, leaving the short wavelength edge and the middle part of the transmission unaffected, allowing wide operational bandwidths.

It is interesting to note that the small spurious peaks resulting from anticrossings are absent in

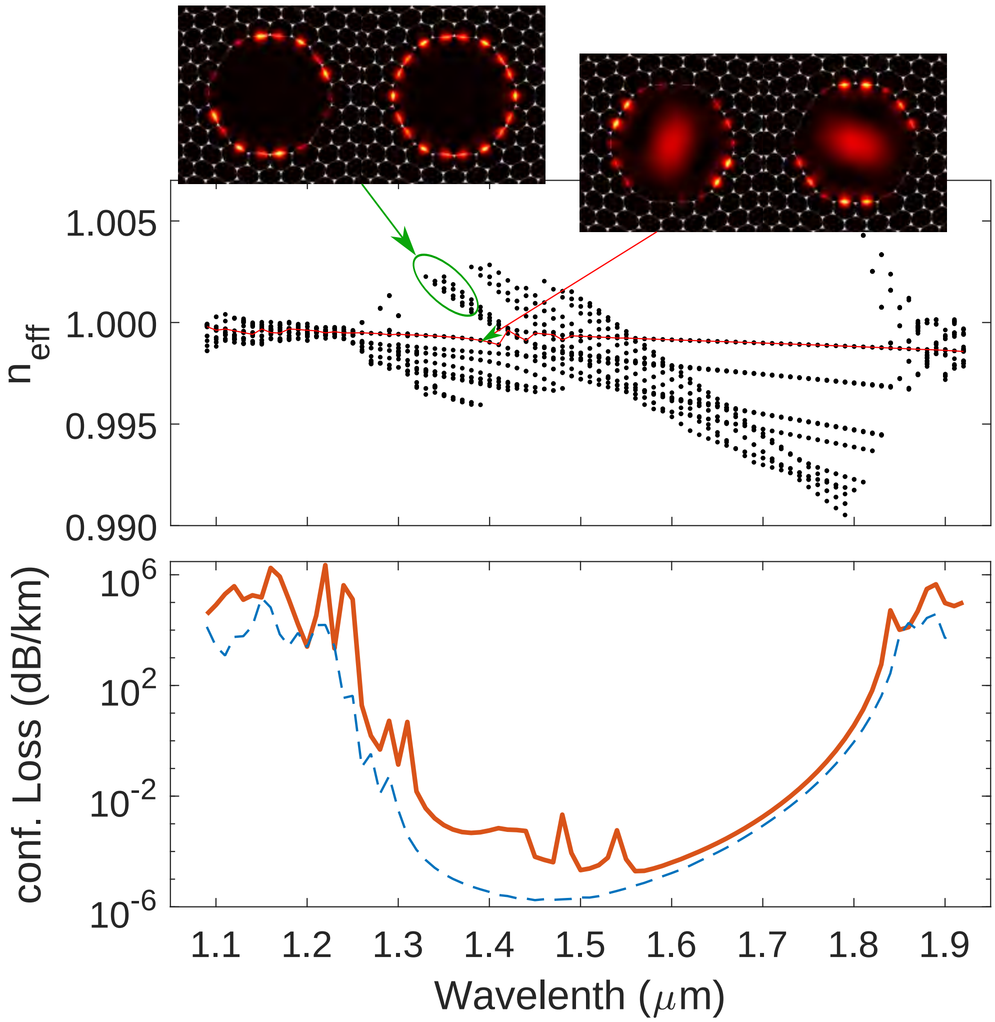

Fig. 10. The role of surface modes on the leakage loss of photonic bandgap fibers. With small modifications of the core boundary (thicker membranes and smaller glass nodes compared to the fiber in Fig8), surface modes are introduced and result in an anticrossing event with the fundamental mode near 1.42μm and a marked increase in leakage loss. The top figure shows the dispersion map as calculated by the finite element solver, 20 modes are solved for at each wavelength. The highlighted red curve is one of the degenerate fundamental mdoes for which the leake loss is plotted in the bottom figure. The surface modes (example shown in gree) can cross or anticross with the dispersion curve for the fundamental mode, leading to the peaks observed in the loss

the loss of a single annular tube waveguide (see Fig.6) or indeed the model structures analyzed by Bird [117]. Loss is instead sharply peaked at the resonant wavelengths. This is because in the tube, the number of membrane modes with a non-vanishing overlap with the fundamental core-guided mode mode is reduced to exactly one by virtue of symmetry.

2.5. Visualizing confinement

Confinement loss manifests as a non-vanishing radial Poynting flow away from the waveguide mode. As such, tools for visualizing this flow can be extremely useful in providing deeper

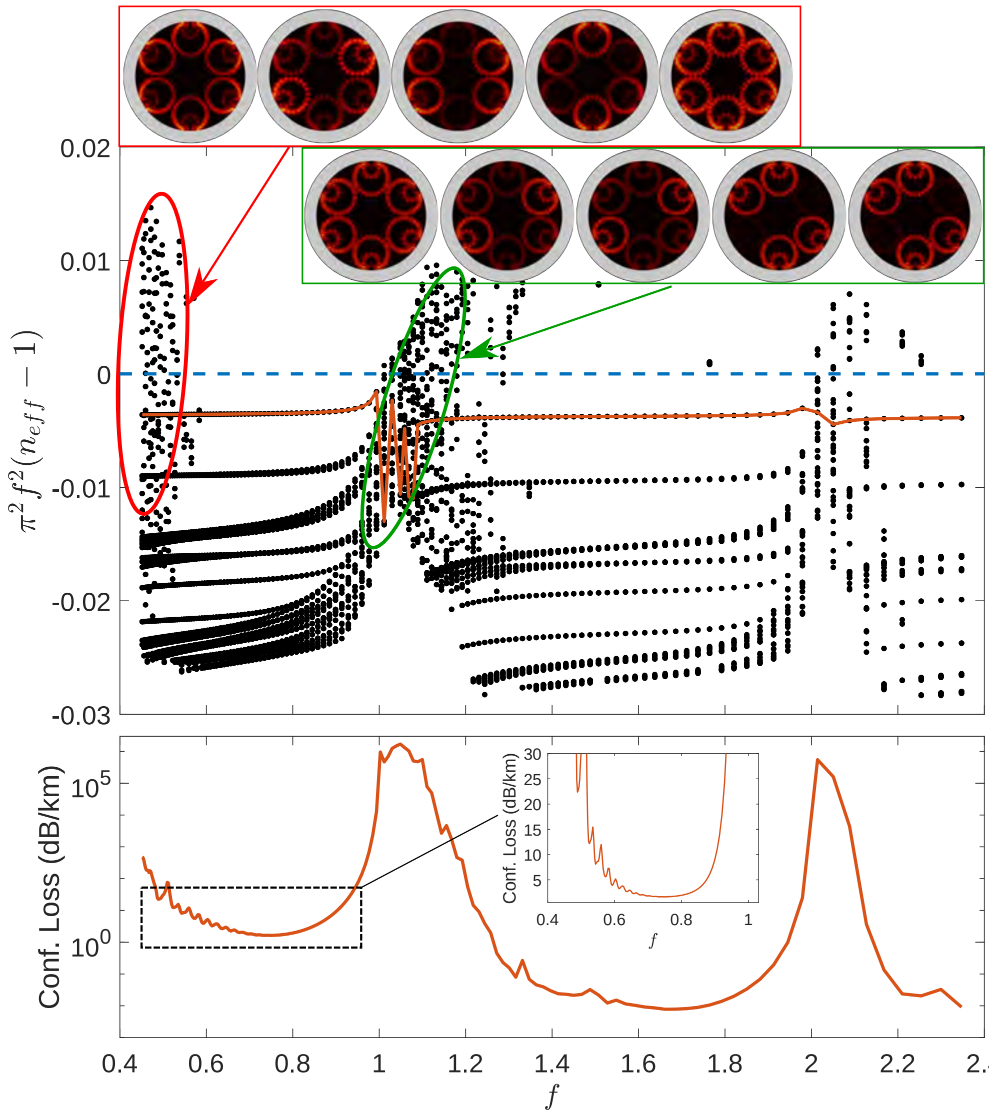

Fig. 11. Anticrossing and leakage loss in NANFs. The figure at the top shows the dispersion map plotted as normalised effective index against the normaized frequency. Near the resonant frequencies, the modes supported in the thin glass membranes crossing and anticrossing events with the core guided modes, in particular the fundamental mode whose curve is highlighted in orange and for which the leakage loss is plotted in the bottom figure. Note how the interaction between these glass modes and the core guided mode leads to peaks in the attenuation near the low frequency edge of the antiresonance window.

understanding of its origin and informing the engineering of geometric features of the fiber to further reduce it. Useful insight into the leakage loss, particularly that of antiresonant fibers where it is a significant contributor to total loss, can be obtained by examining the radial Poynting flux at the perimeter of the fiber. Resolving it azimuthally allows to link leakage loss to specific geometric features of the fiber. This can be used, for example, to identify the loss contribution due to the asymmetries present in the cross-section of a fabricated fiber [109]. As seen in Fig.12,

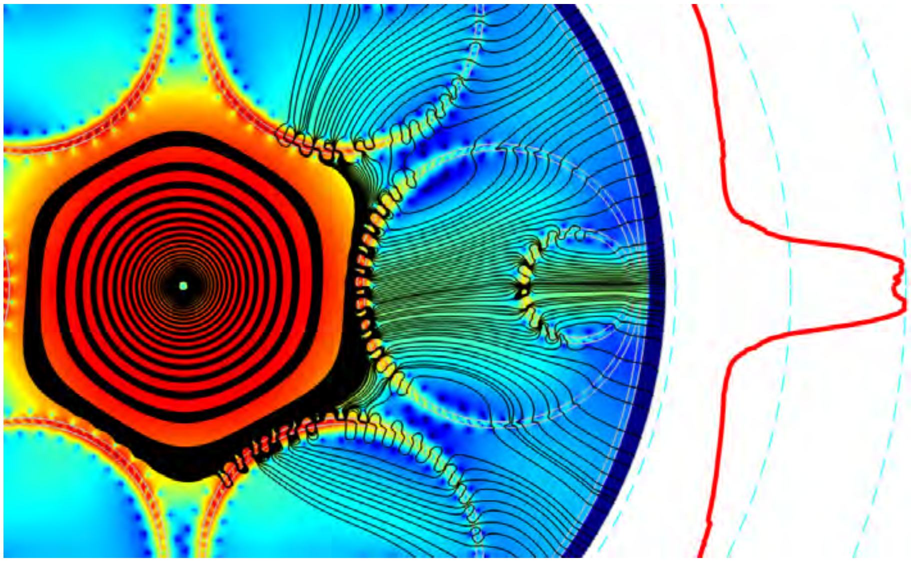

Fig. 12. Visualizing leakage loss in NANFs with the use of streamlines following the the transverse Poynting vector. The streamlines shown here are seeded near the center of the core and spiral outwards. Dense streamlines indicate stronger power flow. For example, near the outer boundary, the streamlines are denser near the nested element indicating that most of the power escapes through the tubes. The red curve shows the density of power leakage at the outer boundary of the geometry, i.e., the radial component of the Poynting vector as a function of angular position. As can be seen, it further confirms that leakage is highest at the azimuthal position of the tubes.

the azimuthally-resolved radial Poynting flux (red curve) for the NANF of Fig.7 at 1550 nm shows peaks at the position of the tubes, indicating that for this fiber, light escapes from the core predominantly through the tubes, confirming that leakage loss is occurs via coupling between core and tube modes. This conclusion changes for example if the gaps between the tubes become large, in which case leakage through the gaps becomes important.

Another powerful and useful visualization tool is that of examining transverse power flow streamlines of the guided modes. Streamlines are defined as lines which are always normal to the vector field, as such when they are closely spaced the local power flux is greater than when they disperse. This tool which has traditionally been used in fluid mechanics to map the path followed by an imaginary suspended in the flow , has proved useful in identifying routes taken by the optical power lost to radiation. In so doing, it also reveals geometry features which are an effective barrier to such transverse power flow and may thus lead to improved fiber designs with much reduced leakage loss [141–143]. Figure 12 shows the streamlines visualising the transverse power flow for the NANF structure of Fig. 7. The streamlines are seeded in a tight group in the core where the power flux is relatively uniform. Here, we see that the power travel outwards from the core, but as it approaches the cladding tubes,it predominantly flows through the capillaries themselves rather than the through gaps between them. Using this insight, a structure known as antiresonant leakage-inhibited fiber structure or ALIF was developed to add more radial gaps between capillaries. A nested pair was used instead of a single nested tube and confinement loss was reduced by a factor of 450 [142].

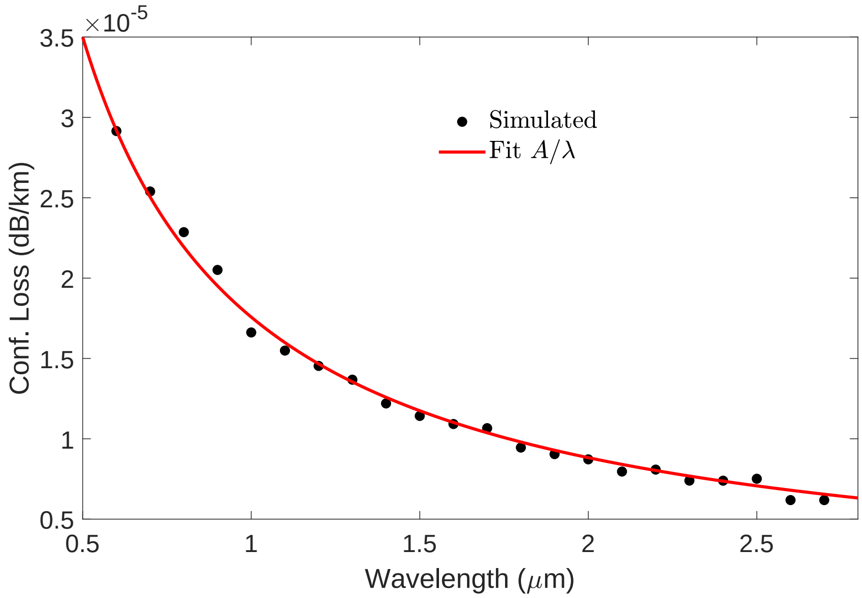

Fig. 13. Confinement loss in rigidly scaled photonic bandgap fibers. As a homothetic scaling is applied to the fiber structure for for operation at different wavelengths, the confinement loss is inversely proportional to the wavelength.

2.6. Scaling rules

Once a choice of cladding geometry has been made it is useful to establish approximate scaling rules for the confinement loss. Key parameters of interest here are the core size and the wavelength of operation. Such scaling rules are particularly important since other loss mechanisms may scale differently and the trade-offs between them can lead to an optimum region of operation over which the total attenuation of the fiber is the lowest.

In PBGFs, the leakage loss for a single fiber follows a U-shape across the photonic bandgap. As we have discussed, the leakage contribution to loss is in principle negligible or can be made so with more rings of air holes outside of the core. Nonetheless, knowledge of how the leakage loss scales with the core size, for example, can help determine the minimum number of cladding rings necessary to maintain it at negligible level and thus simplify fabrication. It was found that for a given cladding design (cladding pitch, strut thickness and air-filling fraction), the minimum leakage loss in the photonic bandgap obeys Marcatili's formula and scales approximately as λ^2/a^3 where a is the core radius [10]. Therefore, when the fiber is rigidly scaled to operate at different wavelengths, the confinement loss decreases as $1/\lambda$. We illustrate this in Fig. 13 where we plot the confinement loss for the bandgap fiber shown in Fig. 7, scaled rigidly to operate at wavelengths from 0.6 to 2.5μm. We have not included material absorption or dispersion, and as can be seen, the leakage loss scales as $1/\lambda$ as expected.

In antiresonant fibers, leakage is a greater contributor to the total loss of the fiber and how it scales with wavelength and core size is of paramount importance. Scaling rules are more complex, however, as they depend strongly on the choice of cladding parameters and design. In model antiresonant hollow core fibers made of l alternating alternating air/glass layers, equations (10) and (11) first derived by Bird state that to leading order, the leakage loss scales approximately as:

$$\alpha_{CL} \propto \frac{\lambda^{l+2}}{a^{l+3}} \tag{14}$$

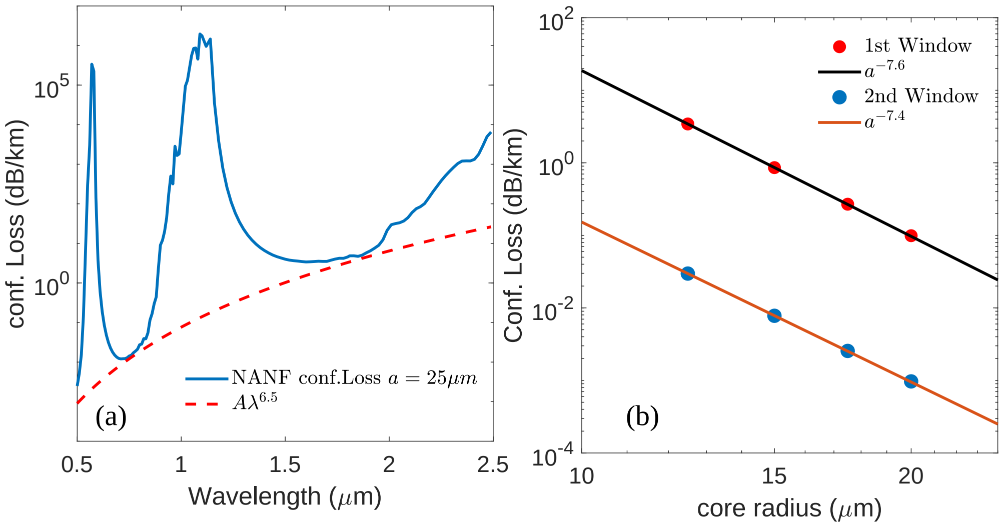

Fig. 14. Confinement loss scaling with wavelength and core size in NANFs. In (a), the NANF has the same structural parameters as the one in Fig.9. In (b) We applied a rigid scaling to this structure, maintaining the membrane thickness of 550 nm and a relative inter-tube spacing of $a/5$. The minimum confinement loss scales approximately as $\lambda^{6.5}/a^{7.5}$

Although practical fibers such as tubular fibers and NANFs differ from these highly simplified model structures, the insight they offer is valuable. In [101], it is shown for an example NANF structure that the minimum leakage loss across antiresonant windows scales approximately as λ^7/a^8, which would be compatible with Bird's formulae for $l = 5$. However, the exact scaling with core size and wavelength depends on cladding parameters such as the number of tubes, their sizes, and the inter-tube gaps. Furthermore, equations (10) and (11) show the explicit dependence of the loss on the refractive index n as well as the transverse phase accumulated across each layer in the structure ϕ_i which both depend on the wavelength. For the NANF example shown in Fig.7 with $t = 550$ nm and a gap of $a/5$, we find as shown in Fig.14 that the loss scales as $\lambda^{6.5}/a^{7.5}$, again conforming approximately to the simplified model derived by Bird for $l = 5$. The addition of nested elements in various configurations therefore not only help reduce the leakage loss, but also how rapidly it scales with wavelength and core size [101, 132, 142]. For the double nested fiber we recently reported in [45] for example, we expect the loss to scale approximately as λ^9/a^{10}.

3. Absorption

Absorption is one of the most fundamental loss mechanisms in optical waveguide. The waveguide's constituent materials absorb light at wavelengths corresponding to transitions between the electronic or ro-vibrational energy levels of its molecules. In fused silica, absorption originates either from electronic transitions in the ultraviolet which have an edge in the visible and near-IR (Urbach edge [144, 145]), or from vibrations of the silica oxygen bonds at wavelengths longer than about 1700 nm [146]. In addition, the preparation processes of the raw glass material may introduce impurities and related absorption bands. Hydrogen or moisture for example react with defect sites in silica to form absorbing species such as chemically bonded hydroxyl groups (OH) with a fundamental absorption band at 2720 nm and a first overtone near 1380 nm [147, 148]. In hollow-core fibers as we will show below, absorption in the glass material is suppressed by more than four orders of magnitude due to the strong confinement of the mode field in the hollow regions. On the other hand, the environment in these hollow regions may be filled with a gas or a mixture of gases with absorption lines at wavelengths of interest. This section discusses the contribution of absorption to the total loss of the fiber.

3.1. Absorption in the glass material

One of the heralded advantages of hollow-core fibers is that they can provide low-loss optical guidance in fibers made of highly lossy materials [87]. This property naturally comes from the fact that guidance in the hollow region strongly suppresses the overlap between the guided optical mode field and the solid material. This has led for example to hollow-core fibers having losses as low as ~40 dB/km in the infrared near the 4 μm wavelength where the absorption of the glass material is as high as 860 dB/m, showing more than a than a twenty-thousand fold suppression of absorption [107].

Mathematically, when the material is absorbing, we can calculate the resulting loss penalty incurred by the optical mode $|\psi_k\rangle$ through a perturbation treatment. Let us consider that the absorption in the material is quantified through an absorption coefficient α_{bulk} in m^{-1}. This correspond to the addition a small imaginary component to the refractive index given by $-j\alpha_{bulk}/2k_0$ and by extension to a small imaginary part to dielectric constant $-j\delta\varepsilon = -jn\alpha_{bulk}/k_0$. From first order perturbation theory, one can show that the purely imaginary correction to the propagation constant of mode $|\psi_k\rangle$ is [54, 149, 150]:

$$\begin{aligned}\Delta\beta_k &= -j\frac{\omega}{c}\langle\psi_k\,|\,\delta\varepsilon\,|\,\psi_k\rangle \\ &= -j\iint_{A_\infty}|\mathbf{E}_k|^2\,n\alpha_{bulk}dxdy\end{aligned} \tag{15}$$

where the modes are normalized to obey the orthonormality condition [54, 151–153]:

$$\iint_{A_\infty}\vec{z}\cdot\left(\mathbf{E}_k\times\mathbf{H}_l^*+\mathbf{E}_l^*\times\mathbf{H}_k\right)dA=\delta_{kl} \tag{16}$$

Here, $\mathbf{E}_k$ and $\mathbf{H}_k$ are the electric and magnetic field vectors of the mode $|\psi_k\rangle$. For the absorption in the glass material alone, the integral of Eq.15 extends only in the glass region in the fiber's cross-section. If the absorptive perturbation is further considered constant in the glass, the absorption loss is simply:

$$\alpha_{abs}=-2\Im(\Delta\beta_k)=2\alpha_{bulk}\iint_{glass}|\mathbf{E}_k|^2\,ndxdy=\zeta\alpha_{bulk} \tag{17}$$

Clearly, the glass absorption is suppressed by a factor ζ given by:

$$\zeta=\frac{\alpha_{abs}}{\alpha_{bulk}}=2\iint_{glass}|\mathbf{E}_k|^2\,ndxdy \tag{18}$$

In other words, the absorption in the glass is suppressed by a factor proportional to the fraction of the normalized $|\mathbf{E}_k|^2$ in the glass material, as also derived elsewhere [154]. In hollow-core fibers, the absorption in the glass is suppressed by a few orders of magnitude as compared to bulk. For the optimized 19c PBGF shown in Fig.7, we calculated ζ across the photonic bandgap and plot the results in Fig. 15, obtaining a minimum value of the order of 400 parts per million (corresponding to an absorption suppression factor $1/\zeta$ of 2.5×10^3). In the NANF of Fig.9 which has a similar core size, we find a minimum ζ value of 90 parts per million (suppression factor of ~10^4) in the first antiresonant window, about 4.5 times smaller than the PBGF.

The value by which glass absorption is suppressed, i.e., $1/\zeta$, evidently depends on the core size, the wavelength, and the design of the cladding, as one may expect. For example, in NANFs with

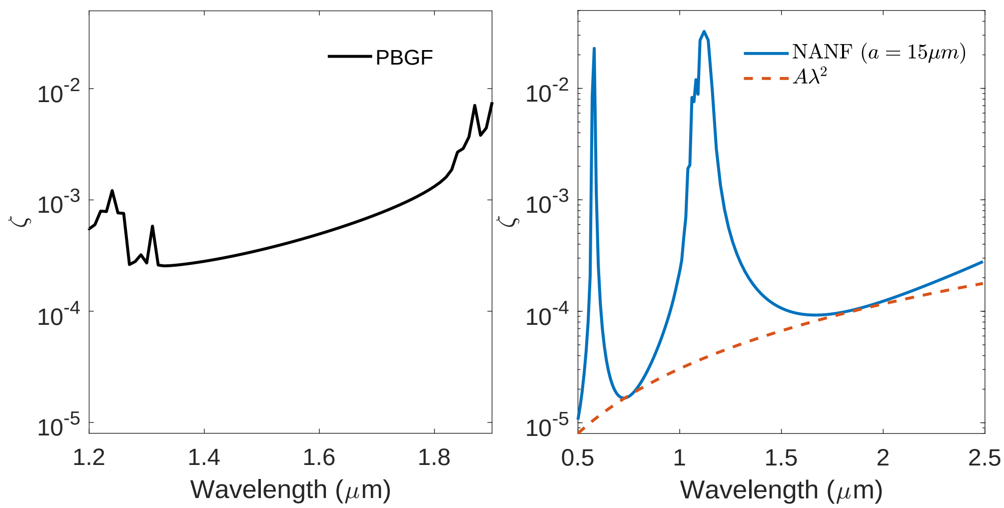

Fig. 15. Glass absorption and bulk scattering loss suppression factor in the PBGF (left) and NANF (right) of Fig.7. With our choice of design parameters, ζ in the PBGF increases with wavelength across the bandgap, going from 250ppm at 1.4µm to 2000 ppm at 1.8µm. ζ is lower in the NANF with minima of 90ppm and 18ppm in the first and second windows respectively. The minima across antiresonant windows increasing roughly as λ^2.

larger core diameters and thinner membranes such as the one reported in [109], the typical value for ζ is 40 to 50 ppm in the first window and 10 to 20 ppm in the second. We can derive a first order scaling rule of ζ with core diameter, wavelength and membrane thickness by considering the simple tube waveguide such as the one shown in the inset of Fig.6. At wavelengths away from the edges of the transmission windows, the field near the core boundary scales approximately as λ/a [54, 115, 155]. When normalized according to Eq.(16), the field at the interface is further divided by a quantity proportional to $\sqrt{mode\ area} \propto a$ so that the normalized field at the interface scales as λ/a^2. Since the integral of Eq.18 is performed over an area roughly equal to the product of the core boundary circumference and the membrane thickness. It follows therefore that to first order, the factor ζ scales as:

$$\zeta = \frac{\alpha_{abs}}{\alpha_{bulk}} \propto \left(\frac{\lambda}{a^2}\right)^2 \cdot a \cdot t \propto \frac{\lambda^2 t}{a^3} \tag{19}$$

We have found that this scaling rule derived for a thin tube of radius a and thickness t holds approximately antiresonant fibers like tubular fibers and NANFs. In Fig.15, we show the approximate λ^2 scaling for the NANF of Fig.7. This scaling relation derived from first principles here is similar to the empirical one found by Vincetti through fitting numerical simulations of tubular fibers [139]. To first order, the scaling is independent of the exact geometry of the fiber, which does not come as surprise given that most of the field confined in the glass is located in the membranes closest to the core.

Eq.(19) can be used to estimate the contribution to loss from glass absorption for fibers operating at different wavelengths without the need for computationally expensive finite element simulations. For example, using the ζ values calculated for the PBGF in Fig.15, we can see that if this fiber is rigidly scaled shift the bandgap to different wavelengths , i.e, both λ, t (which in this case can be taken as the cladding strut thickness) and a are scaled in proportion, then ζ does not change not change appreciably with wavelength, particularly if dispersion is neglected [101].

Eq.19 also points to an important insight as to why in spectral regions where the material is

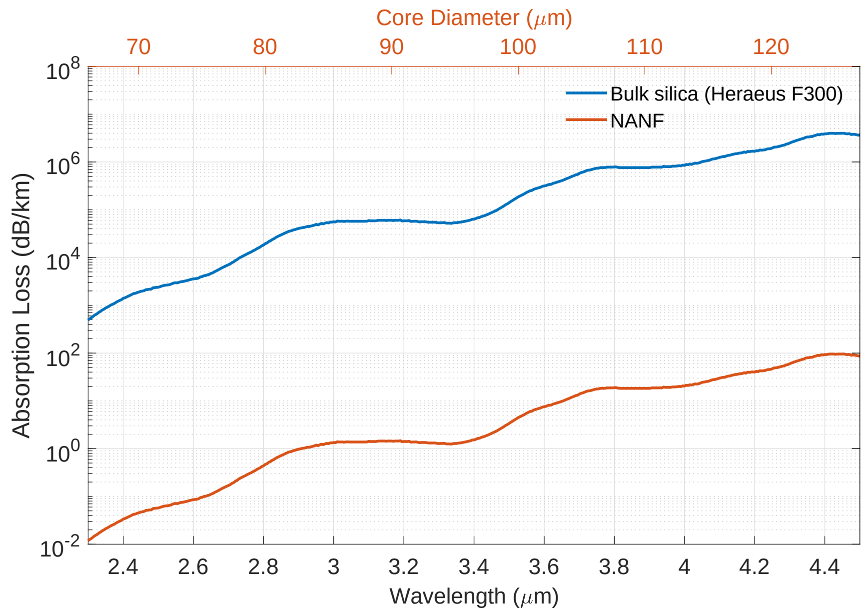

Fig. 16. Calculated glass absorption loss in rigidly scaled NANFs. For the example shown here, we have chosen a/λ = 19.35 and a/t = 86. At 4μm, with a core diameter of 113μm, absorption loss can in principle be reduced to only 20 dB/km. Reported values stand at 40 dB/km in a tubular design [107]

highly absorptive, antiresonant fibers have the potential of outperforming their PBGF counterparts. This key advantage is the freedom, at any chosen operating wavelength, to flexibly change the core size whilst keeping the cladding membrane thicknesses constant. For example, doubling the core size results in absorption being reduced by a factor of 8 if the thickness and cladding design are kept the same. In contrast, while enlarging the core of photonic bandgap fibers by removing a greater number of unit cells to make the core defect is in principle feasible, it has proved extremely challenging to do in practice and the most successful embodiment at all reported wavelengths are fibers with 19 cell core defects. It is no surprise that the lowest loss fibers at wavelengths beyond about 2μm or below 1μm are of the antiresonant type [103](see Fig.5.

Despite the orders of magnitude suppression of glass absorption, this loss contribution can become the dominant contribution to HCF loss in the mid-infrared where silica's absorption is higher than 10 dB/m. In Fig.16, we plot the predicted minimum absorption loss for rigidly scaled NANFs operating at wavelengths between 2.4 and 4.4 μm. For these calculations, we chose a core size to thickness ratio a/t ~86, giving a minimum value $\zeta = 2.4 \times 10^{-5}$ in the first antiresonant window. The loss of bulk silica at these wavelengths is extracted from the data provided by Heraeus [156]. We see that despite the high loss of the silica material (>1000dB/m), for our design restriction, <100 dB/km is possible up to 4.5μm [107, 154]. We project that for example, at 7μm where glass attenuation is 60dB/mm (not shown here), a fiber with a core diameter of 200μm and a membrane thickness of 2.3μm would have an absorption loss of 1.4 dB/m, making low-loss guidance possible for a wide range of apprications across the mid-IR.

3.2. Absorption in the gases within the hollow regions

In applications such as gas-based photonics where relatively short lengths of fiber are required, the exact composition of the gas inside the core is often carefully controlled [35]. In contrast, in telecommunication applications for example where light is transmitted over tens of kilometers of fiber, little attention has traditionally been paid to the control of the gaseous mixture inside the hollow-regions of the fiber. Yet, if present, gas species in the hollow-regions can impact the performance of the fiber and also contribute to attenuation.

Although few studies have been devoted to the composition of gases inside hollow-core fibers when not intentionally controlled, a number of publications have reported observation of atmospheric gas species such as water vapor and carbon dioxide [157, 158] and other gas species such as hydrogen chloride [83, 106, 107, 158, 159]. The presence of atmospheric gas species originates from ingress of atmospheric gases into the fiber post-fabrication if its ends are left open. This, it is now understood, is facilitated by the lower pressure inside the fiber immediately after fabrication [160, 161]. The presence of gas species such as hydrogen chloride is thought to arise from remnants of halogenated precursors employed in the production of the fused silica used to make hollow-core fiber preforms [83, 107].

Molecular gases present within the hollow regions of the fiber affect the fiber attenuation through direct absorption, whether from direct electronic transitions or from ro-vibrational transitions [158]. In the literature, gas absorption has featured more prominently in fibers designed to operate in the mid-infrared, the so-called fingerprint region. For hollow-core fibers operating at wavelengths between 1 and 1.8 µm, the absorption band around 1.4 µm often features prominently (see for example [45, 109]). This feature originates from the hydroxyl ions in the silica, but may also come from atmospheric water vapor [162].

The contribution of gas absorption to loss in hollow-core fibers is not fundamental and when present, can be eliminated by improvements in the fabrication process for example through the use of different precursors in the preparation of the raw glass material, or as has been shown, by additional post-fabrication processing steps like purging with inert gases [83, 106].

4. Bulk scattering

In addition to absorption, light propagation in optical waveguides experiences Rayleigh scattering which arises because of the intrinsic microscopic inhomogeneity present in most optical materials. In hollow-core fibers, Rayleigh scattering contributions to loss come from the glass material as well as from potential gases with which the hollow regions of the fiber may be filled.

One approach to calculating the contribution from Rayleigh scattering is to consider that the inhomogeneities resulting from thermodynamic density fluctuations are effectively equivalent to a small, real perturbation to the dielectric permittivity $\Delta\varepsilon(x, y, z)$. A perturbation treatment can then be used to estimate the total power scattered as a result of such perturbation, see for example [155]. A more intuitive estimate of the contribution from Rayleigh scattering can be made by realising that the Rayleigh loss coefficients for most constituent materials of the hollow-core fiber are well-known. One can thus regard this well-known loss as equivalent to a small absorption, i.e a small imaginary perturbation to the dielectric constant. The same conclusions from the previous section therefore follow logically.

4.1. Scattering within glass

It follows from the preceding section that, like absorption, the contribution to loss from bulk scattering in the glass is expected to scale approximately as the material loss suppression factor ζ. Taking the Rayleigh scattering contribution of pure silica as $\alpha_R = 0.11 \times (1.55/\lambda[\mu m])^4$ [146], it follows that the the loss contribution from bulk scattering in glass is proportional to:

$$\alpha_{sc} = \zeta\alpha_R \propto \frac{\lambda^2 t}{a^3} \cdot \lambda^{-4} \propto \frac{\lambda^{-2} t}{a^3} \tag{20}$$

For rigidly scaled fibers, scattering therefore scales with wavelength as λ^{-4}. However, the small values of ζ make the contribution from bulk scattering negligible. For the example NANF structure of Fig.7, the Rayleigh scattering in the glass contributes ~10^{-5}dB/km at 1550 nm to the loss. If this fiber is scaled rigidly to operate at 100 nm, Eq. (20) indicates that the contribution increases to 0.6dB/km only and is therefore safe to be neglected.

4.2. Scattering within the hollow regions

When the hollow regions of the fiber are filled with a gas, a small Rayleigh scattering contribution to loss may be expected. Because nearly all of the optical field is confined in the hollow regions, this scattering loss contribution is given by the Rayleigh scattering coefficient of the filling gas. Assuming that the hollow regions of the fiber are filled with air at room temperature and atmospheric pressure, the effective Rayleigh scattering coefficient in the hollow regions is 4.7×10^{-3} dB·μm^4/km (see [163]), meaning that at 1550 nm, Rayleigh scattering loss is approximately 8×10^{-4} dB/km. Although this increases linearly with the gas pressure, it still amounts to a negligible contribution to loss and can safely be neglected.

5. Surface contributions to loss

In any optical waveguide, perturbations on boundaries between constituent materials can lead to additional contributions to loss, particularly when the amplitude of the guided optical mode field near such boundaries is high or the refractive index contrast between the constituent materials large [113, 164–166]. This is the case for HCFs as their structure incorporates multiple air-glass interfaces which possess intrinsic roughness of thermodynamic origin [73]. Surface contributions to loss originate from scattering when the material boundaries are perturbed along the length of the fiber, for example by the intrinsic roughness, or from absorption and scattering when potential impurities are adsorbed on the surfaces.

One fundamental mechanism giving rise to intrinsic roughness on air-glass interface in HCFs is that of frozen-in surface capillary waves [73]. As is the case on the surface of any heated liquid, thermally excited capillary waves exist on the surface of molten glass under the restoring force of surface tension. As molten glass goes through solidification, these surface capillary waves freeze in, giving rise to an intrinsic surface roughness. In [49], Roberts *et al.* argue that it is scattering from this intrinsic surface roughness that imposes a fundamental limit on loss in HC-PBGFs. In this section, we examine the loss contribution from light scattering at the air-glass interfaces within HCFs.

5.1. Rigorous theoretical treatment

Traditionally, the tools of choice for calculating loss originating from perturbations to material boundaries such as surface roughness within waveguides have been coupled-mode theory methods [113, 165, 167–173]. However, such tools require knowledge of the infinite set of radiation modes of the fibers in order to accurately estimate loss, making these methods challenging for use in microstructured fibers. An alternative method of estimating scattering loss is to consider that the fields scattered by each perturbation *bump* interfere coherently in the far-field [174]. This approach is generalized here using the so-called the volume-current methods [175–178].

Let us consider that the mode $|\psi_k\rangle$ is propagating through a fiber section of length L, long enough to contain all the relevant features of the perturbations, but also short enough to assume the mode doesn't suffer significant loss. This is illustrated schematically in Fig. 17. We first compute the current density induced by the presence of the surface inhomogeneities within this section of the waveguide, and from it the far field distribution of the radiated field and thus loss. Describing the geometric perturbations caused by roughness on the air-glass interfaces with a small, zero-mean, deviation $h(s, z)$ (s is a curvilinear coordinate along the relevant interface in the cross-section) assumed not to change the local surface normal nor the refractive index, the

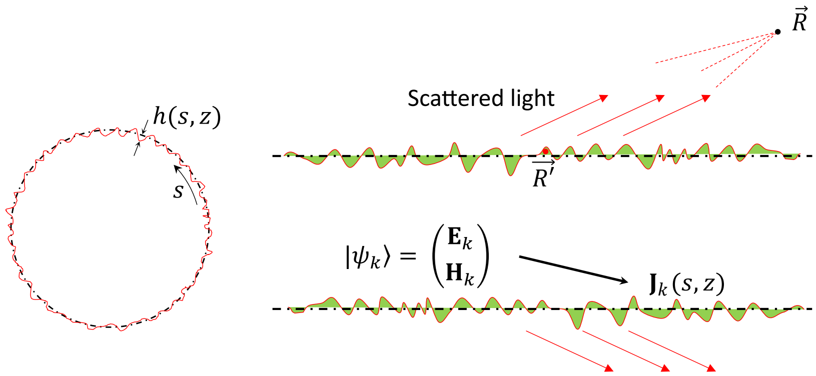

Fig. 17. Schematic illustration of the process of roughness scattering in a hollow-core fiber.

induced current density at a point (s, z) can be expressed as [155, 166, 179]:

$$\mathbf{J}_k(s,z) = -j\omega\varepsilon_0 \left(\Delta\varepsilon_r \mathbf{E}_{\parallel k}(s,z) - \Delta\frac{1}{\varepsilon_r}\mathbf{D}_{\perp k}(s,z)\right) h(s,z) \tag{21}$$

Here, $\Delta\varepsilon_r = n^2_{glass} - 1$ and $\Delta 1/\varepsilon_r = 1/n^2_{glass} - 1$, $\mathbf{E}_{\parallel k}$ and $\mathbf{D}_{\perp k}$ are the component of the electric field parallel to the interface and the component of the electric displacement normal to the interfaces, respectively. By using only field expressions continuous across the interface, this expression ensures the current density is not ill-defined and doesn't depend on the side of the interface on which it is computed. Making the approximation that this induced current radiates in free space, the electric and magnetic field vectors at a location defined by position vector $\vec{R}$ on a far-field sphere centered on the section of the fiber under analysis are given by [175, 180]:

$$\mathbf{E}_s(\vec{R}) = -jk\frac{e^{jkR}}{4\pi R}\left(\vec{r} \times \int_V e^{-jk\vec{r}\cdot\vec{R}'}\mathbf{J}_k(s,z)dV\right) \tag{22}$$

$$\mathbf{H}_s(\vec{R}) = -j\omega\mu\frac{e^{jkR}}{4\pi R}\vec{r} \times \left(\vec{r} \times \int_V e^{-jk\vec{r}\cdot\vec{R}'}\mathbf{J}_k(s,z)dV\right) \tag{23}$$

where $\vec{r} = \vec{R}/R$ and $\vec{R}'$ is the location of the perturbation within the fiber. The integration extends over the total volume containing the perturbed waveguide section. We can shorten the integrand in the above expressions by writing:

$$\begin{aligned}\vec{r} \times \mathbf{J}_k(s,z) &= -j\omega\varepsilon_0 \left(\Delta\varepsilon_r \vec{r} \times \mathbf{E}_{\parallel k}(s,z) - \Delta\frac{1}{\varepsilon_r}\vec{r} \times \mathbf{D}_{\perp k}(s,z)\right) h(s,z) \\ &= -j\omega\varepsilon_0 \vec{U}_k(s)e^{-j\beta_k z}h(s,z)\end{aligned} \tag{24}$$

where we have used $\mathbf{E}_k(s,z) = \mathbf{E}_k(s)e^{-j\beta_k z}$, β_k being the propagation constant of the mode $|\psi_k\rangle$. The Poynting vector of the scattered field at the observation point is then given by:

$$\begin{aligned}\mathbf{S}_k(\vec{R}) &= \frac{1}{2}\left\langle \mathbf{E}_s(\vec{R}) \times \mathbf{H}^*_s(\vec{R})\right\rangle \\ &= \frac{\omega^4\varepsilon_0^2\mu}{32\pi^2R^2c}\vec{r}\int_V\int_V \langle h(s',z')h(s,z)\rangle\,\vec{U}_k(s)\vec{U}^*_k(s')e^{-j\beta_k(z-z')}e^{jk\vec{r}\cdot(\vec{R}'-\vec{R}'')}\end{aligned} \tag{25}$$

where $\langle\ldots\rangle$ represents an ensemble average. Eq. (25) can be further simplified when the roughness autocorrelation $\langle h(s',z')h(s,z)\rangle$ can be expressed as a product of functions of $s-s'$ and $z-z'$. The roughness resulting from frozen-in thermally excited capillary waves is non separable with respect to the longitudinal direction and that along the perimeter, making the evaluation of the integral in Eq. (25) complicated [48, 73]. We argue however that in hollow-core fibers, the most important features of the roughness, especially those dictating the angular distribution (with respect to the polar angle with the fiber axis) of the scattered light are those along the fiber axis (see also [49]). Using a spherical coordinate for the far-field point $\vec{R}\,(R,\theta,\phi)$ and a cylindrical coordinate for the location $\vec{R'}\,(\rho',\phi',z)$ of the perturbation, we have $\vec{r}\cdot\vec{R'} = z\cos\theta + \rho'\sin\theta\cos(\phi-\phi')$. With this, the far-field Poynting vector becomes:

$$\mathbf{S}_k(\vec{R}) = \frac{\omega^4\varepsilon_0^2\mu}{32\pi^2R^2c}L\tilde{\Psi}\left(\beta_k - k\cos\theta\right)\vec{r}\sum_m\left|\oint_{C_m}\vec{U}_k(s)\mathrm{e}^{jk(\rho'\sin\theta\cos\phi-\phi')}ds\right|^2 \quad (26)$$

Here, we have assumed that the roughness on the each glass interfaces labelled m is statistically independent. In other words, the physical process giving rise to roughness is the same, but the roughness on each interface is independent of the others. The roughness on each interface does however have the same power spectral density in the z direction defined as:

$$\tilde{\Psi}\left(\Delta\beta\right) = \int_0^L \langle h(z')h(z)\rangle\, \mathrm{e}^{-j\Delta\beta(z-z')}d(z-z') \quad (27)$$

Eq.(26) is essentially the same result we derived previously in [174], but is more general and without the approximations on the dipole polarizability. Eq.(26) can be evaluated from the mode-field data obtained by commercial finite element solvers like COMSOL Multiphysics, with an overhead on computation time that depends on the resolution in θ and ϕ on the far-field scattering sphere. Fig.18 shows plots of the calculated far-field scattering pattern for the fundamental modes of the PBGF and NANF of Fig.7. To display features of the scattering pattern, we assumed here a PSD $\tilde{\Psi}\left(\Delta\beta\right) = 1$. As may be expected, the more complex structure of the PBGF leads to a richer scattering pattern in the far field, where contributions from the glass nodes on the core boundary for example are visible as the hotspots in the scattered field distribution. In NANFs on the contrary, one only sees that the far-field scattering pattern reflects the six-fold symmetry of its structure.

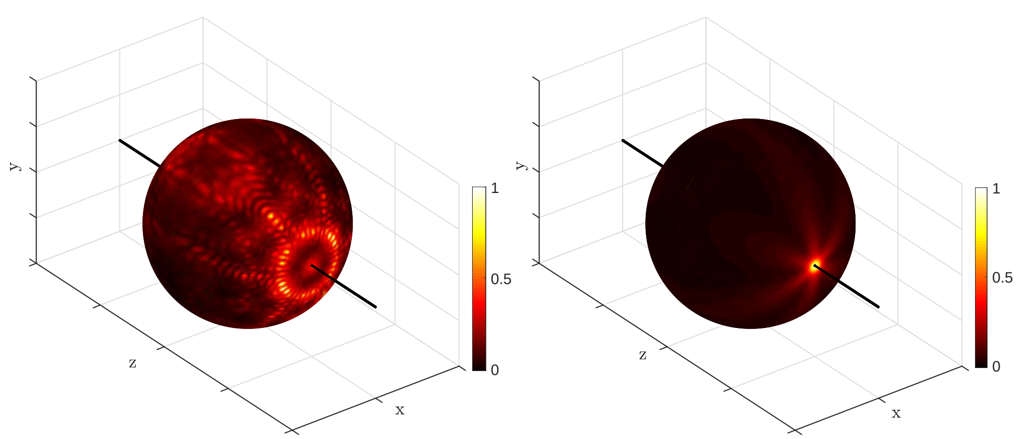

Fig. 18. Normalized far-field distribution of the roughness-scattered power in the PBGF (left) and NANF (right) of Fig.7 as computed from Eq. (26). The more complex structure of the PBGF reveals a richer scattering pattern whereas the six-fold symmetry of the NANF is clearly reflected in its scattering pattern.

When the power spectral density of the roughness is known, the surface scattering loss rate from the fiber is obtained as

$$\alpha_{ssc} = \frac{1}{L} \frac{\int \vec{r} \cdot \mathbf{S}_k R^2 d\Omega}{P_k} \tag{28}$$

where the integration is carried over the 4π solid angle and P_k is the power carried by the incident mode, expressed as the integral of a Poynting flux as in the previous section.

5.2. Intrinsic roughness on air-silica interfaces

It is now well-known that the air-glass interfaces in microstructured optical fibers possess a fundamental and intrinsic surface roughness originating from thermally excited surface capillary waves which are frozen-in during the fiber draw [49, 73]. Such roughness has been thoroughly investigated on flat surfaces of horizontally formed thin glass films [73, 181]. In such a scenario, gravity provides a dampening force to the excited thermal capillary waves on the liquid glass surface, leading to a two-dimensional power spectral density of the form:

$$\tilde{\Psi}_{2D}(\kappa) = \frac{k_B T_g}{\rho g + \gamma |\kappa|^2} \tag{29}$$

where κ is the two dimensional surface wavevector, ρ the glass density and g the gravity constant. k_B is Boltzmann's constant, T_g the glass transition temperature and γ the surface tension of the glass.

In the case of hollow-core fibers, the surfaces are typically closed in one direction (in the cross-section) rather than flat and are made under an imposed vertical flow. Therefore, gravity does not play the same role as a dampening force. It remains unclear if the applied pressure differentials provide a similar restoring force. Since the surfaces in fibers are closed in one direction, the surface capillary wave roughness is quantized along the coordinate on the hole perimeter in the cross-section and can be expressed as an infinite Fourier series which is then summed to yield the roughness PSD in the longitudinal direction [48, 49]. For loss estimates in this paper, we will take this longitudinal PSD as [71, 174]:

$$\tilde{\Psi}_{1D}(\kappa) = \frac{k_B T_g}{4\pi\gamma\sqrt{\kappa_c^2 + \kappa^2}} \tag{30}$$

where we have introduced a low spatial frequency cut-off κ_c to avoid divergence at long spatial wavelengths where $\kappa \to 0$. Whilst such a cut-off for horizontal surfaces arises because of the above-mentioned restoring effect of gravity, its origin on the surfaces in HCFs is not yet known. It is worth mentioning however that atomic force microscope (AFM) measurements performed in on dimension along the fibre axis in PBGFs revealed that the roughness was compatible with Eq.(30), but with surface tension $\gamma = 1J \cdot m^{-2}$, more than three times higher than the value traditionally quoted for silica $\gamma = 0.3J \cdot m^{-2}$ [49, 182–185]. Recently, 2D AFM measurements have shown that the externally applied draw stress during the manufacturing process results in attenuated roughness along the axial direction where such stress is applied [186]. This is compatible with earlier measurements showing a higher surface tension than in float glass thin films. For this reason, we will use the following widely accepted parameter values to estimate the loss: T_g =1500 K, γ = 1 J.m^{-2}. For the spatial frequency cut-off, it is reasonable to assume that it corresponds to a length scale of the order of the perimeter of the air-glass interface in the cross-section. For the remainder of the paper, we use the value $\kappa_c = 2\pi/100\mu m$ (i.e. slightly longer than the perimeter of the typical air-glass interface).

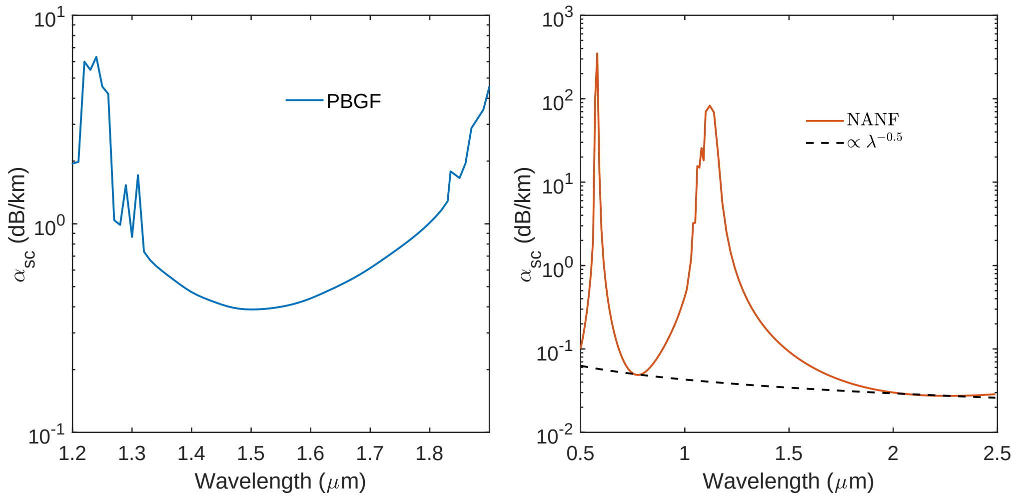

Fig. 19. Rigorous scattering loss calculations for the PBGF (left) and NANF (right) of Fig.7. It is assumed that the roughness present on the air-glass interfaces is the same and limited to the fundamental frozen-in surface capillary waves roughness. This results in the minimum loss in the PBGF (0.4 dB/km) being roughly 15x higher than in the NANF (0.027 dB/km). Note that for this particular NANF, the minimum loss across windows scales weakly with wavelength, decreasing approximately as $\lambda^{-0.5}$. This scaling is subject to both the exact structure of the fiber (number of tubes, gap between them) and the choice for spatial frequency cut-off for the roughness PSD.

5.3. Roughness scattering loss in bandgap fibers vs antiresonant fibers

Inserting the roughness power spectral density of Eq.(30) into Eqs.(26) and (28), we calculate and plot in Fig. 19 the scattering loss of the fundamental mode of the 19c PBGF and NANF of Fig.7 across their transmission windows. With the surface roughness parameters described above, we calculate a scattering loss of 0.4 dB/km for the 19c Fiber and only 0.067dB/km in the NANF at 1550 nm. The minimum scattering loss for the NANF occurs at the longer wavelength of 2.2 µm, and is only 0.027dB/km (Note that 2.2µm is the antiresonance wavelength in the first window). For the NANF, we note the slower decrease of the minimum loss with wavelength across the antiresonant windows ($\sim\lambda^{-0.5}$, see the following section for discussion).

The significantly lower scattering loss in a NANF comes as no surprise, given that antiresonance guidance results in much reduced mode-field intensity near the air-glass interfaces (further discussion below). For the PBGF in which the loss is widely acknowledged to be limited by surface scattering, the loss value we calculate is roughly one order of magnitude lower than the best value reported in surface-mode free fibers operating at 1550 nm [75]. For the fiber reported in [18, 75], with a core diameter of 26µm and a hole diameter to pitch ratio of 0.97, we calculate a scattering loss of ~2 dB/km (see [174]). Its measured loss via cutback revealed a minimum loss of 3.5 dB/km at 1500 nm. The discrepancy between measured and calculated values was first thought to originate either from inaccuracies in reproducing fiber cross-sections for the numerical modeling, or from the uncertainty regarding the surface roughness itself (e.g. it was shown in [18] that modeled loss matched measurements for $Tg/\gamma = 2900$). However, it is increasingly clear that the underlying assumption that surface roughness scattering alone was responsible for the measured attenuation in PBGFs did not always hold. By inducing power transfer between the guided and radiation modes, other structural perturbations such as microbending (which we examine in Section 7) can lead to increased attenuation [187–189]. It is crucial to take such contributions into account in order to build a complete picture of loss in HCFs and help guide the design of ultralow loss fibers.

5.4. Scaling rules

For the purpose of optimizing fiber designs, it is of primary interest to examine how the surface scattering loss scales with key fiber design parameters such as core size and operating wavelength. Such scaling rules are needed to help quickly determine which fiber designs are likely to offer the lowest possible loss for a chosen wavelength of operation. Although the scattering loss at each wavelength ultimately depends on the precise mode field distributions within the fibers and near the air-glass interfaces in particular, useful simplifications can be made. This is because to first order approximation, the field strength near the air-glass interfaces at the core boundary scales with λ/a [54, 115, 155]. If for simplicity we approximate this core boundary with a circle of radius a and assume the mode field is constant on the core boundary , then to first order, the integral in Eq.(26) is proportional to:

$$\oint_{C_m} \vec{U}_k(s) \mathrm{e}^{jk(\rho' \sin\theta(\cos\phi - \phi'))} ds \quad \propto \quad \int_0^{2\pi} \frac{\lambda}{a} \mathrm{e}^{jka\sin\theta(\cos\phi-\phi')} a d\phi' \propto \lambda J_0(ka\sin\theta) \tag{31}$$

The power P_k carried by the mode is proportional to a^2 and it follows therefore that the surface scattering loss is therefore proportional to:

$$\alpha_{ssc} \quad \propto \quad \frac{\lambda^{-4}}{a^2} \int_0^{\pi} \tilde{\Psi}_{1D} \left(\beta - k\cos\theta\right) \lambda^2 J_0^2(ka\sin\theta) \sin\theta d\theta \tag{32}$$

Of the terms in the integral, the PSD from surface capillary waves scales with λ (when no cut-off is imposed) and the remaining integral over θ scales approximately as $1/ka \propto \lambda/a$. Combining these together, we find that the surface scattering loss scales as

$$\alpha_{sc} \propto \frac{\lambda^{-4}}{a^2} \cdot \lambda^2 \cdot \lambda \cdot \frac{\lambda}{a} \propto \frac{1}{a^3} \tag{33}$$

This is an important and somewhat surprising result which suggests that under the approximations made here, the core size is the only important parameter in determining the scattering loss. It is compatible with the well-established and experimentally validated observations with rigidly scaled PBGFs which showed the loss decreasing as λ^{-3} when both the core size and wavelength were scaled in proportion [49, 190]. To further confirm this, we plot in Fig. 20 the scattering loss computed for the PBGF of Fig.7 rigidly scaled to operate at wavelengths from 0.6 to 2.5 µm. We also show the minimum scattering loss in the first and second antiresonant window for the NANF as a function of the core radius a.

Eq.(33) suggests that in principle, the surface scattering contribution to loss in a fiber guiding across multiple spectral regions does not depend strongly on wavelength. In Fig.19, we see that for the NANF under analysis, there is a weaker $\lambda^{-0.5}$ scaling with the wavelength, not too dissimilar to the one found by Roberts *et al.* for solid-core microstructured fibers [48]. This weak wavelength dependence reflects the approximations made in reaching Eq.(33).

5.5. Heuristic model for surface roughness scattering

In this section, we turn our attention to the question whether the surface scattering loss computed rigorously in the above can be approximated to facilitate less computationally intense estimates. To do so, we consider the simpler approximation of isolated and uncorrelated scatterers. Here, we assume that the rough interfaces can be thought of as a collection of independent scattering dipole elements radiating away part of the light incident upon them. Let us assume that the mode $|\psi_k\rangle$ is propagating in a section of length L of fiber which contains the rough air-glass interfaces.

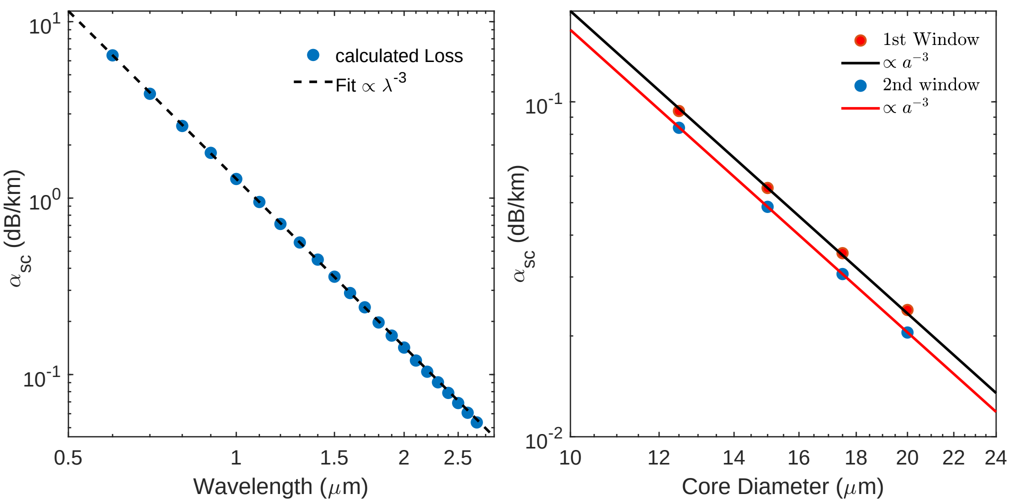

Fig. 20. Scaling rules for the surface scattering loss in PBGFs (left) and NANFs (right). The PBGF of Fig.7 is rigidly scaled for operation at different wavelengths and as a result, our model predicts the well-known experimental results of a λ^{-3} scaling (or more precisely, a^{-3} scaling, see text). For the NANF, the loss minima within the antiresonance windows also scales as a^{-3}.

Following references [54, 191], we postulate that a typical scatterer on this surface has a volume ΔV_s. Its induced dipole moment may therefore be expressed as:

$$\mathbf{p} = \varepsilon_0 \Delta\varepsilon \Delta V_s \cdot \mathbf{E}_k \tag{34}$$

Here, $\Delta\varepsilon$ is the permittivity contrast between air and silica and $\mathbf{E}_k$ is the incident mode's electric field strength at the scatterer location. When the dipole is assumed to radiate in free space, the radiated power is approximated by:

$$\begin{aligned} dP &= \frac{c^2}{12\pi}\left(\frac{\mu_0}{\varepsilon_0}\right)^{\frac{1}{2}}\left(\frac{\omega}{c}\right)^4 |\mathbf{p}|^2 \\ &= \frac{1}{12\pi}\left(\frac{\omega}{c}\right)^4 \Delta\varepsilon^2 \Delta V_s^2 \left(\frac{\varepsilon_0}{\mu_0}\right)^{\frac{1}{2}} |\mathbf{E}_k|^2 . \end{aligned} \tag{35}$$

The total radiated power from a section of length L of the fiber is therefore:

$$P = \frac{1}{12\pi}\left(\frac{\omega}{c}\right)^4 \Delta\varepsilon^2 \Delta V_s^2 \left(\frac{\varepsilon_0}{\mu_0}\right)^{\frac{1}{2}} \frac{1}{\Delta\mathcal{A}} \int_L \mathrm{d}z \oint_C |\mathbf{E}_k|^2 \,\mathrm{d}s \tag{36}$$

where $\Delta\mathcal{A}$ is the average area occupied by a dipole on the interface and C represents the perimeters of the air-glass interfaces in the cross-section. In a further approximation, we will assume that L is short enough that the field strength does not change appreciably over L. If we then express the total power P_k carried by the mode as a Poynting flux, we derive the surface scattering loss per unit length as:

$$\alpha_{ssc} = \frac{P}{P_k L} \sim \frac{1}{6\pi}\left(\frac{\omega}{c}\right)^4 \Delta\varepsilon^2 \frac{\Delta V_s^2}{\Delta\mathcal{A}} \left(\frac{\varepsilon_0}{\mu_0}\right)^{\frac{1}{2}} \frac{\oint_C |\mathbf{E}_k|^2 \, dl}{\iint \mathbf{z} \cdot \mathbf{E}_k \times \mathbf{H}_k^* dS} \tag{37}$$

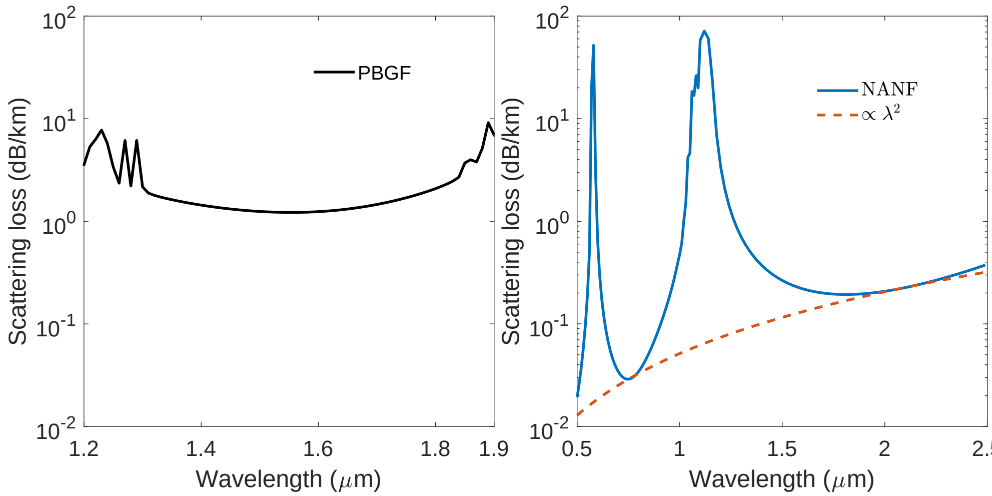

Fig. 21. Scattering loss predicted from the normalized interface field intensity F in the PBGF (left) and NANF (right) of Fig.7. Here, we have taken $\alpha_{sc} = \eta F$ with a constant $\eta = 300$. The estimated scattering loss reaches a minimum of $1.2 dB/km$ in the photonic bandgap fiber at 1.55μm (3x higher than with the rigorous scattering model), whereas in the NANF, the minima in the first and second windows are ~$0.18 dB/km$ and ~$0.03 dB/km$ respectively. The minima across antiresonant windows follow the λ^2 scaling approximately.

The uncorrelated scatterers approximation therefore leads to the conclusion that the surface scattering loss is proportional to the geometry and mode field-dependent quantity:

$$F = \left(\frac{\varepsilon_0}{\mu_0}\right)^{\frac{1}{2}} \frac{\oint_C |\mathbf{E}_k|^2 \, dl}{\mathbf{z} \cdot \iint \mathbf{E}_k \times \mathbf{H}_k^* dS} \tag{38}$$

known as the normalized interface field intensity [49, 71, 191]. This simple quantity has often been used in the literature, to compare the scattering loss performance of HCFs designs, the underlying assumption being that the lower the value of F, the lower the surface scattering loss will be. Despite the simplicity of the assumptions involved in deriving equation (37), it is conceivable that for fibers manufactured with the same process (thus assumed to have the same roughness statistics) and operating at the same wavelength, a simple calibration of the F parameter could be used to estimate loss. We found for example that for 1550 nm PBGFs fabricated in our lab, when assuming that all the loss was due to surface scattering alone, the simple scaling given by

$$\alpha_{sc}\ (dB/km) = \eta F(\mu m^{-1}) \tag{39}$$

often provided an adequate approximation for the fiber loss, with the proportionality coefficient taking the value $\eta = 300$ [129, 192]. We plot in Fig. 21 the surface scattering loss as would be predicted from Eq.(39) for the optimized photonic bandgap fiber and NANF of Fig.7 using a constant, wavelength-independent value $\eta = 300$. With this value, Eq.(39) predicts 1.2 and 0.2 dB/km at 1550 nm for the PBGF and NANF, respectively, a factor of 3 higher than obtained from Eq.(28).

As can be seen, using a constant value of η predicts for the NANF surface scattering loss minima that increase with wavelength, with the minimum loss in the first window higher than that in the second window. This is evidently incompatible with most scattering processes. Therefore,

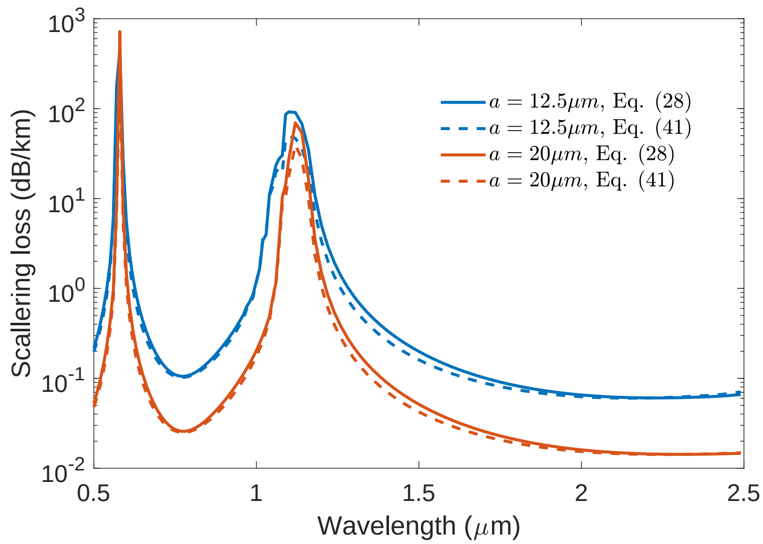

Fig. 22. Comparison between rigorous scattering loss model (solid lines) and the heuristic approximation of Eq.(41) for two NANFs with core diameters 25 μm (blue) and 40 μm (orange).

to capture the most general case, we assign a wavelength dependence to the proportionality coefficient η and write:

$$\alpha_{sc}\ (dB/km) = \eta(\lambda) \cdot F \tag{40}$$

and use the rigorous model of the previous sections to inform the choice of such a dependence. Focusing on the the NANF and by extension other ARFs, we first note that using the same reasoning of section 5.4, the normalized interface field intensity F scales as λ^2/a^3. This is evidenced by the dashed black curve in Fig.21.

To match the the weak wavelength dependence $\sim\lambda^{-0.5}$ (see Fig.19) resulting from the rigorous scattering model, we propose that an adequate estimate of the surface scattering loss can be obtained through

$$\alpha_{sc}\ (dB/km) = \eta_0 \cdot \left(\frac{\lambda_0}{\lambda}\right)^{2.5} \cdot F \tag{41}$$

Exploiting the fact that $\eta_0 = 300$ resulted in losses 3x higher than the rigorous model at 1550 nm, we find that the lower value $\eta_0 = 100$ at a wavelength $\lambda_0 = 1550$ nm provides a reasonable agreement with the rigorous calculations of the previous sections. Fig.22 shows the approximation of Eq.(41) and the surface scattering loss from Eq.(28) for two NANFs with core diameters of 25 and 40 micrometers. Although it is slightly less accurate and underestimates the scattering loss near the resonant wavelengths, the approximation of Eq.(41) appears adequate for rapid surface scattering loss estimates. We emphasize once again that in agreeing with the rigorous scattering model, the revised expression of Eq.(41) predicts lower scattering loss for the PBGFs than previously thought. We believe this is in line with the new understanding of other loss contributions previously unaccounted for but which we explore in the remainder of this paper.

Although not too dissimilar to the often used formula $\eta \cdot F \cdot (\lambda_0/\lambda)^3$, the revised formula Eq.(41) provides a more accurate approximation to the surface scattering loss. We emphasize that ultimately, calculating surface scattering loss from the normalized interface field intensity F is at best heuristic, but can be helpful to compare contributions from scattering in different fibers

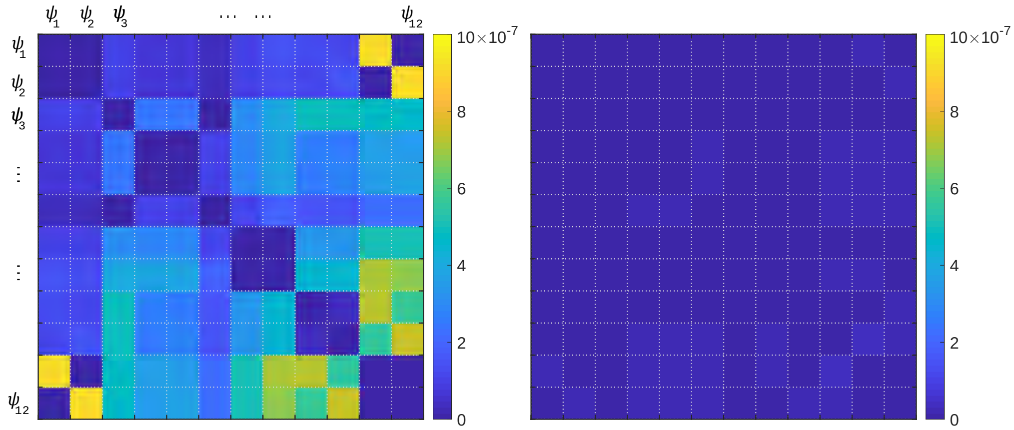

Fig. 23. Roughness scattering-induced intermodal coupling in the PBGF (left) and NANF (right) of Fig.7. The power transfer between the modes occurs predominantly between modes of the same azimuthal symmetry. Like loss, it is higher in PBGFs than in NANFs.

and to perform rapid loss estimates where needed.

5.6. Roughness induced inter-modal coupling

In addition to causing loss via coupling to radiation, the surface roughness scatters optical power from one guided mode of the fiber to another, resulting in intermodal interference (IMI). This can adversely affect the performance of telecom links [193–196]. The rate of intermodal power exchange can be calculated from our treatment of scattering loss in section 5.1. It is known from classical theory that the induced current density $\mathbf{J}_k(s, z)$ resulting from the propagation of mode $|\psi_k\rangle$ will excite another discrete mode $|\psi_l\rangle$ with unitless amplitude given by [197]:

$$a_{kl} = \int_V \mathbf{E}_l^* \cdot \mathbf{J}_k(s, z) dV \tag{42}$$

It follows from here that the power coupling coefficient per unit length to mode $|\psi_l\rangle$ is [155, 198, 199] :

$$h_{kl} = \frac{1}{L}\langle a_{kl} a_{kl}^* \rangle = \omega^2 \varepsilon_0^2 \tilde{\Psi}_{1D} (\beta_k - \beta_l) \times \\ \sum_m \left| \oint_{C_m} \left(\Delta\varepsilon_r \mathbf{E}_{\parallel l}^*(s) \cdot \mathbf{E}_{\parallel k}(s) - \Delta\frac{1}{\varepsilon_r} \mathbf{D}_{\perp l}^*(s) \mathbf{D}_{\perp k}(s) \right) ds \right|^2 \tag{43}$$

As modes $|\psi_k\rangle$ and $|\psi_l\rangle$ propagate in the fiber exchanging power at a rate h_{kl}, it results in added noise in the form of IMI, but also additional loss when one of the modes has higher attenuation. We examine propagation in the presence of intermodal coupling by means of coupled power theory in section 7 (see also [188]), but we show in Figure 23 the calculated h_{kl} matrix from roughness scattering for the first 4 mode groups (LP_{01},LP_{11}, LP_{21}, LP_{02}, 12 guided modes in total) of the PBGF and NANF of Fig. 7 at 1550 nm.

As can be seen, roughness-induced mode-coupling is significantly stronger in the PBGF than in the NANF. This originates, as before, from the lower field at the air-glass interfaces. The highest coupling rate from the fundamental mode is to the LP_{02} mode of the same polarization, amounting to $9 \times 10^{-7} m^{-1}$ in the PBGF but only $1.6 \times 10^{-8} m^{-1}$ in the NANF of similar core sizes. This mode however, often suffers from high differential loss (see following section). The lowest loss higher order mode group is the LP_{11} mode for which we calculate a total coupling coefficient of $3 \times 10^{-7} m^{-1}$ for the PBGF and $2 \times 10^{-8} m^{-1}$ for the NANF. Finally, we note that roughness-induced coupling of one polarization of the fundamental mode to the other is significantly lower in both fibers, amounting to $1.5 \times 10^{-9} m^{-1}$ in the PBGF and $10^{-10} m^{-1}$ in the NANF, respectively. Such low levels represent a fundamental limit to the polarizaton mode coupling in HCFs, though other perturbations may exacerbate this [200].

6. Loss in higher order modes

The foregoing analysis has so far pertained to the pair of degenerate fundamental HE_{11} modes in hollow-core fibers since they typically offer the lowest loss. All of the intrinsic loss mechanisms we have discussed scale favorably with larger core sizes, i.e., these loss contributions decrease when the core is enlarged. However, fibers with larger core size support an increasingly high number of transverse modes of propagation [10, 58, 201, 202]. Unlike in solid-core multimode fibers where the attenuation is virtually independent of mode order when they are far from cut-off, in hollow-core fibers, there exists an intrinsic differential attenuation between the fundamental and higher order modes [61, 202]. However, the level of differential loss can be enhanced through engineering the structure of the cladding to achieve effective single mode operation even in large core fibers [88, 122, 124]. The reverse is also possible, and in principle, the cladding region can be designed in such a way that the differential loss between the fundamental and higher order modes is minimized, thereby achieving few-mode/multi-mode operation [203, 204].

In section 2, we briefly discussed why higher order modes in hollow-core fibers must inevitably suffer from higher leakage loss (see Section 2). From the partial refraction picture, higher order modes correspond to rays that impinge on the core cladding interface at a steeper angle and are thus reflected less efficiently, leading to higher confinement loss. A qualitative analysis from the inhibited-coupling perspective yields the same conclusion. Higher order modes have a stronger overlap with cladding modes and simultaneously have propagation constants closer to those of the cladding modes, thus leading to higher confinement loss (see Eq. (13)). In the simplest of hollow-core fibers analyzed by Marcatili and Schmeltzer [115], the differential confinement loss increases with the mode order, scaling as u_{nm}^2 (recall that u_{nm} is the m-th zero of the Bessel function $J_{n-1}(x)$, $u_{01} \approx 2.4048, u_{11} \approx 3.8317, u_{21} \approx 5.1356, u_{02} \approx 5.5201, \ldots$ etc) . For the model antiresonant fibers studied by Bird, Eqs.(10) and (11), show that for a structure with l antiresonant layers, the leakage loss scales with the more order as u_{nm}^{l+2}. In practical fiber designs such as photonic bandgap or antiresoant fibers, quantifying the loss of the higher order modes is not as straightforward. Depending on its complexity and the guidance mechanism, the cladding structure supports modes whose interaction with the core-guided modes is not easily predicted.

To illustrate the differential confinement loss in HCFs, we plot in Fig. 24 the calculated confinement loss for the first four mode groups of the PBGF and NANF shown in Fig. 7. For simplicity, we adopt the LP terminology, but it should be understood the modes are not linearly polarized in practice.

In the photonic bandgap fiber, as the order of the mode increases, its propagation constant decreases and becomes closer to that of cladding modes at the bottom of the photonic bandgap (see Fig. 2), leading to higher leakage. However, for the first 12 modes of the 19c fiber examined here, confinement loss remains below 100x the confinement loss of the fundamental mode, which translates to less than 10^{-3} dB/km near the center of the photonic bandgap. Interestingly, in the particular structure examined here (Fig.7), one of the LP_{11} modes, the TE_{01} mode, has lower leakage loss than the fundamental modes at longer wavelengths beyond about 1.55μm, a behaviour similar to what is observed in hollow metallic waveguides [115].

In contrast, in the NANF, the leakage loss grows rapidly with mode order. For the selected structural parameters (see Fig. 7), we find that the lowest loss LP_{11} mode, the TE_{01} mode has a minimum confinement loss 23x higher than that of the fundamental mode near the center of the

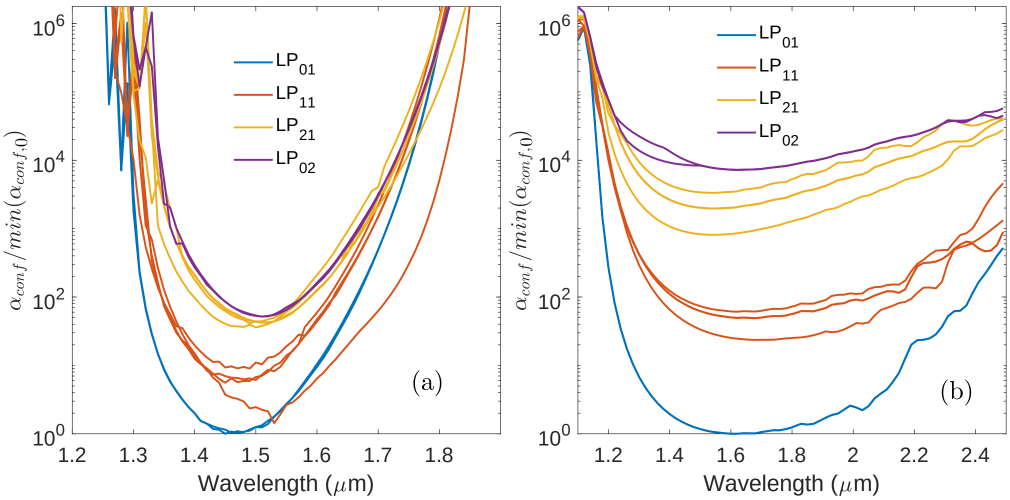

Fig. 24. Confinement loss in higher order modes in hollow-core optical fibers. The Confinement loss calculated for the first four mode groups is normalized to the minimum leakage loss of the fundamental mode . (a) Mode-dependent confinement loss in the PBGF of Fig.7 and (b) Mode-dependent confinment loss for the NANF of Fig.7. The confinement loss increases more slowly with mode order in the PBGF than in the NANF due to the absence of phase-matched lossy cladding modes.

transmission window. In this low-loss spectral region. the LP_{11} mode group averages a leakage loss of ~30dB/km, 46x higher than that of the fundamental mode. All other HOMs beyond have higher confinement loss than ~1 dB/m. It appears therefore that this 6-tube NANF may effectively be regarded as a two mode fiber [109]. It is worth mentioning that the cladding can be further optimized to increase the leakage of the LP_{11} mode too, for example by changing the ratio z/a (see Fig.7 above and Fig (11) of ref. [101], or adopting a geometry with 5 sets of tubes [95, 101, 205].

Next we look at potential contributions from absorption and bulk scattering in the glass to the loss of higher order modes. We plot in Fig. 25 the material loss suppression factor ζ for higher order modes in the PBGF and NANF of Fig. 7. In both fiber types, at wavelengths away from the edges of the transmission windows, we see that ζ is roughly proportional to u_{nm}^2. A first order perturbation analysis reveals that since normalized field strength near the core boundary is a zero of the order of $u_{nm}\lambda/a$, the integral of Eq. (18) scales as $u_{nm}^2\lambda^2 t/a^3$ (see section 3). As absorption and glass material loss only scale as u_{nm}^2, we conclude that relying on these loss mechanism will be ineffective at rapidly stripping undesired higher order modes.

Finally, we consider the contribution from surface roughness scattering. Using Eqs.(26) and (28) , we compute the surface roughness scattering loss for the first four mode groups of the PBGF and NANF we have considered so far. The results we obtain are shown in Fig. 26. Just like with absorption, we see that in both fibers, the loss from surface scattering scales approximately as u_{nm}^2. We also observe, in the case of PBGF in particular, the degenerate modes making the LP-like HOM groups have different scattering loss contributions. In the LP_{11}-like mode group for example, the TE mode offers the lowest loss near the middle of the bandgap and the TM mode the highest due to the large discontinuity of its electric field near the core boundary.

We conclude from the preceding analysis that of the intrinsic loss mechanisms in HCFs, material loss and surface roughness scattering are fundamentally limited to scaling with the transverse mode order as u_{nm}^2. However, the cladding can be engineered to control the differential leakage loss between the transverse modes, e.g., through phase matching undesired core modes

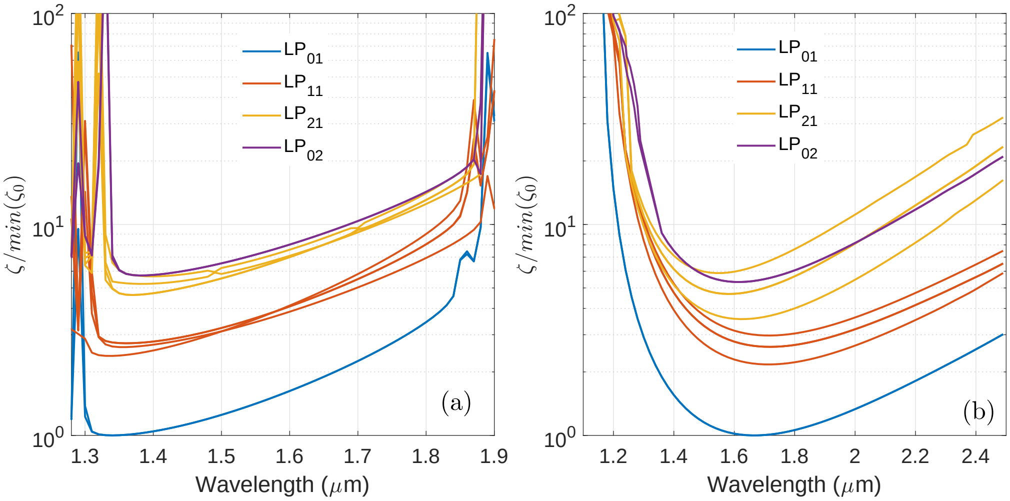

Fig. 25. Glass absorption/bulk scattering suppression factor for higher order modes in the PBGF (left) and NANF (right) of Fig.7 . In both fiber types, contribution from scattering and absorption within the glass scale approximately with the mode order as u_{nm}^2.

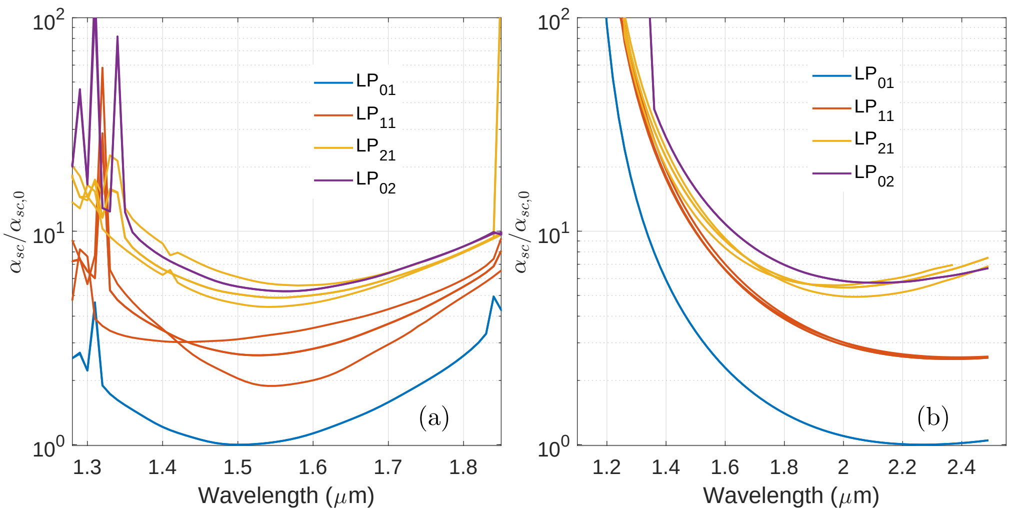

Fig. 26. Surface scattering loss for the higher order modes in the PBGF (left) and NANF (right) of Fig.7. Here too, the loss scales approximately with the mode order as u_{nm}^2, i.e., is roughly 2.5 times higher for the LP_{11} mode, 4.6 times higher for the LP_{02}, etc.

with lossy cladding modes. This understanding has been exploited to achieve effective single mode fibers, whether in PBGFs via the introduction of shunt cores [124] or in antiresonant fibers through the control of the size of the cladding tube [88, 101].

In PBGFs without these higher-order mode stripping shunt cores (such as in [19, 124]), at wavelengths away from the edges of the bandgap or surface modes, leakage is low for all modes (below 10^{-3} dB/km for the example we considered). The total loss is essentially dominated by surface scattering (unless operating where the glass is highly absorptive). When this is the case, the total loss scales approximately with mode order as u_{nm}^2. This is supported by experimental loss measurements in 37c PBGFs used for mode-division multiplexed data transmission for example [62].

In antiresonant fibers, in spectral regions where there is no absorption, the contribution from leakage tends to be higher than scattering. Since the structure can be readily engineered to achieve phase matching between lossy tube modes and core modes (e.g. through the choice of the size of the hollow regions in the cladding), the total loss of all HOMs can be made orders of magnitude higher than that of the fundamental mode, resulting in effective single mode operation after an appropriate propagation distance. On the other hand, by using smaller cladding tubes or subdividing the tubes into smaller hollow regions, one can reduce the loss of higher order modes [203, 204]. In NANFs, for example, the choice of the size of the nested tubes plays an important role in determining the loss of higher order modes [101]. The underlying principle is that of controlling the propagation constant difference between core and cladding modes as well as their spatial overlap.

Part II

Extrinsic loss mechanisms

Having analyzed the key intrinsic loss mechanisms in hollow-core fibers, we now turn our attention to those contributions to loss that result from imperfections in fabrication such as longitudinal non-uniformities, or from the macroscopic deployment conditions of the fiber such as bends. Although these can in principle be reduced by improvements in fiber fabrication processes, improved packaging strategies (e.g. UV curable coatings) or the relaxation of deployment criteria and conditions, their contribution to loss remains significant in most practical scenarios. Understanding them, particularly how they scale with key fiber parameters, is therefore of paramount importance in informing the fiber design and manufacturing processes. In this part of the paper, we first focus on random microbends which appear to be the most important extrinsic contributor to loss and can be addressed through adequate fiber packaging. We then briefly survey other perturbations which may be present in the fiber but which perhaps can be addressed through finer control of the drawing process. Finally, we describe macrobending loss that the fiber incurs when it is coiled under a constant diameter for a long distance. Such bend loss is extremely important in a range of applications where the fiber must be in a compact form, see for example [33].

7. Random microbends

Microbending refers to microscopic displacements of the fiber axis that cause it to depart from an ideal straight trajectory. They often result from random lateral loads on the fiber, for example when it is wound under tension on a drum with a rough surface under tension or when pressing against a strength member within a cable [206]. In the early days of research into conventional single mode fibers, it was recognized that if unadressed, microbending would cause severe additional loss to (~100 dB/km) and exacerbate polarization mode dispersion [206–208]. In solid-core multimode fibers or even multicore fibers, microbending induces strong intermodal power transfer, thereby degrading the fiber's performance in data transmission systems. Essentially, microbends cause scattering from a mode of interest to other guided modes and to radiation, thus resulting in intermodal coupling and excess loss [209–211]. Through decades of research, it is now well-established that there are three main routes to address microbending in standard solid-core optical fibers fibers. The first is to increase the diameter of the fiber and its polymer coatings to give the fiber stiffness and thus increase its ability to resist bends. The second is to use softer primary coatings which effectively act as a shock absorber preventing external mechanical loads from displacing the fiber axis. The third route consists of engineering the refractive index profile of the fibers in such a way that it results in a large separation between the propagation constant of the guided mode of interest and that of the radiation modes to which the microbending-induced coupling is the strongest [207, 212, 213]. *A priori*, these solutions ought to work also for hollow-core fibers [189]. However, the extent to which this might be the case is not yet well known since a comprehensive analysis of microbending in HCFs has not hitherto been performed. This section presents such an analysis.

We start by examining a single microbend perturbation also studied in detail in [214, 215]. Effectively, this consists of a short fiber section of length dz being bent with radius of curvature R_b, thus equivalent to a directional change $\phi = \frac{dz}{R_b}$ for the fiber axis (see Fig. 27). When the fiber mode $|\psi_k\rangle$ carrying unit power (i.e. normalized according to Eq.(16)) is incident on the bend, provided that ϕ is small, a perturbative analysis tells us that at the end of the bent section, the mode $|\psi_l\rangle$ will be excited with amplitude :

$$a_{kl} = \left\langle \psi_l \middle| \Delta\hat{A} \middle| \psi_k \right\rangle dz \tag{44}$$

where $\Delta\hat{A}$ is a bend perturbation operator which has been derived using a coupled-mode analysis in references [54, 153, 168, 214, 215]. Assuming the bend is along the x-axis, the amplitude coupling coefficient above can be written explicitly as the integral [54]:

$$a_{kl} = \left\langle \psi_l \middle| \Delta\hat{A} \middle| \psi_k \right\rangle dz = dz \iint \begin{bmatrix} E_x \\ E_y \\ E_z \\ H_x \\ H_y \\ H_z \end{bmatrix}_l^\dagger \frac{\omega x}{c R_b} \begin{pmatrix} \varepsilon & & & & & \\ & \varepsilon & & & & \\ & & -\varepsilon & & & \\ & & & \mu & & \\ & & & & \mu & \\ & & & & & -\mu \end{pmatrix} \begin{bmatrix} E_x \\ E_y \\ E_z \\ H_x \\ H_y \\ H_z \end{bmatrix}_k dxdy \tag{45}$$

In waveguides with circular symmetry in the cross-section, x can be written in a cylindrical coordinate system (ρ, θ, z) as $x = \rho\cos(\theta)$ and it follows that since all the modes have a dependence $e^{jm\theta}$ (m is the azimuthal mode number), only modes satisfying the selection rule $\Delta m = \pm 1$ will be coupled as a result of the bend [165]. Although the geometry of HCFs generally do not have circular symmetry (typically six-fold for the PBGF, N-fold for antiresonant fibers with N being the number of sets of cladding tubes), this selection rule also holds approximately (as shown for example in the coupling matrix of Fig.28 discussed below).

For such a single bend, it is of interest to estimate the total power coupled out of the incident mode as a result of the perturbation. First, from the excited amplitude of Eq.(45), we calculate the power coupled from mode $|\psi_k\rangle$ to mode $|\psi_l\rangle$ as:

$$\Delta P_{k\to l} = a_{kl}^* a_{kl} = \left\langle \psi_k \middle| \Delta\hat{A}^* \middle| \psi_l \right\rangle \left\langle \psi_l \middle| \Delta\hat{A} \middle| \psi_k \right\rangle \tag{46}$$

The total power coupled out of the mode $|\psi_k\rangle$ is therefore a summation over all the destination modes and is obtained as (see [214–216]):

$$\Delta P_k = \sum_{l\neq k} \Delta P_{k\to l} = \sum_{l\neq k} \left\langle \psi_k \middle| \Delta\hat{A}^* \middle| \psi_l \right\rangle \left\langle \psi_l \middle| \Delta\hat{A} \middle| \psi_k \right\rangle = \phi^2 \left(\frac{\omega}{c}\right)^2 \left\langle \psi_k \middle| x^2 M^2 \middle| \psi_k \right\rangle \tag{47}$$

where we have exploited the completeness rule, i.e., $\sum |\psi_l\rangle\langle\psi_l| = 1$, and where M is the diagonal matrix in Eq.(45). This interesting result shows that the total power coupled out of the mode

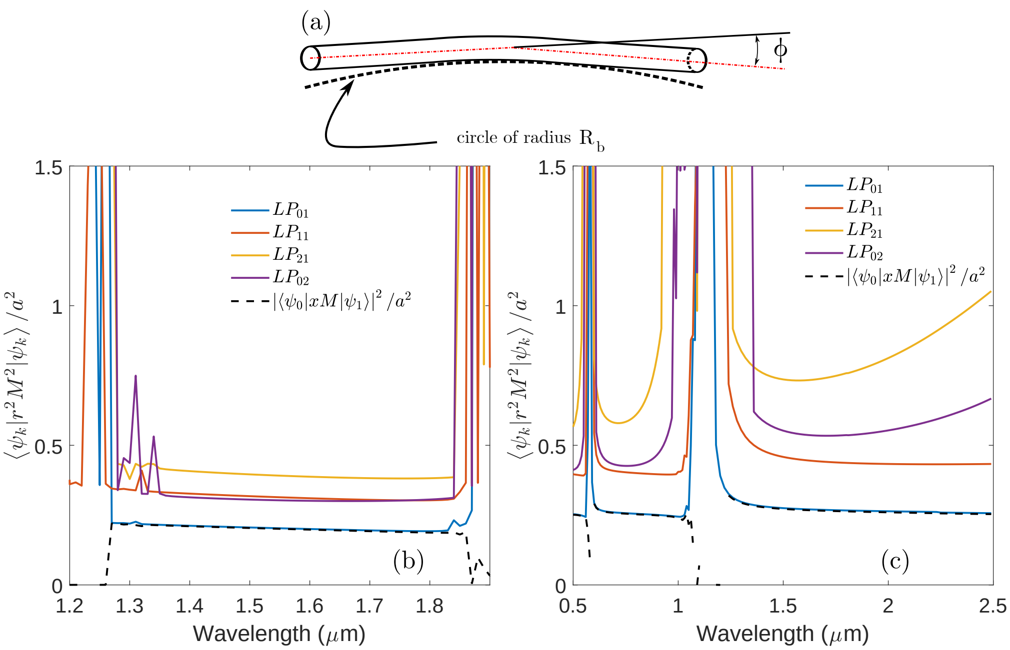

Fig. 27. Normalized Mode spot areas or normalized total power loss at a directional change in hollow-core optical fibers. (a) illustration of a directional change ϕ around a bend of radius R_b. (b) Mode spot areas for the first 4 mode groups of the PBGF and (c) for the NANF. The mode spot area, and thus microbend sensitivity increases rapidly with mode order. The dashed black lines show the normalized power coupled from the fundamental mode to the LP_{11} mode group.

$|\psi_k\rangle$ depends only on the quantity $\langle\psi_k|x^2M^2|\psi_k\rangle$. This quantity is effectively a mode-field weighted average of x^2 and thus has the meaning of an area. For standard single mode-fibers, Petermann refers to this as the mode spot area [217–219]. The total power coupled out of the incident mode is thus proportional to its mode spot area. To account for the fact that hollow-core fibers typically do not have a circular symmetry, we assume microbends may occur along any azimuthal direction in the fiber cross-section and thus write:

$$\Delta P_k = \frac{1}{2}\phi^2\left(\frac{\omega}{c}\right)^2\langle\psi_k|r^2M^2|\psi_k\rangle \tag{48}$$

Figure 27 shows the normalized mode spot area $\langle\psi_k|r^2M^2|\psi_k\rangle/a^2$, or mode spot area, for the first 12 modes of the PBGF and NANF of Fig.7. The spot areas are calculated from the mode-field data obtained from the finite element solver. Unsurprisingly, we see the mode spot area increase with mode order, indicating that higher order modes will incur greater bend-induced penalties. We also plot for both fibers (dashed black lines) the normalized power transferred from the fundamental mode $|\psi_0\rangle$ to the LP_{11} modes denoted $|\psi_1\rangle$ for simplicity (we have summed over the TE_{01}, TM_{01} and the degenerate HE_{21} modes). Note how this quantity, $|\langle\psi_1|xM|\psi_0\rangle|^2/a^2$ is virtually identical to the spot area of the fundamental mode, showing that nearly all of the power coupled out of the fundamental mode at a directional bend is transferred to the LP_{11} modes [216]. This is important for some useful approximations which we will make next.

For the fundamental mode in both fibers, the mode spot area $\langle\psi_k|r^2M^2|\psi_k\rangle$ does not change appreciably with the wavelength within the transmission window. This is in contrast to single mode weakly guiding fibers where the mode spot area grows rapidly with wavelength due to the mode field expanding further into the cladding [219, 220]. Since the unnormalized ΔP_k

has an additional factor $k^2 = 1/\lambda^2$, it follows that unlike in SMFs, the total power lost from a mode at a directional change in HCFs is higher at shorter wavelengths. As shown in the following discussion, microbending loss in hollow-core fibers is more prominent at shorter wavelengths as a result. Interestingly, despite their similar core sizes, the nature of the guidance mechanism results in the photonic bandgap fiber having a 20% smaller spot area $\left\langle \psi_k \middle| r^2 M^2 \middle| \psi_k \right\rangle$ than the corresponding NANF, giving it a small advantage in lower microbending loss and microbending-induced mode coupling (see also Fig. 30).

We now consider a section of fiber of length L is subject to random microbends with local random curvature radius $R_b(z)$. The foregoing analysis says that when L is short enough that the amplitude of incident mode $|\psi_k\rangle$ is considered constant, then at the end of this section of fiber, the mode $|\psi_l\rangle$ is excited with an amplitude given by:

$$a_{kl} = \int_0^L \left\langle \psi_l \middle| \Delta\hat{A} \middle| \psi_k \right\rangle dz = \int_0^L \left\langle \psi_l \middle| \frac{1}{R_b(z)} \frac{\omega}{c} x M \middle| \psi_k \right\rangle dz \tag{49}$$

The rate of power coupling between the two modes per unit length is therefore:

$$h_{kl} = \frac{1}{L} \left\langle a_{kl}^* a_{kl} \right\rangle \tag{50}$$

where $\langle \ldots \rangle$ is an ensemble average. As before (see section 5), this simplifies to:

$$h_{kl} = \left(\frac{\omega}{c}\right)^2 \left| \left\langle \psi_l \middle| \frac{\omega}{c} x M \middle| \psi_k \right\rangle \right|^2 \Xi(\beta_k - \beta_l) \tag{51}$$

where $\Xi(\kappa)$ is the power spectral density of the curvature function $1/R_b(z)$ [219]. Such a curvature spectrum is not easily determined in practice. However, in conventional solid-core fibers for which microbending effects have been studied more extensively, researchers have commonly assumed a power spectrum of the form:

$$\Xi(\kappa) = \frac{A}{\kappa^{2p}} \tag{52}$$

where A is a constant characterizing, for example, the magnitude of the lateral loads causing the microbends, the ability of the fiber's packaging to dampen such loads,the number of such local point loads per unit fiber length and p is an exponent describing how rapidly the PSD decreases with increasing spatial frequency [207, 212, 221–225]. Considering for example uncorrelated point loads on the fiber within a cable, Olshansky finds that $p = 2$ [221]. However, fitting of experimentally measured microbending loss data for single mode fibers has suggested higher values for p between 2 and 5 [225–227]. For simplicity we will assume a value $p = 2$ in the following discussion.

In the most general case, the impact of random microbends on the evolution of the optical power carried by each mode is described by coupled power theory which states that [165, 228]:

$$\frac{dP_k(z)}{dz} = -\alpha_k P_k(z) + \sum_{l=1}^{N} h_{kl} \left(P_l(z) - P_k(z)\right) \tag{53}$$

where α_k is the loss of the mode $|\psi_k\rangle$, $P_k(z)$ its power as a function of z and h_{kl} are the power coupling coefficients of Eq.(51). When solving this system of coupled equations, it has been found that after a certain distance, a *steady-state* is reached and the relative distribution of power among the modes regardless of initial conditions remains unchanged [228]. In the steady-state, all the modes evolve with the same loss rate, which is higher than the loss of the fundamental mode alone and is called the *steady-state loss*.

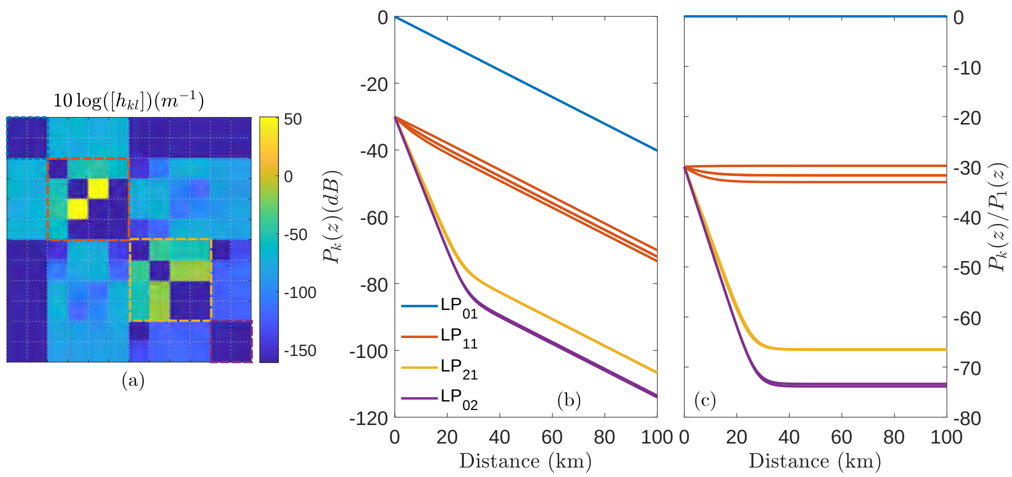

Fig. 28. Example of microbending-induced mode coupling matrix and modal power evolution with distance in the example PBGF. (a) The microbending coupling matrix showing the ±1 selection rule for bend-induced coupling between mode groups (b) Solution to the coupled power equation and (c) modal power normalized to fundamental mode power. The assumed power spectral density for the microbend perturbations is $\Xi(\kappa) = A/\kappa^{2p}$ with $A = 10^6$ and $p = 2$. With this perturbation,it follows that microbending induces about ~-30dB power in the LP_{11} modes, showing that microbending can lead to considerable IMI in PBGFs because of the low differential loss.

An example of a numerical solution of Eq.(53) is shown in Fig.28. We have considered the PBGF of Fig.7 at 1550 nm for which we first calculated the microbending induced coupling matrix $[h_{kl}]$ for the first four mode groups. For our illustration here, we chose a microbending perturbation power spectrum obeying Eq.(52) with $A = 10^6$, $p = 2$. As can be seen from the coupling matrix, microbends couple power from one core mode group to a neighbouring one which satisfies the condition $\Delta_m = \pm 1$ as expected from symmetry considerations. The fundamental modes thus couple predominantly to the LP_{11} modes, whereas the latter couples to LP_{01},LP_{21} and LP_{02} modes and so on. However, we note for this fiber that microbending appears to induce a strong coupling between modes within the same mode group, particularly within the LP_{11} and LP_{21} mode groups as can be seen. Using this coupling matrix, we solved Eq.(53) numerically for propagation over 100 km. We assumed initial conditions whereby the fundamental mode is launched into the fiber with every other mode excited at the -30 dB level below it. In the first twenty kilometers or so, the slightly higher loss HOMs (LP_{21} and $_{02}$, both only ~2 dB/km on average) decay at a rate given by their respective loss coefficients (see section 6). This decay is followed by power transfer to these modes from those with lower loss due to microbending. After about 30 km of propagation, a steady state is reached and thereafter, all the modes decay at the same rate and their relative powers compared to that of the fundamental mode is constant. This decay rate is the steady-state loss.

Fig. 29 shows the steady state loss calculated for the photonic bandgap fiber and NANF of Fig.7 as a function of wavelength under two scenarios. First we consider the same perturbation with $A = 10^6$, $p = 2$ and a perturbation that is 100 times stronger, i.e., $A = 10^8$, $p = 2$. In the photonic bandgap fiber, the loss penalty from microbending is negligible as the steady-state loss value is nearly identical to the intrinsic loss of the fiber (all the curves overlap). This remains true even for the stronger perturbation with $A = 10^8$. The result is not surprising given the low differential loss between the modes of the PBGF and indicates therefore that the most important

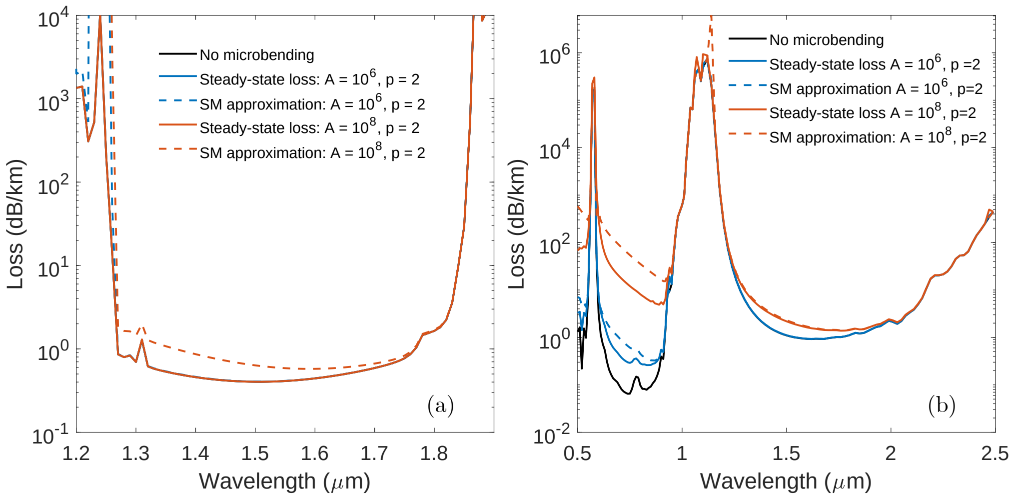

Fig. 29. Microbending-induced loss penalty in the PBGF (a) and NANF (b) from solving the coupled power equations (53) for the first 12 guided modes. (a) PBGF: With its low differential loss, the assumed perturbation spectra do not induce appreciable added loss for the fundamental mode (all the curves overlap exactly, except for the inadequate single mode approximation discussed below). The biggest penalty is instead intermodal coupling.(b) NANF: In the first window, the single-mode approximation agrees well with the steady-state loss (the dashed curves overlap with the solid ones) but is less reliable in the second window at shorter wavelengths.

impact of microbending in this fibre type is intermodal power coupling, which would be a source of noise when the fiber is used in long-distance telecoms for . For the NANF, We see that in the first antiresonant window, the weaker perturbation does not induce a noticeable loss penalty whereas such added loss is already present in the second antiresonant window. The stronger perturbation leads to loss penalties across both antiresonant windows, with higher loss at shorter wavelengths as discussed previously. The dashed lines in the plot are single mode approximations which we discuss next.

7.1. Single mode approximation

In a host of applications using hollow-core fibers, it is often required that the fiber is effectively single-moded. In practice, this means imposing high loss on all higher order transverse modes in the core. When light coupled from the fundamental to any other higher order core mode or cladding mode is effectively lost, the additional loss incurred by the fundamental mode due to microbends can be obtained by summing up the power coupling coefficients as:

$$\alpha_\mu = \sum_l \left(\frac{\omega}{c}\right)^2 \left|\left\langle \psi_l \,\middle|\, \frac{\omega}{c} x M \,\middle|\, \psi_0 \right\rangle\right|^2 \Xi(\beta_0 - \beta_l) \tag{54}$$

The summation extends over all the lossy HOMs and takes the meaning of an integration over the continuum of radiation modes. A further simplification can be made to this expression when this effectively single-mode condition holds and the power spectrum $\Xi(\kappa)$ decreases with spatial frequency, i.e., $d\Xi(kappa)/d\kappa < 0$, as is the case for example from Eq.(52). We have established most of the power lost at a single bend from the fundamental mode is coupled to LP_{11} modes. As these modes also happens to have the smallest $\Delta\beta$ with the fundamental mode, so that

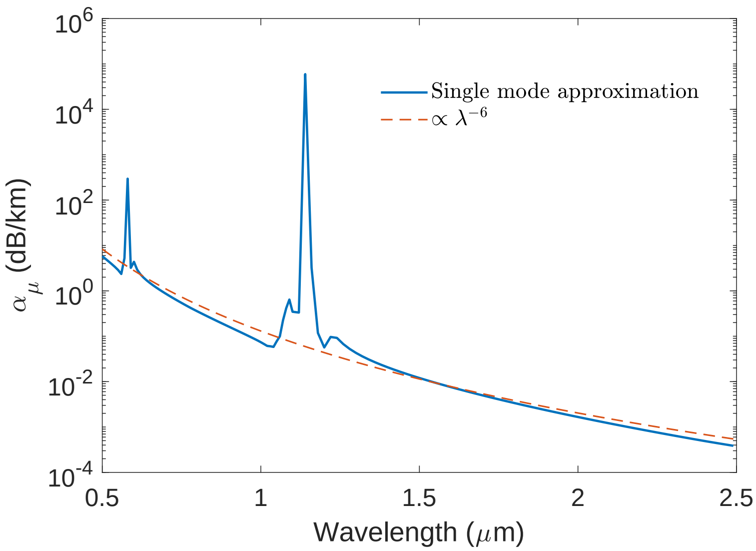

Fig. 30. Single-mode approximation to microbend loss in the NANF of Fig. 7. It is assumed here that all the modes supported by the fiber other than the fundamental mode can be regarded as radiation modes, giving effectively an upper limit for the microbend loss. With the assumed PSD, the loss in the NANF scales approximately as λ^{-6}

$\Xi(\beta_0 - \beta_1)$ is the highest. It follows therefore that an upper bound to the loss can be obtained as:

$$\alpha_\mu = \frac{1}{2}\left(\frac{\omega}{c}\right)^2 \left\langle \psi_0 \middle| r^2 M^2 \middle| \psi_0 \right\rangle \Xi(\beta_0 - \beta_1) \tag{55}$$

This expression is similar to Petermann's formula [217, 218, 220] for standard single mode fibers which has been used as a first order approximation to the microbending loss. The dashed lines in Fig.29 are the sum of the intrinsic loss contributions and the microbending loss computed from the single mode approximation of Eq.(55). The microbending loss predicted by this expression is plotted in Fig.30 for clarity for the NANF with a curvature power spectrum given by E.(52) with $A = 10^6$ and $p = 2$.

When the fiber is effectively single-mode, Eq.(55) allows for a powerful insight into how the microbending loss scales with core size and wavelength. First, we note that the fundamental mode-field distribution in hollow-core fibers results in $\left\langle \psi_0 \middle| r^2 M^2 \middle| \psi_0 \right\rangle / a^2$ being constant with wavelength (see Fig.27). From simple analytical expressions giving the propagation constant of the guided modes derived by Marcatili [115], it follows that to the to the first order, $\beta_0 - \beta_1 \approx \frac{u_{11}^2 - u_{01}^2}{2} \frac{1}{ka^2}$. Finally, assuming the perturbation power spectrum follows Eq.(52), the single mode approximation of Eq.(55) scales as:

$$\alpha_\mu \propto \frac{1}{\lambda^2} \times a^2 \times \frac{1}{\left(\frac{\lambda}{a^2}\right)^{2p}} \propto \frac{a^{2+4p}}{\lambda^{2p+2}} \tag{56}$$

For $p = 2$, the microbending loss scales as a^{10}/λ^6, which is a very strong dependence on the core size.

The steep scaling relationship with the core size explains why the core cannot be enlarged indefinitely in HCFs to reduce the intrinsic loss contributions without penalty. The $1/\lambda^6$ scaling implies that the total loss increases very sharply at short wavelengths. In our NANF example, when the single mode approximation holds, loss which is 0.01dB/km at 1.5µm increases to ~1dB/km at 0.7µm. This may point to one of the reasons why it is often difficult to simultaneously achieve low-loss in the same fiber in the infrared and in higher antiresonant windows at shorter wavelengths.

When the curvature power spectrum of the microbending perturbation decreases with spatial frequency, Eq.(55) shows that an effective approach to reducing microbending penalties is by enlarging $\Delta\beta = \beta_0 - \beta_1$. In standard solid core single mode fibers, β_1 is replaced by $\bar{\beta}_r$ understood as the average propagation constant of the radiation modes to which light is coupled. Whilst in SMFs, low refractive index trenches outside the core have proved effective at enhancing $\beta_0 - \bar{\beta}_r$ and reducing the microbending loss [212, 229], $\beta_0 - \bar{\beta}_1$ in HCFs is determined by the core size and there is no obvious route to enlarge it through engineering the cladding geometry.

7.2. Impact of fiber packaging

An effective route to reducing microbending loss in standard single mode fibers is through adequate packaging of the fiber [207]. Nowadays, the most widely adopted strategy is the application of carefully developed and optimized UV-curable polymeric coatings onto the fiber during fabrication [207]. The combination of a soft primary coating which serves in a way as a shock absorber for microbend-inducing lateral loads on the fiber, and hard secondary coating to facilitate fiber handling and processing is now industry standard for telecom fibers [213].

Over the years, many studies have explored and optimized the design of such a dual coating to effectively shield the standard solid-core fibers from external loads. In his seminal work on the topic, Gloge showed that essentially, the coating assembly behaves as a low-pass filter for external perturbations whereby components with spatial frequency higher than a cut-off given by fiber stiffness and coating moduli are effectively absorbed by the coatings [207]. Further refinements have now shown that the effectiveness of the fiber's packaging in shielding the fiber from distributed external perturbations can be captured by a mechanical transfer function (MTF). The curvature power spectrum of the fiber axis is thus generally expressed as [225]:

$$\Xi(\kappa) = MTF(OD, t_p, t_s, E_p, E_s, \kappa)\Xi_{ext}(\kappa) \approx \frac{A(OD, t_p, t_s, E_p, E_s)}{\kappa^{2p}} \tag{57}$$

where OD is the bare glass fiber diameter, t_p, t_s, E_p and E_s the thicknesses and Young's moduli of the primary and secondary coatings respectively, and $\Xi_{ext}(\kappa)$ is the power spectrum of the external perturbations. Deriving an expression for the MTF is beyond the aim of this paper and we would refer the reader to the works in [207, 213, 221, 225, 230, 231]. From this literature however, it is possible to express it as proportional to:

$$MTF \propto OD^{-6}(t_p + t_S)^{-x}(E_p/E_s)^y \tag{58}$$

where x and y are some characteristic constants usually obtained from statistical experimental data. Because the spatial frequencies that are responsible for coupling from fundamental (i.e, $\beta_0 - \beta_1$) are much smaller than in single mode fibers, controlling the MTF in HCFs is of crucial importance to reduce their microbending loss sensitivity. In order to do so, a bespoke packaging strategy has to be developed. The heuristic mechanical transfer function above suggests that this may take the form of increased fiber's glass diameter, increased coating thicknesses, and exploring the possibility using newer coatings optimized to filter out external perturbations at the relevant spatial frequencies [212]. The final research direction is that of producing HCFs with ultralow confinement loss at smaller core sizes. For example, for the same MTF, reducing the core size from 30 to 25 µm will reduce the microbending sensitivity by a factor of 6.

8. Other Extrinsic perturbations

In conventional fibers, the geometry of the waveguide usually possesses a cylindrical symmetry, greatly simplifying the analysis of geometric or material perturbations and the impact they may have on the loss and other optical properties [113, 165, 232]. In hollow-core fibers that possess this symmetry like Bragg fibers, theoretical tools have also been developed to study the impact of such perturbations [54, 168, 233].

However, because photonic bandgap fibers and antiresonant fibers incorporate a large number of material boundaries and do not possess the simple cylindrical symmetry, there exists a myriad of possibilities for geometric perturbations. Any study of their impact on the loss and other optical properties of the fibers is unlikely to be exhaustive. However, some of the most important ones can be studied, and some useful conclusions obtained.

One may make the distinction between two broad classes of geometrical perturbations. The first is a departure of the geometry under study from the ideal fiber which remains constant along the length of the fiber. These are for example, in the case of photonic bandgap fibers, a deformation or asymmetry of the core, non-uniform thickness of the core boundary, or a deviation of the cladding from the perfect idealized structure [74, 129]. In antiresonant fibers, this may mean an azimuthal misalignment of one or many of the tubes, a change in thickness along the circumference of the tube, non-uniform thickness among the cladding tubes etc. This class of perturbations in fibers can be thought of in a way as inherited from the macroscopic preform from which the fiber is made or resulting from some consistent reproducible effect in the fabrication process. Such perturbations or non-idealities affect the optical properties of the fibers by introducing cladding or surface modes which may interact strongly with the desired core modes, resulting as we have seen in an increase in leakage loss, often accompanied by a narrowing of the usable bandwidth of the fiber.

When such perturbations are longitudinally invariant, their impact can be directly studied with the help of numerical mode solvers and their properties can be compared to those of fibers with idealized geometries. In photonic bandgap fibers, core asymmetries and the impact they have via the introduction of surface modes has already been explored [74, 129]. In antiresonant fibers, the impact of a slightly broken symmetry of the fiber cross-section is often reported and more comprehensive studies of this type of perturbations are being undertaken [234]. The net effect is, as may be expected, an increase in leakage loss and narrowing of the usable bandwidth. For long lengths of fiber, these perturbations may vary along the fiber length, making it equivalent to spliced sections of fibers with different guidance properties. This,it was argued could lead for example to the loss of the photonic bandgap [69]. We believe however, that such perturbations and their impact will be best addressed via improvements in the fiber fabrication processes.

The second class of perturbations are small changes in the geometry, typically much smaller than the relevant waveguide dimensions or wavelength, that change randomly along the fiber length. These are random variations in the dimensions of the structure such as the fiber diameter or indeed the azimuthal position and diameter of each of the cladding tubes, an may result from random fluctuations of the key parameters of the fiber draw process. The complexity of the geometry means that the possibilities for such perturbations are innumerable. However, their general impact when present, will be to scatter light from one core-guided mode into other guided modes, cladding modes and radiation modes. This impact can be studied with coupled mode/coupled power theory as outlined above. If the perturbation of interest can be expressed as a perturbation operator $\Delta\hat{A}$, then Eq.(53) can be solved to find the impact of the perturbation on the propagation, with the power coupling coefficient given by Eq.(50), with a_{kl} given by Eq.(44) (the new $\Delta\hat{A}$ replaces the bend perturbation operator). In many cases however, the perturbation can not be described by an analytical perturbation operator $\Delta\hat{A}$, making the computation of the coupling coefficients rather difficult. However, the coupling coefficients can be calculated alternatively by first obtaining an induced volume current $\mathbf{J}$ as we did when analyzing roughness scattering. In this case, the amplitude coupling coefficient is simply given by:

$$a_{kl} = \int_0^L \iint_{A_\infty} \mathbf{E}_l^* \cdot \mathbf{J}_k dAdz \tag{59}$$

Where $\mathbf{J}_k$ is the induced current density when the mode $|\psi_k\rangle$ is propagating in the section of length L of fiber.

The first example we consider here is that of random diameter fluctuations along the fiber length. We assume a uniform scaling of waveguide dimensions, i.e, a map such that $x' \mapsto (1+\delta(z))x$ and $y' \mapsto (1+\delta(z))y$ where $\delta(z)$ is a small perturbation. Following the coupled-mode formalism described in [168, 235], we find after some algebra that to the first order in δ, this mapping corresponds to a perturbation operator $\Delta\hat{A}$ such that the amplitude coupling coefficient between modes is simply:

$$\begin{aligned} a_{kl} &= \left\langle \psi_l \middle| \Delta\hat{A} \middle| \psi_k \right\rangle \\ &= \frac{\omega}{c} \iint \begin{bmatrix} E_x \\ E_y \\ E_z \\ H_x \\ H_y \\ H_z \end{bmatrix}_l^\dagger \begin{pmatrix} & & x\varepsilon\delta'(z) & & & \\ & & y\varepsilon\delta'(z) & & & \\ x\varepsilon\delta'(z) & y\varepsilon\delta'(z) & -2\varepsilon\delta(z) & & & \\ & & & & & x\mu\delta'(z) \\ & & & & & y\mu\delta'(z) \\ & & & x\mu\delta'(z) & y\mu\delta'(z) & -2\mu\delta(z) \end{pmatrix} \begin{bmatrix} E_x \\ E_y \\ E_z \\ H_x \\ H_y \\ H_z \end{bmatrix}_k dA \end{aligned} \tag{60}$$

with $k \neq l$ and where $\delta'(z)$ represents a derivative. It is then easy to work out from here that the power coupling coefficient takes the form of:

$$h_{kl} = \left((\beta_k - \beta_l)^2 |I_1|^2 + 4|I_2|^2\right) \tilde{\Psi}(\beta_k - \beta_l) \tag{61}$$

with $\tilde{\Psi}$ the power spectral density of the diameter fluctuations $\delta(z)$ and I_1 and I_2 the integrals from Eq.(60) proportional to $\delta'(z)$ and $\delta(z)$, respectively. When the fiber is effectively single-mode, the added loss to the fundamental mode resulting from these fluctuations is $\sum_l h_{0l}$. The difficulty in obtaining the loss in this way is the large number of modes required. In Fig.31, we show the additional loss incurred by our example NANF (see Fig.7) for random diameter fluctuations using only the first 50 core and cladding modes found by the finite element solver. We assume here that the perturbations have a Gaussian power spectrum with a 1% mean-square and plot the loss as a function of the correlation length at 1550 nm. As may be expected, diameter fluctuations couple modes of the same azimuthal symmetry as can be appreciated from the coupling matrix. Since the longest coupling length between the fundamental mode and modes of the same symmetry is that between it and the LP_{02} mode and is of the order of ~460 µm, we see that diameter fluctuations with correlation lengths shorter than about ~1 mm can cause significant added loss. With the limited number of modes considered here, fluctuations with longer correlation lengths do not appear to cause noticeable loss penalty. Since rapid fluctuations of the diameter on the order of ~1 mm are typically not observed in practice, we believe that small diameter perturbations (1% or smaller) on realistic length scales, i.e., 1 m or longer, will have minimal impact on the fiber loss away from resonant wavelengths. Random ellipticity fluctuations can be treated in exactly the same way as above, and their effect as one may deduce is the introduction of birefringence as has been well documented elsewhere [113, 235].

In the next example, we consider that one of the big tubes in the NANF has a random thickness variation along the length of the fiber. In such a case, we can use the tools derived in Section 5.1

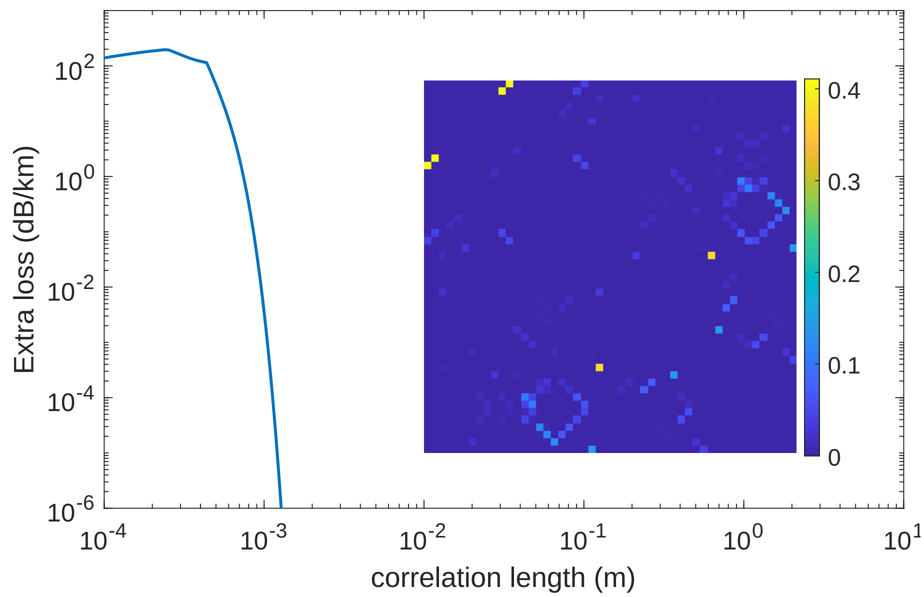

Fig. 31. Additional loss induced by diameter fluctuations in our example NANF. The assumed perturbation has a Gaussian power spectral density with an rms value of 1% and the loss is plotted as a function of the correlation length. The inset shows the calculated diameter fluctuation-induced mode coupling matrix for a correlation length of 500µm. For longer correlations than about 1 mm, the wavelength examined here, 1550 nm is unaffected by diameter fluctuations.

to directly compute the light scattered and lost to radiation. One distinction however is that in the case of thickness fluctuations, the perturbation on the outer and inner surfaces of the membrane are perfectly correlated. it follows therefore that the far-field scattered power distribution is:

$$\mathbf{S}_k(\vec{R}) = \frac{\omega^4 \varepsilon_0^2 \mu}{32\pi^2 R^2 c} L\tilde{\Psi}\left(\beta_k - k\cos\theta\right)\vec{r}\left|\sum_{m=1,2}\oint_{C_m}\vec{U}(s)\mathrm{e}^{jk(\rho'\sin\theta\cos\phi-\phi')}ds\right|^2 \tag{62}$$

where $m = 1$ or 2 for the inner and outer interface of the tube. In case many tubes are perturbed, we can calculate the far field scattered power for each tube as above and perform a summation over all of the perturbed tubes. We plot in Fig.32 the scattering loss that occurs for a 1% tube thickness fluctuation assumed to have a Gaussian power spectrum as a function of its correlation length. Shown in the inset is the far-field scattering pattern caused by such a perturbation. We see that for correlations lengths below 1 cm, significant added loss can occur. This added loss shows a peak of about 20 dB/km for a correlation length of ~1.1 cm but this then decreases sharply as the correlation length increases further. Although it is possible that short-scale thickness fluctuations exist in fibers, we believe long-range fluctuations are more likely and more compatible with the dynamics of fiber fabrication. Away from resonances, these are unlikely, as the results show, to cause significant added loss. Nevertheless, tools to confirm the magnitude of their potential contribution are of paramount importance in improving the fiber designs as well as the fabrication processes.

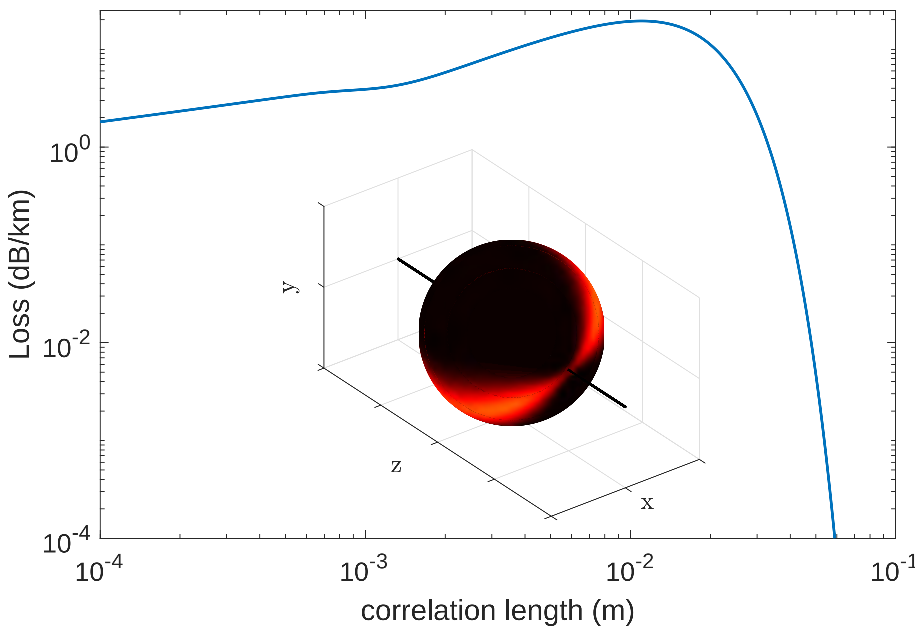

Fig. 32. Extra loss induced by thickness fluctuations of a single large tube in a NANF. The inset shows the far-field distribution of the power scattered by the tube with thickness fluctuations. The assumed perturbation is Gaussian with an rms of 1% membrane thickness (~5 nm). For correlation lengths of 3 cm or less, the fiber can incur significant added loss.

9. MacroBends

9.1. Overview of macrobending effects

In addition to the microscopic random perturbations examined in the previous sections, hollow-core fibers are often deployed in configurations that include some degree of sustained bending at a defined constant bend diameter. Bending of the fiber is of paramount importance for example in applications such as sensing where deploying the fiber in a small coiled topology is essential [33]. By introducing a bend to the fibers, the straightness of the propagation path no longer holds, and the modes experience a modification of their field profiles and propagation constants. What ensues is additional loss to radiation. In extreme cases of bend, for example at small bend diameters, the modes of the fiber may cease to be guided.

In general, the induced bend loss can be associated with two distinct mechanisms, namely, transition loss and curvature bend loss [236, 237]. The former is the result of power transfer from modes in the straight part of the fiber to radiation modes in the constant-curvature section of the fiber. This transition loss typically accounts for a negligible part of a bent fiber since the transition section is often very short. On the other hand, significant loss can occur in the constant curvature section if it is sustained over a long distance because lossy cladding modes introduced by the bend can couple with the core guided modes. Such loss inevitably accounts for the majority of the total bend loss.

A quantitative assessment of bending effects in optical waveguides is generally achieved by mapping the curved propagation path of the light in the bent waveguide onto a straight one using conformal optics [236]. In this method, the bent path is conformally mapped to a straight one, but the impact of the curvature of the waveguide is mapped onto its material property, specifically

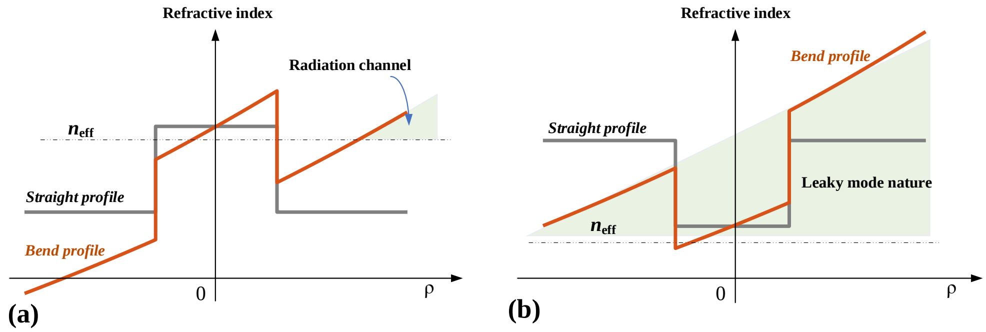

Fig. 33. Equivalent refractive index distribution in bent waveguides obtained by conformal transtransformation. The bent waveguide is equivalent to a straight one with a tilted refractive index profile, with the index increasing from the inside to the outsize of the bend. In solid-core step-index fibers (a), the bend introduces new lossy cladding modes to which the core mode can couple. Similarly, in a hollow-core fiber (b), the leakage is exacerbated by the introduction of higher effective index lossy cladding modes.

the refractive index distribution is [236, 238, 239] modified as:

$$n_b = n_s e^{\frac{x}{R_b}} \tag{63}$$

where n_b is the refractive index distribution of the bent waveguide, n_s that of the straight fiber, R_b the bend radius and it is assumed the bend is along the direction of the $x-$axis. The impact of the bend can then be studied with the same analytical and numerical tools. We note that this transformation is only an approximation. A more rigorous treatment accounts for the shifting of the material boundaries, an effect which is non-negligible at very small bend radii (where indeed the approximation breaks down completely) and in fibers with high index contrast between their constituent materials such as hollow-core fibers. Such a rigorous treatment is found for example in the method of transformation optics [240, 241]. Nevertheless, for the most relevant and practical deployment scenarios, the approximation above provides adequate accuracy.

Figure 33 illustrates the effect of the simple conformal transformation on the index profile of a standard solid core step-index fiber (SIF) and a cylindrical hole in glass (as studied by Marcatili [115]). In the SIF, the tilted index profile introduced by the bend provides the prospect of the core guided mode being phase matched to a cladding mode, thereby resulting in loss. This observation has informed the main design approach for low bend loss solid-core fibers, which is via the introduction of low-index trenches in the cladding to keep the index of cladding modes low when the fiber is bent [242, 243]. In the HCFs (an example in Fig. 33 (b)), even when straight, the modes suffer from leakage loss due to the cladding being capable of supporting phase-matched radiation modes. Once the bend modifies the index profile of the waveguide, the leakage is enhanced further.

For further insight into a quantitative analysis of the impact of macrobends, we note that a bend sustained over a long length of fiber can be treated as the limit of a waveguide with a very large number of small tilts [153]. We have seen in Section 7 that the effect of a small tilt is to couple light from an incident mode into other guided modes and radiation. One may therefore consider that for a bend sustained over long distance, it is possible to express the eigenmodes of the bent waveguide as a linear expansion of the modes of the straight fiber. For bend radii much larger than the fiber diameter, the modes are only slightly perturbed. In such a case, a second order correction to the propagation constant (since the first order correction vanishes under the bend perturbation) is [54]:

$$\Delta\beta_k = \sum_{l\neq k} \frac{\left|\left\langle \psi_l \middle| \Delta\hat{A} \middle| \psi_k \right\rangle\right|^2}{\beta_k - \beta_l} \tag{64}$$

where $\left\langle \psi_l \middle| \Delta\hat{A} \middle| \psi_k \right\rangle$ is given by Eq.(45) and the summation extends over all core, cladding and radiation modes. From this expression, if the modes are associated with a loss α_k in the straight fiber in the form of a small imaginary part to the propagation constant, one may extract the loss due to bend from Eq.(64) as [54, 244]:

$$\alpha_{bend,k} = \sum_{l\neq k} \frac{\left|\left\langle \psi_l \middle| \Delta\hat{A} \middle| \psi_k \right\rangle\right|^2}{(\Re(\beta_k - \beta_l))^2} (\alpha_l - \alpha_k) \tag{65}$$

This expression, phenomenologically similar to Eq. (13), provides powerful insight. First, since from Eq.(45), $\left\langle \psi_l \middle| \Delta\hat{A} \middle| \psi_k \right\rangle$ is proportional to $1/R_b$. It follows from this that the bend loss scales as $1/R_b^2$. This inverse square law dependence on bend radius for large bend diameters has been confirmed in [244]. This scalling does not hold at small bend radii because such tight bends cause strong mode mixing and introduce new cladding modes whose propagation constants depend on R_b. Skorobodaity et al. show that in this regime, the bend loss scale instead as $1/R_b$ [244]. Secondly, if the bend modifies cladding modes in such a way that their phase index matches that of the core mode of interest, this can result in extremely high loss for that core mode (i.e. $\alpha_{bend,k} \to \infty$ when $\Re(\beta_k - \beta_l) \to 0$) . This insight is useful to determine for example a critical bend radius for which the bend loss becomes prohibitively high for a desired mode. Such a bend radius is solved for by considering that under bend, the cladding tube mode reaches an effective index equal to that of the core mode, see for example [245–247]. Interestingly, if the cladding modes to which the core guided modes couple under the bend are discrete, it is possible that the bend loss as a function of bend radius shows discrete resonance peaks separated by relatively low loss regions, as the discrete cladding modes are phased matched with the core modes at discrete bend radii [248, 249]. On an additional practical level, once a design for the cladding is chosen, it is possible to choose an adequate bend diameter that allows to strip unwanted modes, should they be excited at launch into the fiber [250].

We note that in antiresonant fibers, a simple scaling of the bend loss with the core size and wavelength is not easily extracted from Eq.(65). This is because increasing the core size comes with a modification of the cladding arrangement and with it, the lossy modes it may support which are further modified by bending. This situation arises because the dependence of the β_l, and α_l on core size, cladding design and wavelength is not analytically tractable at all bend radii. Such scaling, in most cases may therefore only be obtained empirically.

9.2. Macrobend loss in hollow-core fibers

To examine the loss penalty incurred by PBGFs and NANFs when they are bent, we apply the conformal transformation technique mentioned above where the bend is mapped onto a modification of the constitutive tensors of the material media of the fiber [236]. After applying such a transformation, we plot in Fig. 34 the confinement loss calculated when the PBGF and NANF of Fig. 7 are wound on a standard shipping spool with ~15.8 cm diameter. At this bend diameter, the PBGF suffers virtually no noticeable additional confinement loss. The resilience of PBGFs to bends is well known and documented, and our simulations at the smaller bend radius of 1 cm still show little additional loss near the centre of the bandgap, as also confirmed in experiments [251, 252]. This comes as no surprise since the same principles that endow them with low leakage loss are at play in keeping their bend loss low. Therefore, we focus the remainder of this section on antiresonant fibers, with the NANF of Fig.7 as an illustrative example.

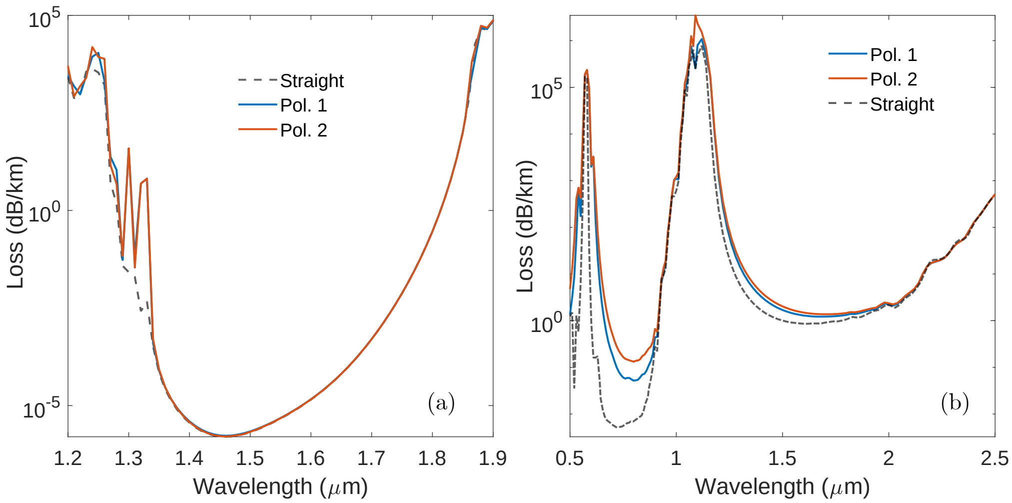

Fig. 34. Bend-induced additional confinement loss on a standard shipping bobbin (158 mm diameter) as a function of wavelength for the PBGF (a) and NANF (b). (a) The bent PBGF incurs virtually no additional confinement loss as the dashed curve calculated for the straight fiber overlaps with the confinement loss for both polarization of the fundamental mode under bending. (b) In the NANF, bending induces noticeable added confinement loss and also a small amount of birefringence and polarization-dependent loss (PDL). The bend loss calculated here is for the bend plane bisecting two sets of tubes.

For this NANF, there is a noticeable increase in the confinement loss as a result of the bend, which as we expect from our analysis of microbending is higher at shorter wavelengths. In the specific example here, the leakage loss increases from 1 dB/km when straight to an average of ~1.4 dB/km when wound on the shipping spool. We emphasize that this is inextricably linked to our choice in the size of the nested elements. Different bend performance can be expected when the size of these elements is modified. Bending also introduces a small birefringence and a noticeable amount of polarization-dependent loss, see Fig.35 [200,253]. This can be conceptually understood from the picture of leakage loss as the result of partial reflection (see Section 2.1). The bend imposes an additional two-fold symmetry about the bend plane and as a result, the mode polarized in the plane of the bend has its polarization vector substantially more orthogonal to the *core boundary* (thus effectively resembling a $p-$ polarized or TM wave) than the one polarized orthogonal to the bend plane ($s-$wave). The former suffers higher loss as expected, since it is less effectively reflected by the cladding membranes. We emphasize that bending loss in the NANF depends on its structural parameters and design, notably the core diameter. In Fig.35, we plot the bend loss as a function of core diameter for a fixed bend diameter of 158 mm. In scaling the core size, the membrane thickness, the ratio between nested tube diameter and core size, and ratio between gap and core diameter are all kept constant. We can observe interestingly that the pure bend loss reaches a minimum around a core diameter of 35 µm (see inset of Fig.35). This, we expect, would change for a different bend diameter or a different cladding design. Our observations therefore do not apply to all NANF structures, but further illustrate the complexity of how the bend loss scales with core size and wavelength. An in-depth study of macrobending effects in antiresonant fibers and NANFs in particular will be presented elsewhere [254].

One additionally expects *a priori* that the six-fold (or generally N-fold) symmetry of the structure results in a dependence of bend loss on the direction of the bend plane. Figure 36(a) shows the bend loss for both polarizations of the fundamental mode for a bend radius of 5 cm as

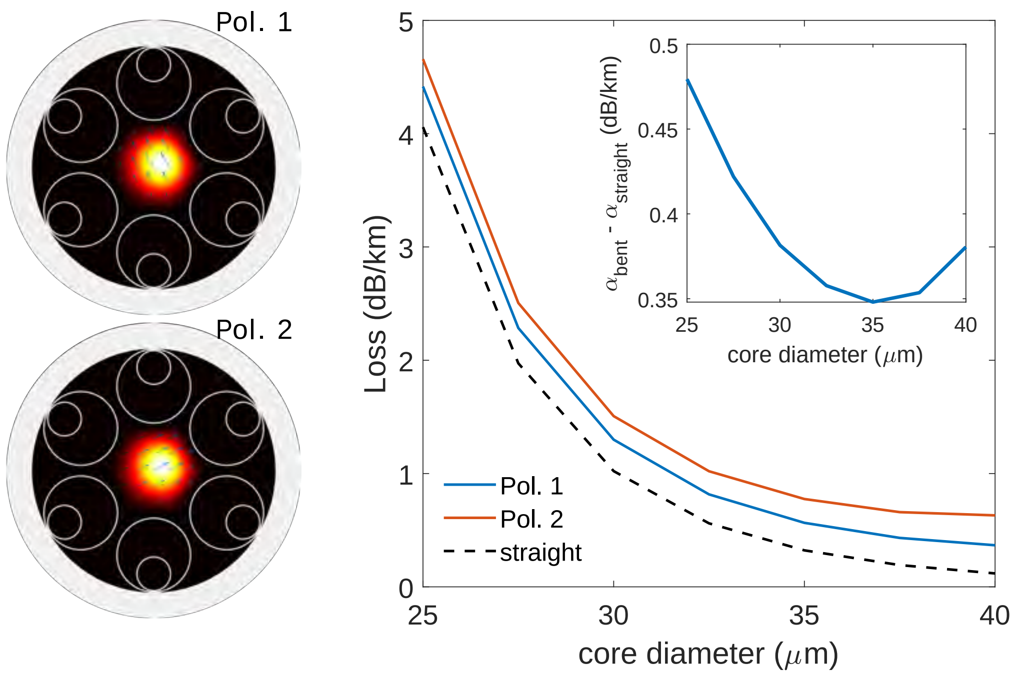

Fig. 35. Bend loss in NANFs on a standard shipping bobbin (158 mm diameter) as a function the core diameter. The inset shows the pure bend loss, i.e., the difference between the leakage loss when the fiber is bent (average between the two polarizations) and when it is straight. The bend plane is perpendicular to the tubes. In this special case, the added loss reaches a minimum around a core diameter of 35μm.

a function of the bend plane azimuth and confirms that this is indeed the case. The total loss as a result of the bend is well expressed by $\alpha_0 + \alpha_1 \cos N\theta$ where theta is the angle between the bend plane and the $x-$axis. Unsurprisingly, the loss of the in-plane polarized mode (pol. 2) is highest when the bend plane is aligned with the tube (bend azimuth of 0°) and lowest when it is aligned with the gap between tubes (bend azimuth of 30°), and vice-versa for the orthogonal polarization.

In Fig.36 (b), we plot the loss for both polarizations when the bend plane is aligned with the tube as a function of bend radius. We can see that for moderate values of the bend radius, i.e ≥ 5 cm, the approximate $1/R_b^2$ scaling holds reasonably well. However, the loss increases sharply if the bend radius is reduced further, in this specific case, below a bend radius of 4 cm which may thus be defined as a critical bend radius for the specific NANF considered here [245].

Clearly, macrobending can be a considerable contributor to loss in hollow-core antiresonant fibers and should be given due attention when designing fibers for applications where the deployment effectively involves bends over long distances. Macrobending loss presents a richer picture in these fibers, it is inextricably linked with the design of the fiber, its symmetry, the bend orientation as well as the bend diameter. But it lends itself to some degree of control and significant reduction in bend loss is possible through engineering the fiber structure. Our analysis in the previous section and in Section 2.2 shows that the key is to ensure that under bend, the cladding structure does not support modes that have a strong overlap and are phase-matched to the core mode of interest. In practice, this may be accomplished through different controlling the size of the hollow regions within the cladding. For example, by adding the nested tube to the simple tubular fiber design (see Fig.9), both the straight leakage loss and bend loss are greatly reduced [101, 102]. Using a large number of smaller cladding tubes in a tubular fiber also reduces

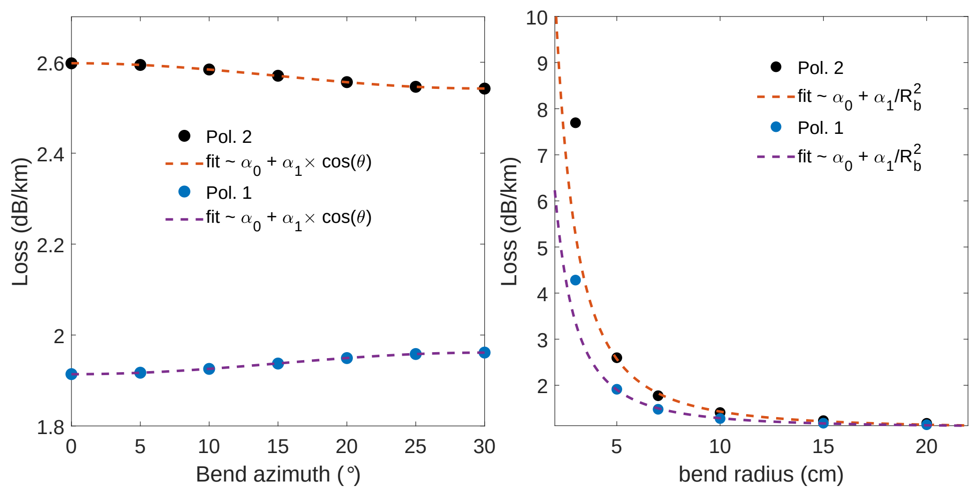

Fig. 36. Bend loss in the NANF as a function of bend plane azimuth (a) and bend radius (b). The bend loss in (a) is calculated at a bend radius of 5 cm. 0° corresponds to the bend plane aligned with the tube and 30° corresponds to when it is aligned with the gap between tubes. In (b) the bend plane intersects the tube and for $R_b \geq 5$ cm, the loss follows R_b^{-2} as expected.

the bend loss. There are trade-offs in addressing bend loss via these design techniques. For example, using many smaller tubes results in higher straight loss due to the proximity of the glass jacket to the core, whilst partitioning the hollow regions into smaller areas may reduce the loss of higher order modes, making effective single mode operation more difficult. Designs like the double-NANF (DNANF) with 5 tubes overcome this dilemma by simultaneously providing high intermodal differential loss and low bend loss [45].

Part III

Designing low-loss hollow-core fibers

10. Loss analysis in state of the art fibers

In this section we use the tools derived in the previous sections to describe the loss in an example state-of-the-art 6-tube NANF reported by our team [109]. This example is simply illustrative as the analysis can be (and routinely is) performed on any fiber provided its cross-section can be captured accurately from scanning electron microscope images into the finite element solver.

The fabricated NANF sample had an experimentally measured minimum loss of 0.28dB/km. The NANF geometry or similar concepts has been the subject of intense research efforts over the past five years, resulting in dramatic and sustained loss reduction. We have since reduced the loss for the fundamental mode whilst increasing higher order mode loss in the NANFs first to 0.22 dB/km by adopting a five tube geometry [95] and later to 0.174 dB/km by introducing an additional nested tube [45]. These fibers can be modelled and analysed in the exact same way. The fiber we analyze here, as can be seen in Fig. 37, consists of six pairs of nested silica capillaries arranged around a central hollow core. From the SEM image of the cross-section, we measured an average thickness of 0.5μm for the outer tubes, with inner tubes approximately 6% thicker. The core size diameter was measured to be 34.5μm and the average gap between the

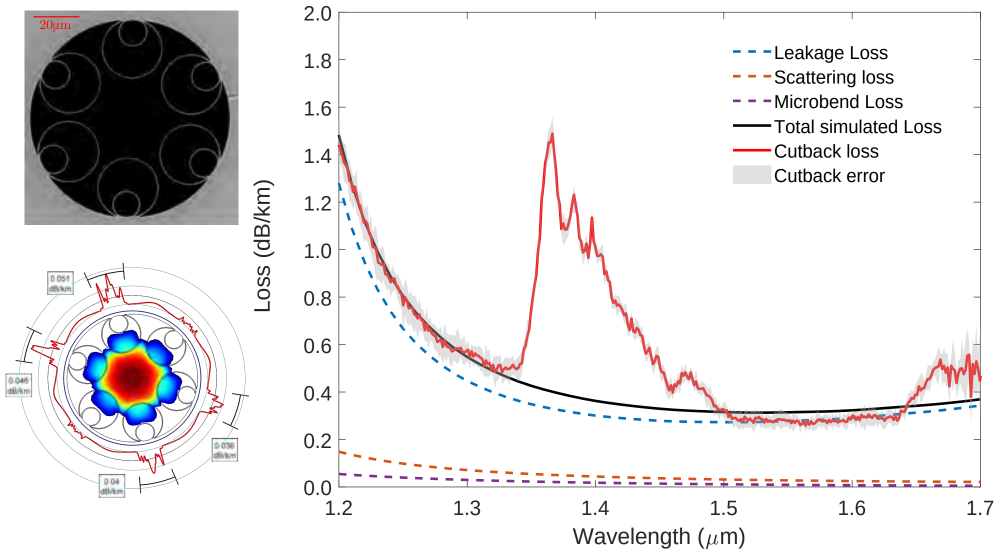

Fig. 37. Loss analysis in a state-of-the-art 6-tube NANF fiber [109]. The experimental curve (solid red) was measured via cutback from 1700 m to 500 m. This was repeated several times to give the measurement uncertainty (grey area).

larger tubes was 4.4 µm. We reconstructed the permittivity profile of the fiber from the SEM images by accurately capturing the coordinates of the tubes and for simplicity, assumed that they were of circular shape and even thickness all around.

Figure 37 shows the modelled intrinsic loss contributions in the fiber along with the experimentally measured attenuation. We first consider the confinement loss which can be seen to account for nearly all of the loss across the C and L bands. Indeed, at 1550 nm, the fundamental mode has a leakage loss of leakage loss of 0.27 dB/km, accounting for the near totality of the measured average value of 0.28 dB/km. A closer analysis through examining the azimuthally resolved radial Poynting vector shows that this confinement loss is dominated by power flowing radially outside of the core of the fiber through the tubes (note how most of the light leaks through tubes which are oriented orthogonal to the polarization vector of the fundamental mode). Interestingly, our simulations showed that the LP_{11}-like mode group suffered leakage loss in the 6-10 dB/km range, whilst other higher order modes incurred > 1 dB/m loss, making the fiber effectively 2-moded. Next, we calculated the scattering loss using Eq.28 and found it to amount to about 0.027 dB/km. As noted in [109], this is much lower than the ~0.1dB/km that would be predicted form the empirical scaling of the normalized interface field intensity (Eqs.(41) and Using the single mode approximation of Eq. (55), we estimated an additional microbending loss contribution of 0.02 dB/km. For the microbend power spectral density, we chose a spectrum of the form A/κ^{2p} with model values $A = 5 \times 10^5$ and $p = 2$ which provided consistent agreement across many experimental fibers. This gives an estimated total loss for the fundamental mode at 1550 nm of ~0.32dB/km (the steady-sate loss plotted in Fig.37 is ~0.3dB/km). Within measurement error, this is in very good agreement with experimental data, considering that such sources of uncertainty exist both in the experimental measurement and the accuracy with which the fiber profile is reconstructed from the SEM images.

It is noteworthy that this agreement is consistent throughout the transmission window of the fiber, except for the ~1350-1450 nm water vapor and the >1650 nm which are instrument artifacts at the long wavelength edge of the optical spectrum analyzer. The level of agreement between the theoretical contributions to loss and the measured value are also a testimony to the already achievable levels of uniformity in the fiber structure along its length, showing particularly that if present, some of the perturbations analyzed in Section 8 are on length scales that do not significantly alter the loss of the fiber. Therefore, for antiresonant fibers, it is possible to make reliable analysis and predictions on possible fiber performance by relying solely on the three mechanisms of leakage, scattering and microbending.

11. Scaling rules and design optimization

In this section we summarize our analysis and use the key scaling rules we have established to inform a view on the potential lowest achievable loss in hollow-core fibers and the spectral wavelength at which such lowest loss may be obtained.

As we have seen, bar for some model hollow-core fiber types [117], an analytical expression for the loss at all wavelengths in hollow-core fibers remains almost unattainable. However, an empirical prediction for the minima of the key loss contributions is possible and that is what we attempt here. Let us consider that for a given operating wavelength λ_0, we have optimized the design of the cladding to minimize the leakage loss through choice of pitch, air-filling fraction, glass node size, core wall thickness in PBGFs or alternatively by choosing the membrane thickness, the size, nesting configuration and arrangement of cladding tubes in antiresonant fibers (we will consider NANFs for simplicity). For the purpose of the discussion here, we will assume that such a cladding design makes the fiber effectively single-moded. The key loss mechanisms we consider in optimizing the designs will be limited to leakage, surface scattering and microbending. For the purpose of predicting ultimate loss performance, we thus neglect the macrobending loss contribution which is small when the fibers are wound on large bobbins (see Section 9 or deployed in cables, but which must be considered in applications requiring compact coils. We also do not consider other perturbations,thus assuming that they can be removed by technological improvements or if present, are on length scales that don't affect the propagagtion of the fundamental mode (see section8). Table 1 summarizes the scaling rules for these key loss contributions.

A very important question that arises then is to determine what core diameter provides the lowest possible loss at λ_0. Without considering microbending contributions to loss, both scattering and leakage decrease monotonically with core size and thus loss can be made arbitrarily low by choosing ever larger core sizes. There are, however, practical limitations on the fiber's dimensions and flexibility often imposed by the intended application and also on the choice of coating materials available. With such limitations, the microbending contribution cannot be neglected at all core diameters. Since it increases rapidly with core size, there exists therefore an optimum core size for which the total loss is lowest. Without loss of generality, we will consider here the example of a 6-tube NANF for which a choice of membrane thickness t and cladding tube size and gap between them gives a minimum confinement loss of 0.2 dB/km at 1550 nm in a 35 μm core diameter fiber. The contribution from scattering loss in such a fiber is 0.03dB/km and the fiber is packaged in a way that the microbending leads to an additional 0.02 dB/km for a total loss of 0.25dB/km. As shown in Fig.14, if such a NANF is scaled so that the gap to core radius ratio remains constant at 1/5, the leakage loss decreases with the core as $1/a^{7.5}$. The microbending loss contribution scales as in Eq. (56) with a p-coefficient of $p = 2$ used throughout the paper. In this case, the total loss as a function of core diameter is plotted in Fig.38. Confinement loss accounts for nearly all of the loss for core diameters smaller than 35μm and microbending dominates for core sizes larger than ~40μm. With these parameters, which are not far from those already achieved (see Section10 and [109]), we see that a loss as low as 0.17dB/km can be achieved with a core diameter around 39μm. However, fabricating such large core fibers whilst maintaining control over other cladding parameters may prove challenging in practice and care must be taken to ensure that the fiber remains highly uniform along its length and that its packaging guarantees low levels of microbending loss. Note that for the prediction

Loss mechanism	Scaling	Description
Confinement loss	$\frac{\lambda^{l+2}}{a^{l+3}}$	This scaling applies to antiresonant fibers, l is the number of antiresonant layers, λ the wavelength and a the core radius. The exact powers may depend on other geometry parameters such as gap size and size of nested elements. Refer to section 2
Material loss suppression factor	$\frac{\lambda^2 t}{a^3}$	Fraction by which either absorption or scattering loss in the glass material are suppressed. For antiresonant fibers, t is the cladding membrane thickness
Surface scattering loss: rigidly scaled fibers	$\frac{1}{a^3}$	For a given fiber design scaled rigidly to operate at different wavelengths, the minimum scattering loss scales only with the core size. See section 5.4
Surface scattering loss approximation	$\eta F \left(\frac{\lambda}{\lambda_0}\right)^{2.5}$	Approximation of the rigorous scattering loss for a given fiber across its transmission windows. See section 5.5.
Surface roughness-induced intermodal coupling coefficient	$\frac{\lambda^3}{a^6}$	Roughness induced power coupling rate between core-guided modes. See section 5.6 and also ref [155].
Higher order mode surface scattering loss or absorption from glass	$\frac{\alpha_{mn}}{\alpha_0} \propto u_{nm}^2$	Ratio between the surface scattering loss or the material loss of the LP_{mn} mode and that of the fundamental mode. u_{nm} is the m-th zero of the Bessel function $J_{n-1}(x)$. See section 6
Microbending loss (single mode approximation)	$\frac{a^{2+4p}}{\lambda^{2+2p}}$	It is assumed the microbend power spectrum can be expressed as A/κ^{2p}. See section 7
Macrobend loss	$\frac{1}{R_b^2}$	The scaling is valid when the bend radius R_b is greater than a critical bend radius.

Table 1. Summary of scaling rules for key loss contributions in hollow-core fibers.

shown in Fig.38, we assume that the outer diameter and fiber packaging remains the same as the core size is changed.

Repeating the process above with a photonic bandgap fiber for which we assume negligible confinement loss and a surface scattering limited attenuation of 1dB/km for a 21μm core diameter, we find, interestingly, that the loss minimum predicted for a core diameter of 41μm is 0.19 dB/km. Note that this larger core size effectively demands removing a 61 unit cells to make the core defect which gives rise to significant challenges in fabrication and would in effect render void our assumption of single mode guidance. We do not foresee that such a fiber could be successfully fabricated.

A second and very important question is that of the ultimate low loss achievable in hollow-core fibers and at which wavelength this may be achieved. For practically achievable photonic bandgap fiber geometries, i.e., with 19c core defects, the loss is dominated by surface roughness scattering

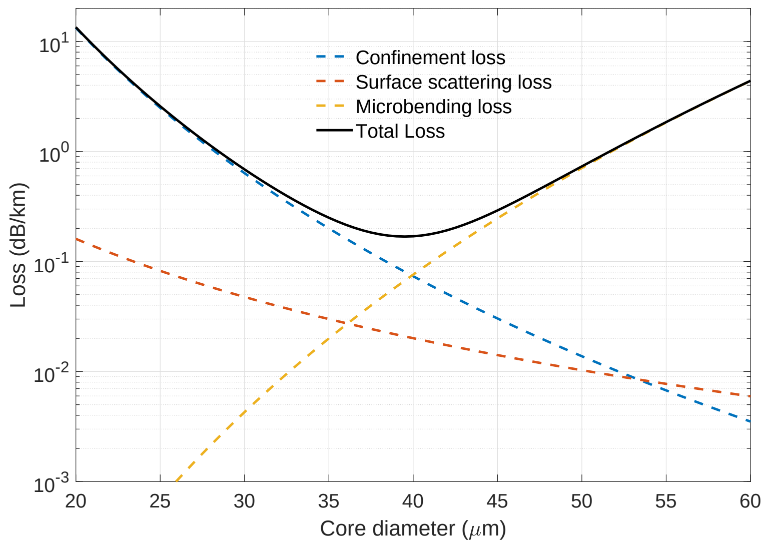

Fig. 38. Optimizing the core diameter for a NANF with a 6T geometry to achieve lowest possible loss near 1550 nm.

and multiphonon absorption at infrared wavelengths. When microbending is neglected, our conclusions are similar to those in [49], where 0.2 dB/km near 2µm is predicted.

For antiresonant fibers, there is great flexibility in that the membrane thickness which controls the guidance can be adjusted separately of the core diameter with which key loss mechanisms scale. In such a scenario, without the loss contribution from microbending or practical constraints on fiber size and packaging, there is no optimization to be done as the natural choice at any wavelength will be the largest core size possible. Were this to be the case, arbitrarily low loss could be achieved at any wavelength. However low it may be though, the microbending loss contribution must be taken into account and practical limitations on the size of the fiber and its core as well as deployment conditions play a role too. As a result, for each operating wavelength, we can carry out the same optimization as in Fig.38 to find the core size which provides the lowest loss possible at a given wavelength. Without loss of generality, we will assume in the first instance that no improvement in microbending loss is possible beyond what is currently achievable and that all fibers will be restricted to the same outer diameter. Regardless of the wavelength of operation, we thus assume that the fibers are drawn to the same outer diameter and use the same coatings and packaging, thereby making them subject to the same microbending perturbation power spectral density. Taking the 6-tube NANF as an example, we show in Fig. 39 the optimized loss as a function of wavelength from the visible up to 3 µm. For each wavelength, we optimize the core diameter of the fiber so that the combination of contributions from surface scattering, leakage, microbending and bulk scattering or absorption is minimized. In scaling the leakage loss, we have assumed that the gap between the large tubes of the fibers are kept at a constant fraction of the core radius ($g = a/5$). For longer wavelengths, we also include the absorption from the glass. For simplicity, IR vibrational absorption as $\alpha_{IR} = 6 \times 10^{11} \exp\left(-48/\lambda[\mu m]\right)$ [146] (this provides an adequate approximation to the data available from Heraeus up to ~3µm [156]). The Rayleigh scattering in the glass may be accounted for also, for example by taking the Rayleigh scattering coefficient of pure silica as $\alpha_R = 0.11 \times (1.55/\lambda[\mu m])^4$ [43, 146], though we found it plays a negligible role.

Our results shown in Fig.39 paint a very interesting picture. For this six tube NANF geometry, we see that at wavelengths shorter than about 1µm, surface scattering is the biggest contributor

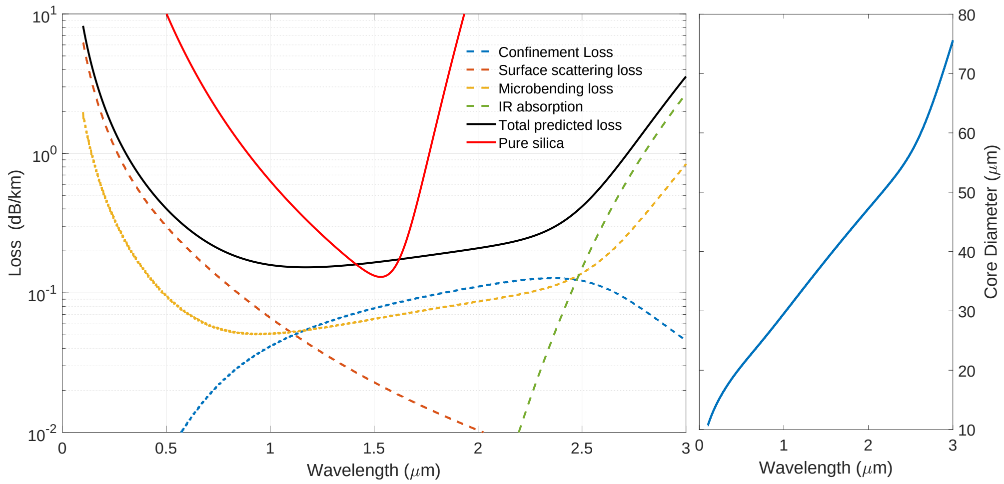

Fig. 39. Predicted achievable loss values in 6-tube NANFs geometries operating from the Uv to 3µm. For each wavelength, we optimize the core size to obtain the minimum total loss made of contributions from confinement loss, surface scattering loss, microbending loss and at wavelengths beyong 2µm, IR absorption from the glass. For all wavelengths, microbending is calculated by assuming the same outer diameter and polymer coatings. Surface scattering dominates at wavelengths below ~1µm and absorption beyond about 2.5µm. The red curve shows the ultimate loss achievable in pure silica core fibers across the same wavelength range. With the imposed limitations, the 6-tube NANF outperforms pure silica at all wavelengths, except for a narrow spectral region around the C-band.

to loss. Below 0.5µm, the confinement loss is very low. The implication is that more complex designs which primarily further reduce the leakage loss at similar core sizes are not necessary for fibers operating in this region. Thus in principle, the simpler tubular designs can be optimized to provide the lowest loss possible in this spectral region (see for example [104]. Similarly, at wavelengths beyond about 2.5µm, the loss is dominated by IR absorption. Although the confinement loss is relatively high for the somewhat small core diameters of the 6-tube NANF, this also means that the simpler tubular design can be optimized to provide very low loss, for example by increasing the number of tubes, the core size and the fiber diameter to lower the microbend contribution. Between 1 and 2.5µm, leakage and microbending are the biggest loss contributors. This is the spectral region where significant loss reduction is possible via tweaking the cladding design to allow further reduction of leakage and microbending loss. For the six-tube NANF geometry adopted here, the loss minimum of 0.15dB/km is obtained near 1.2µm (we emphasize that this is specific to the geometry we are studying. The number of cladding tubes, gap between tubes, size of nested element can all be changed to further reduce the loss). We also plot the ultimate loss of pure silica fibers for comparison in red. As can be seen, the lowest loss achievable with experimentally demonstrated 6-tube NANF designs is lower than that of pure silica across all wavelength regions, except in the C-band where it is higher by a few hundredths of dB/km. We reiterate that this is but a limitation of the specific six-tube NANF design explored here for illustrative purposes only. By providing lower leakage loss, alternative structures such as the 5-tube NANF (3 to 4x lower) or our recently reported 5-tube DNANF which we examine next (10 to 20x lower), simply outperform pure silica fibers at all wavelengths. This means that with their other attractive properties, hollow-core antiresonant fibers offer strong competition to traditional silica fibers and may well replace them in the long run.

12. Outlook and future prospects

We now take a look at what the future might hold for hollow-core fiber technology. The continuing rapid pace of development and improvement in performance means that the predictions we make here may well be fulfilled or indeed obsolete by the time this manuscript is published. We base our projections here not on as yet unrealized and promising fiber designs, but on the DNANF structure we recently reported [45]. As the dynamic research field continues to advance, we believe that significant loss reduction is possible and we will soon see reports of ever more transparent fibers with unprecedented low loss values. To illustrate why, we note that as shown in [45], for a similar core size, the DNANF can provide more than 10x lower leakage loss compared to a 5-tube NANF. We will make projections here with the somewhat conservative value of leakage loss of 0.02dB/km in a 35µm core diameter DNANF. The surface scattering remains the same for the same core size (0.03 dB/km), as does the microbending contribution (0.02dB/km) if the fiber is drawn to the same outer diameter. We will assume that fiber packaging can be improved to give an overall 2x reduction on the microbending loss contribution to 0.01 dB/km. Already, this means a loss of only 0.06dB/km, more than 2x lower than the lowest loss single mode fiber [42, 255].

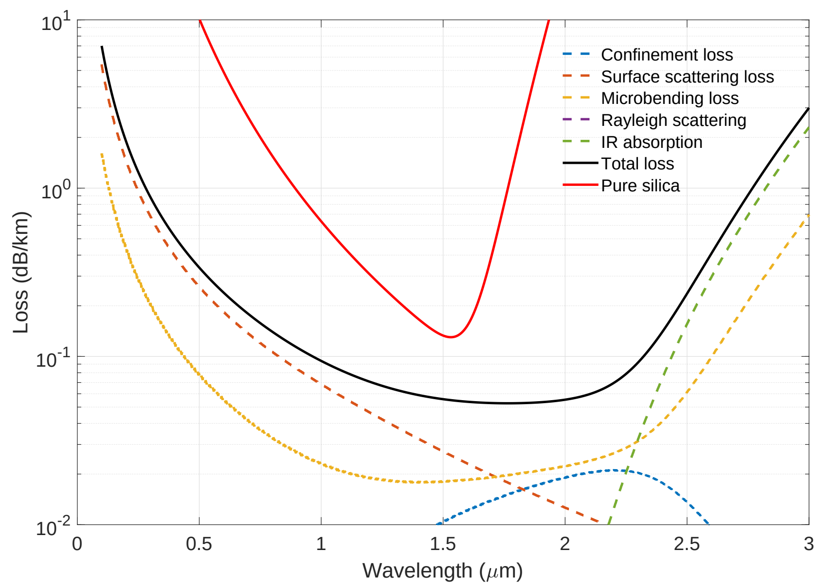

Fig. 40. Predicted achievable loss in DNANF fibers as a function of wavelength. We assume a 2x reduction in current microbending loss levels. As can be seen, the DNANF would outperform pure silica at all wavelengths from visible to mid-IR, with a remarkable minimum loss of 0.053 dB/km at 1.75µm and only 0.055dB/km at 1.55µm.

With this assumption, we show in Fig. 40 our predictions loss values that can be achieved for such a DNANF and again for reference, the loss limit of pure silica core fibers across the same spectral range . As may be expected, the DNANF can be tailored to have lower loss than the most transparent materials known to date at all wavelengths from the UV to the mid-IR. We predict, with our self imposed limitations on microbending, a remarkable minimum loss of 0.053dB/km near 1.75µm. In contrast to the 6 -tube NANF, microbending is the biggest contributor to loss in this low-loss spectral region (1.7 - 2.2 µm) and scattering or absorption dominate at either side of it. To further illustrate that these predictions are conservative and cautious, we plot in Fig.41 the loss of a DNANF with an optimized core diameter of 35µm and membrane thickness of 408 nm.

For this DNANF structure, the minimum confinement loss near 1.25µm is only ~10^{-4} dB/km. Surface roughness and microbending dominate the total loss. Remarkably, the fiber achieves a loss below 0.1 dB/km from 1320 nm to 2µm, 0.055 dB/km at 1550 nm and a minimum of 0.043 dB/km at 1780 nm.

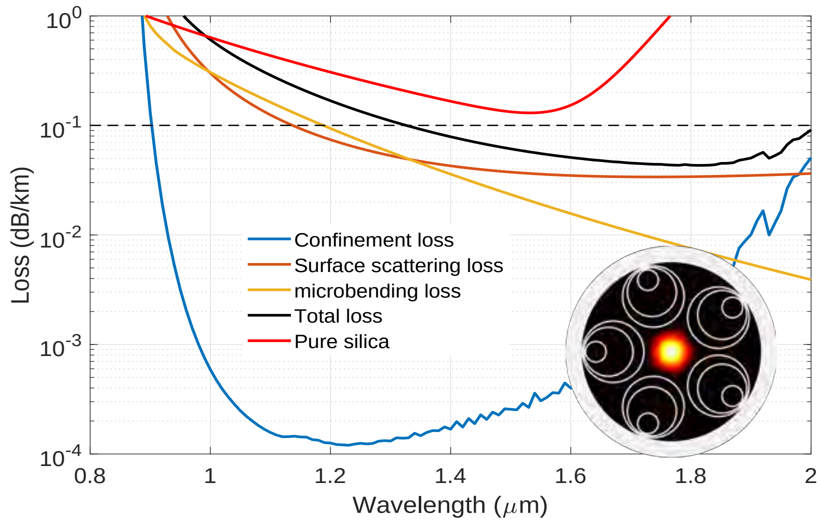

Fig. 41. Simulated attenuation of a DNANF with optimum core size operating near 1550nm. The fiber has a core diameter $2a = 35\mu m$, uses 5 sets of double nested tubes, a membrane thickness of 408 nm and a gap between the tubes $a/5$. The double nested structure results in a significant reduction in confinement loss to a minimum of only ~10^{-4} dB/km and the loss is thus dominated by surface roughness scattering and microbending. The fiber achieves a total loss <0.1 dB/km between 1320nm and 2µm

Could loss be reduced beyond these predictions for the DNANF? It is possible that some other, as of yet undiscovered antiresonant fiber designs may offer leakage loss levels rivalling that of photonic bandgap fibers, but that would leave surface scattering, absorption and microbending. If the latter is reduced by a further factor of 10, as one can see from Fig. 40, with only surface scattering (dashed orange curve) and infrared absorption (dashed green curve) contributing to loss , the minimum loss would be predicted where they cross, near 2.2 µm, and in this speculative scenario, would be of the order of ~0.02dB/km.

Such fibers would effectively usher in vacuum-like optical guidance properties in flexible waveguides and over long distances, revolutionizing telecoms [196] and transforming many fields in which optical fibers have traditionally been used such as sensing [200] or laser power delivery [256]. It is our belief that in the near future, perhaps even by the time this work is published, the first <0.1 dB/km fiber will be reported and it will take the form of a hollow-core antiresonant optical fiber.

13. Concluding Remarks

Hollow-core optical fibers represent arguably one of the most exciting developments in optical fiber technology in the past four decades. From the early excitement following the introduction of the hollow-core photonic bandgap fiber structure in 1999, to the somewhat disappointing realization that surface scattering may yet limit the loss in such fibers to 5 or 6 times higher than single mode fibers in the C-band and back again to the reignition of that excitement with antiresonant structures, the field has developed tremendously and now sits on the cusp of transforming all application areas in which light guidance in its purest form over long distances is needed, whilst uniquely enabling many new ones.

A fundamental understanding of the basic mechanisms that contribute to attenuation in such fibers is of paramount importance in enabling the realization of fibers with unprecedented low loss levels. In this paper, we have presented a theoretical analysis of these loss mechanisms based on the best current understanding. Our theoretical analysis accounts for intrinsic loss mechanisms such as leakage loss which uniquely results from the guidance mechanisms in hollow-core fibers, scattering and absorption within the bulk glass of the fiber or indeed in the hollow regions be they filled with gaseous or liquid species and scattering from surface roughness. It is our hope that the rigorous analysis of this latter loss mechanism will prove useful to researchers in the field when designing fibers and analysing their loss characteristics. One important distinction with solid-core fibers is that higher order transverse modes in hollow-core fibers inevitably suffer from higher losses, with all these intrinsic contributions higher than that of the fundamental mode, and often significantly so. This differential loss mechanism, which lends itself to further engineering through control of the phase constant of cladding modes, particularly so in antiresonant fibers, is the reason why large core fibers can be made with effective single mode operation.

Turning our attention to extrinsic loss mechanisms, we examined how randomly distributed geometrical changes in the fiber structure along its length scatter light from one mode of the fiber to the other, resulting ultimately in loss and intermodal power coupling. We identified in particular random microbends as imposing practical limitations on the size of the core, though their contribution to loss can in principle be reduced through adequate packaging of the fiber. Lastly, we explored the loss suffered by hollow-core fibers when deployed under a constant radius of curvature as is often the case in applications such as interferometers or compact sensors.

The scaling rules we have identified for the key loss contributions mean that in practical scenarios where microbending (or indeed macrobending when it is a requirement) imposes a limit on the size of the core of the fiber, there exists an optimum core diameter which minimizes the total loss at a given wavelength. Using this, we carried out numerical projections which show that antiresonant fibers of the NANF geometry similar to those reported in the literature (we considered specifically a NANF with 6 sets of nested tubes) can have losses as low as 0.17 dB/km at 1550 nm, marginally higher than pure silica and on par with commercial single mode fibers. At other wavelengths, such fibers are predicted to have, as has been demonstrated already, significantly lower loss than pure silica. We further predict that other antiresonant fiber structures such as our recently reported DNANF, which allow for significant leakage loss reduction, will ultimately outperform any existing optical fiber technology at all wavelengths (with loss potentially as low as ~0.05 dB/km near 1.7μm), and usher in a new era of optical fiber technology and related applications.

Funding. ENF acknowledges support from a Royal Academy of Engineering University Research Fellowship. FP gratefully acknowledges funding from the ERC project Lightpipe (grant number 682724).

Acknowledgments. We are grateful to many colleagues past and present for stimulating discussions and valuable insight: John Hayes, Yong Chen, Thomas Bradley, Hesham Sakr, Natalie Wheeler, Marco Petrovich, Ian Davidson, Austin Taranta, Wei Wang, Reza Sandoghchi and Radan Slavík.

Disclosures.
The authors declare no conflicts of interest.

Data Availability Statement. See OSA's Data Availability Statement policy page for more information.

OSA has identified four common (sometimes overlapping) situations that authors should use as guidance. These are provided as minimal models, and authors should feel free to include any additional details that may be relevant.

References

[1] R. F. Cregan, B. J. Mangan, J. C. Knight, T. A. Birks, P. S. J. Russell, P. J. Roberts, and D. C. Allan, "Single-mode photonic band gap guidance of light in air," Science **285**, 1537–1539 (1999).

[2] E. Yablonovitch, "Inhibited spontaneous emission in solid-state physics and electronics," Phys. Rev. Lett. **58**, 2059–2062 (1987).

[3] S. John, "Strong localization of photons in certain disordered dielectric superlattices," Phys. Rev. Lett. **58**, 2486–2489 (1987).

[4] T. A. Birks, P. J. Roberts, P. S. Russell, D. M. Atkin, and T. J. Shepherd, "Full 2D photonic bandgap in Silica/air structures," Electron. letters **31**, 1941–1943 (1995).

[5] A. Maradudin and A. McGurn, "Out of plane propagation of electromagnetic waves in a two-dimensional periodic dielectric medium," J. Mod. Opt. **41**, 275–284 (1994).

[6] P. Russell, "Photonic crystal fibers," Science **299**, 358–362 (2003).

[7] P. S. J. Russell, "Photonic-crystal fibers," J. Light. Technol. **24**, 4729–4749 (2006).

[8] P. Russell, "Photonic crystal fibers: A historical account," IEEE LEOS Newsl. **21**, 11–15 (2007).

[9] F. Benabid and P. J. Roberts, "Linear and nonlinear optical properties of hollow core photonic crystal fiber," J. Mod. Opt. **58**, 87–124 (2011).

[10] F. Poletti, M. N. Petrovich, and D. J. Richardson, "Hollow-core photonic bandgap fibers: technology and applications," Nanophotonics **2**, 315 (2013).

[11] D. G. Ouzounov, F. R. Ahmad, D. Müller, N. Venkataraman, M. T. Gallagher, M. G. Thomas, J. Silcox, K. W. Koch, and A. L. Gaeta, "Generation of megawatt optical solitons in hollow-core photonic band-gap fibers," Science **301**, 1702–1704 (2003).

[12] A. V. Newkirk, J. M. Mercado, E. A. Lopez, R. A. Correa, and A. Schulzgen, "High power laser delivery using anti-resonant hollow core fiber," in *Photonic Fiber and Crystal Devices: Advances in Materials and Innovations in Device Applications XV,* vol. 11826 S. Yin and R. Guo, eds., International Society for Optics and Photonics (SPIE, 2021), pp. 38 – 41.

[13] J. D. Shephard, A. Urich, R. M. Carter, P. Jaworski, R. R. J. Maier, W. Belardi, F. Yu, W. J. Wadsworth, J. C. Knight, and D. P. Hand, "Silica hollow core microstructured fibers for beam delivery in industrial and medical applications," Front. Phys. **3** (2015).

[14] N. V. Wheeler, Y. Chen, J. R. Hayes, T. D. Bradley, H. C. H. Mulvad, S. A. Mousavi, S. R. Sandoghchi, M. A. Gouveia, E. Numkam, G. T. Jasion, M. B. S. Nawazuddin, P. Horak, S. U. Alam, M. N. Petrovich, F. Poletti, and D. J. Richardson, "Novel hollow core fibers for ultra-high power delivery," in *2017 IEEE Photonics Conference (IPC),* (2017), pp. 279–280.

[15] G. Palma-Vega, F. Beier, F. Stutzki, S. Fabian, T. Schreiber, R. Eberhardt, and A. Tünnermann, "High average power transmission through hollow-core fibers," in *Laser Congress 2018 (ASSL),* (Optica Publishing Group, 2018), p. ATh1A.7.

[16] R.-J. Essiambre, G. J. Foschini, G. Kramer, and P. Winzer, "Capacity limits of transport in fiber-optic networks," Phys. Rev. Lett. **101**, 163901 (2008).

[17] R.-J. Essiambre, G. Kramer, P. Winzer, G. J. Foschini, and B. Goebel, “Capacity limits of optical fiber networks,” J. Light. Technol. **28**, 662 – 701 (2010).

[18] F. Poletti, N. V. Wheeler, M. N. Petrovich, N. Baddela, E. Numkam Fokoua, J. R. Hayes, D. R. Gray, Z. Li, R. Slavik, and D. J. Richardson, “Towards high-capacity fibre-optic communications at the speed of light in vacuum,” Nature Photonics **7**, 279–284 (2013).

[19] B. Zhu, B. J. Mangan, T. Kremp, G. S. Puc, V. Mikhailov, K. Dube, Y. Dulashko, M. Cortes, Y. Liang, K. Marceau, B. Violette, D. Cartsounis, R. Lago, B. Savran, D. Inniss, and D. J. DiGiovanni, “First demonstration of hollow-core-fiber cable for low latency data transmission,” in *2020 Optical Fiber Communications Conference and Exhibition (OFC),* (2020), pp. 1–3.

[20] M. Kuschnerov, B. J. Mangan, K. Gong, V. A. J. M. Sleiffer, M. Herrmann, J. W. Nicholson, J. M. Fini, L. Meng, R. S. Windeler, E. M. Monberg, A. DeSantolo, K. Mukasa, V. Mikhailov, U. Feiste, W. Zhang, and R. Yu, “Transmission of commercial low latency interfaces over hollow-core fiber,” J. Light. Technol. **34**, 314–320 (2016).

[21] Y. Hong, K. R. H. Bottrill, T. D. Bradley, H. Sakr, G. T. Jasion, K. Harrington, F. Poletti, P. Petropoulos, and D. J. Richardson, “Low-latency wdm intensity-modulation and direct-detection transmission over >100 km distances in a hollow core fiber,” Laser & Photonics Rev. **15**, 2100102 (2021).

[22] X. Chen, W. Ding, Y.-Y. Wang, S.-F. Gao, F. Xu, H. Xu, Y.-F. Hong, Y.-Z. Sun, P. Wang, Y.-Q. Lu, and L. Zhang, “High-fidelity, low-latency polarization quantum state transmissions over a hollow-core conjoined-tube fiber at around 800 nm,” Photon. Res. **9**, 460–470 (2021).

[23] M. A. Iqbal, N. Parkin, and A. Lord, “Performance benefits analysis of low-loss hollow core fibre in uwb transmission systems,” in *2021 Conference on Lasers and Electro-Optics (CLEO),* (2021), pp. 1–2.

[24] A. Iqbal, P. Wright, N. Parkin, M. Fake, M. Alonso, S. R. Sandoghchi, and A. Lord, “First demonstration of 400zr dwdm transmission through field deployable hollow-core-fibre cable,” in *Optical Fiber Communication Conference (OFC) 2021,* (Optica Publishing Group, 2021), p. F4C.2.

[25] L. Schares, D. M. Kuchta, and A. F. Benner, “Optics in future data center networks,” in *2010 18th IEEE Symposium on High Performance Interconnects,* (2010), pp. 104–108.

[26] B. J. Mangan, M. Kuschnerov, J. W. Nicholson, J. M. Fini, L. Meng, R. S. Windeler, E. M. Monberg, A. DeSantolo, K. Mukasa, V. Mikhailov, M. Herrmann, and U. Feiste, “First demonstration of hollow-core fiber for intra data center low latency connectivity with a commercial 100gb/s interface,” in *Optical Fiber Communication Conference,* (Optica Publishing Group, 2015), p. M3D.4.

[27] X. Tian, R. Han, L. Wang, G. Lu, and J. Zhan, “Latency critical big data computing in finance,” The J. Finance Data Sci. **1**, 33–41 (2015).

[28] R. Proietti, Z. Cao, C. J. Nitta, Y. Li, and S. J. B. Yoo, “A scalable, low-latency, high-throughput, optical interconnect architecture based on arrayed waveguide grating routers,” J. Light. Technol. **33**, 911–920 (2015).

[29] R. Slavík, “Ultralow thermal sensitivity of phase and propagation delay in hollow core optical fibres,” Sci. Rep. **5** (2015).

[30] E. Numkam Fokoua, M. N. Petrovich, T. Bradley, F. Poletti, D. J. Richardson, and R. Slavík, "How to make the propagation time through an optical fiber fully insensitive to temperature variations," Optica **4**, 659–668 (2017).

[31] V. Dangui, H. K. Kim, M. J. F. Digonnet, and G. S. Kino, "Phase sensitivity to temperature of the fundamental mode in air-guiding photonic-bandgap fibers," Opt. Express **13**, 6669–6684 (2005).

[32] C. Lisdat, G. Grosche, N. Quintin, C. Shi, S. M. F. Raupach, C. Grebing, D. Nicolodi, F. Stefani, A. Al-Masoudi, S. Doerscher, S. Haefner, J. L. Robyr, N. Chiodo, S. Bilicki, E. Bookjans, A. Koczwara, S. Koke, A. Kuhl, F. Wiotte, F. Meynadier, E. Camisard, M. Abgrall, M. Lours, T. Legero, H. Schnatz, U. Sterr, H. Denker, C. Chardonnet, Y. Le Coq, G. Santarelli, A. Amy-Klein, R. Le Targat, J. Lodewyck, O. Lopez, and P. E. Pottie, "A clock network for geodesy and fundamental science," NATURE COMMUNICATIONS **7** (2016).

[33] G. A. Sanders, A. A. Taranta, C. Narayanan, E. Numkam Fokoua, S. A. Mousavi, L. K. Strandjord, M. Smiciklas, T. D. Bradley, J. Hayes, G. T. Jasion, T. Qiu, W. Williams, F. Poletti, and D. N. Payne, "Hollow-core resonator fiber optic gyroscope using nodeless anti-resonant fiber," Opt. Lett. **46**, 46–49 (2021).

[34] F. Couny, F. Benabid, P. J. Roberts, P. S. Light, and M. G. Raymer, "Generation and Photonic Guidance of Multi-Octave Optical-Frequency Combs," Science **318**, 1118–1121 (2007).

[35] B. Debord, F. Amrani, L. Vincetti, F. Gérôme, and F. Benabid, "Hollow-core fiber technology: The rising of "gas photonics"," Fibers **7** (2019).

[36] F. Benabid, G. Bouwmans, J. C. Knight, P. S. J. Russell, and F. Couny, "Ultrahigh efficiency laser wavelength conversion in a gas-filled hollow core photonic crystal fiber by pure stimulated rotational raman scattering in molecular hydrogen," Phys. Rev. Lett. **93**, 123903 (2004).

[37] M. Cassataro, D. Novoa, M. C. Günendi, N. N. Edavalath, M. H. Frosz, J. C. Travers, and P. S. Russell, "Generation of broadband mid-ir and uv light in gas-filled single-ring hollow-core pcf," Opt. Express **25**, 7637–7644 (2017).

[38] T. Balciunas, C. Fourcade-Dutin, G. Fan, T. Witting, A. A. Voronin, A. M. Zheltikov, F. Gerome, G. G. Paulus, A. Baltuska, and F. Benabid, "A strong-field driver in the single-cycle regime based on self-compression in a kagome fibre," Nat. Commun. **6** (2015).

[39] F. Benabid, J. Knight, and P. Russell, "Particle levitation and guidance in hollow-core photonic crystal fiber," Opt. Express **10**, 1195–1203 (2002).

[40] D. S. Bykov, O. A. Schmidt, T. G. Euser, and P. S. J. Russell, "Flying particle sensors in hollow-core photonic crystal fibre," Nat. Photonics **9**, 461–U63 (2015).

[41] D. S. Bykov, S. Xie, R. Zeltner, A. Machnev, G. K. L. Wong, T. G. Euser, and P. S. J. Russell, "Long-range optical trapping and binding of microparticles in hollow-core photonic crystal fibre," LIGHT-SCIENCE & APPLICATIONS **7** (2018).

[42] Y. Tamura, H. Sakuma, K. Morita, M. Suzuki, Y. Yamamoto, K. Shimada, Y. Honma, K. Sohma, T. Fujii, and T. Hasegawa, "The First 0.14-dB/km Loss Optical Fiber and its Impact on Submarine Transmission," J. Light. Technol. **36**, 44–49 (2018).

[43] Marie Wandel, "Attenuation in silica-based optical fibers," Ph.D. thesis, DTU (2006).

[44] S. Sakaguchi and S. ichi Todoroki, "Rayleigh scattering of silica core optical fiber after heat treatment," Appl. Opt. **37**, 7708–7711 (1998).

[45] G. T. Jasion, H. Sakr, J. R. Hayes, S. R. Sandoghchi, L. Hooper, E. N. Fokoua, A. Saljoghei, H. C. Mulvad, M. Alonso, A. Taranta, T. D. Bradley, I. A. Davidson, Y. Chen, D. J. Richardson, and F. Poletti, "0.174 db/km hollow core double nested antiresonant nodeless fiber (dnanf)," in *2022 Optical Fiber Communications Conference and Exhibition (OFC),* (2022), pp. 1–3.

[46] T. P. White, R. C. McPhedran, C. M. de Sterke, L. C. Botten, and M. J. Steel, "Confinement losses in microstructured optical fibers," Opt. Lett. **26**, 1660–1662 (2001).

[47] K. Saitoh and M. Koshiba, "Leakage loss and group velocity dispersion in air-core photonic bandgap fibers," Opt. Express **11**, 3100 (2003).

[48] P. J. Roberts, F. Couny, H. Sabert, B. J. Mangan, T. A. Birks, J. C. Knight, and P. S. J. Russell, "Loss in solid-core photonic crystal fibers due to interface roughness scattering," Opt. Express **13**, 7779 (2005).

[49] P. J. Roberts, F. Couny, H. Sabert, B. J. Mangan, D. P. Williams, L. Farr, M. W. Mason, A. Tomlinson, T. A. Birks, J. C. Knight, and P. St. J. Russell, "Ultimate low loss of hollow-core photonic crystal fibres," Opt. Express **13**, 236 (2005).

[50] B. Temelkuran, S. Hart, G. Benoit, J. Joannopoulos, and Y. Fink, "Wavelength-scalable hollow optical fibres with large photonic bandgaps for co2 laser transmission," NATURE **420**, 650–653 (2002).

[51] F. Benabid, J. C. Knight, G. Antonopoulos, and P. S. J. Russell, "Stimulated raman scattering in hydrogen-filled hollow-core photonic crystal fiber," Science **298**, 399–402 (2002).

[52] F. Poletti, "Nested antiresonant nodeless hollow core fiber," Opt. Express **22**, 23807 (2014).

[53] P. Yeh, A. Yariv, and E. Marom, "Theory of bragg fiber∗," J. Opt. Soc. Am. **68**, 1196–1201 (1978).

[54] S. Johnson, M. Ibanescu, M. Skorobogatiy, O. Weisberg, T. Engeness, M. Soljacic, S. Jacobs, J. Joannopoulos, and Y. Fink, "Low-loss asymptotically single-mode propagation in large-core OmniGuide fibers," Opt. Express **9**, 748 (2001).

[55] C. M. Smith, N. Venkataraman, M. T. Gallagher, D. Muller, J. A. West, N. F. Borrelli, D. C. Allan, and K. W. Koch, "Low-loss hollow-core silica/air photonic bandgap fibre," Nature **424**, 657–659 (2003).

[56] B. Mangan, L. Farr, A. Langford, P. Roberts, D. Williams, F. Couny, M. Lawman, M. Mason, S. Coupland, R. Flea, H. Sabert, T. Birks, J. Knight, and P. Russell, "Low loss (1.7 db/km) hollow core photonic bandgap fiber," in *Optical Fiber Communication Conference, 2004. OFC 2004,* vol. 2 (2004), p. PDP 24.

[57] R. Amezcua-Correa, F. Gérôme, S. G. Leon-Saval, N. G. R. Broderick, T. A. Birks, and J. C. Knight, "Control of surface modes in low loss hollow-core photonic bandgap fibers," Opt. Express **16**, 1142–1149 (2008).

[58] M. N. Petrovich, F. Poletti, A. van Brakel, and D. J. Richardson, “Robustly single mode hollow core photonic bandgap fiber,” Opt. Express **16**, 4337–4346 (2008).

[59] X. Chen, M.-J. Li, N. Venkataraman, M. T. Gallagher, W. A. Wood, A. M. Crowley, J. P. Carberry, L. A. Zenteno, and K. W. Koch, “Highly birefringent hollow-core photonic bandgap fiber,” Opt. Express **12**, 3888–3893 (2004).

[60] N. K. Baddela, M. N. Petrovich, Y. Jung, J. R. Hayes, N. V. Wheeler, D. R. Gray, N. Wong, F. Parmigiani, E. Numkam, J. P. Wooler, F. Poletti, and D. J. Richardson, “First demonstration of a low loss 37-cell hollow core photonic bandgap fiber and its use for data transmission,” in *CLEO: 2013,* (Optica Publishing Group, 2013), p. CTu2K.3.

[61] Y. Jung, V. A. J. M. Sleiffer, N. Baddela, M. N. Petrovich, J. R. Hayes, N. V. Wheeler, D. R. Gray, E. N. Fokoua, J. P. Wooler, N. H.-L. Wong, F. Parmigiani, S. U. Alam, J. Surof, M. Kuschnerov, V. Veljanovski, H. de Waardt, F. Poletti, and D. J. Richardson, “First demonstration of a broadband 37-cell hollow core photonic bandgap fiber and its application to high capacity mode division multiplexing,” in *Optical Fiber Communication Conference/National Fiber Optic Engineers Conference 2013,* (Optica Publishing Group, 2013), p. PDP5A.3.

[62] V. A. J. M. Sleiffer, Y. Jung, N. K. Baddela, J. Surof, M. Kuschnerov, V. Veljanovski, J. R. Hayes, N. V. Wheeler, E. R. N. Fokoua, J. P. Wooler, D. R. Gray, N. H.-L. Wong, F. R. Parmigiani, S.-u. Alam, M. N. Petrovich, F. Poletti, D. J. Richardson, and H. de Waardt, “High capacity mode-division multiplexed optical transmission in a novel 37-cell hollow-core photonic bandgap fiber,” J. Light. Technol. **32**, 854–863 (2014).

[63] J. M. Fini, J. W. Nicholson, B. Mangan, L. Meng, R. S. Windeler, E. M. Monberg, A. DeSantolo, F. V. DiMarcello, and K. Mukasa, “Polarization maintaining single-mode low-loss hollow-core fibres,” NATURE COMMUNICATIONS **5** (2014).

[64] N. V. Wheeler, A. M. Heidt, N. K. Baddela, E. N. Fokoua, J. R. Hayes, S. R. Sandoghchi, F. Poletti, M. N. Petrovich, and D. J. Richardson, “Low-loss and low-bend-sensitivity mid-infrared guidance in a hollow-core–photonic-bandgap fiber,” Opt. Lett. **39**, 295–298 (2014).

[65] “Hollow core photonic crystal fibers,” https://www.nktphotonics.com/products/optical-fibers-and-modules/hollow-core-photonic-crystal-fibers/. [Online; accessed 30-March-2022].

[66] X. Xu, X. Yuan, F. Gao, X. Wang, and N. Song, “Investigation of longitudinal uniformity of the core structure in a hollow-core photonic bandgap fiber,” Opt. Express **29**, 37534–37540 (2021).

[67] F. Couny, F. Benabid, P. J. Roberts, M. T. Burnett, and S. Maier, “Identification of bloch-modes in hollow-core photonic crystal fiber cladding,” Opt. Express **15**, 325–338 (2007).

[68] F. Poletti and E. Numkam Fokoua, “Understanding the physical origin of surface modes and practical rules for their suppression,” in *39th European Conference and Exhibition on Optical Communication (ECOC 2013),* (2013), pp. 1–3.

[69] D. C. Allan, N. F. Borrelli, M. T. Gallagher, D. Müller, C. M. Smith, N. Venkataraman, J. A. West, P. Zhang, and K. W. Koch, “Surface modes and loss in air-core photonic bandgap fibers,” Photonic Cryst. Mater. Devices **5000**, 161 (2003).

[70] J. A. West, C. M. Smith, N. F. Borrelli, D. C. Allan, and K. W. Koch, "Surface modes in air-core photonic band-gap fibers," Opt. Express **12**, 1485–1496 (2004).

[71] P. J. Roberts, D. P. Williams, B. J. Mangan, H. Sabert, F. Couny, W. J. Wadsworth, T. A. Birks, J. C. Knight, and P. S. J. Russell, "Realizing low loss air core photonic crystal fibers by exploiting an antiresonant core surround," Opt. Express **13**, 8277 (2005).

[72] T. A. Birks, P. J. Roberts, F. Couny, H. Sabert, B. J. Mangan, D. P. Williams, L. Farr, M. W. Mason, A. Tomlinson, J. C. Knight, and P. S. J. Russell, "The fundamental limits to the attenuation of hollow-core photonic crystal fibres," Proc. 2005 7th Int. Conf. on Transparent Opt. Networks, ICTON 2005 **1**, 107–110 (2005).

[73] J. Jackle and K. Kawasaki, "Intrinsic roughness of glass surfaces," J. Physics: Condens. Matter **7**, 4351–4358 (1995).

[74] F. Poletti, N. G. R. Broderick, D. J. Richardson, and T. M. Monro, "The effect of core asymmetries on the polarization properties of hollow core photonic bandgap fibers," Opt. Express **13**, 9115–9124 (2005).

[75] N. V. Wheeler, M. N. Petrovich, R. Slavík, N. Baddela, E. Numkam, J. R. Hayes, D. R. Gray, F. Poletti, and D. J. Richardson, "Wide-bandwidth, low-loss, 19-cell hollow core photonic band gap fiber and its potential for low latency data transmission," in *National Fiber Optic Engineers Conference,* (Optica Publishing Group, 2012), p. PDP5A.2.

[76] Y. Chen, Z. Liu, S. R. Sandoghchi, G. T. Jasion, T. D. Bradley, E. Numkam Fokoua, J. R. Hayes, N. V. Wheeler, D. R. Gray, B. J. Mangan, R. Slavík, F. Poletti, M. N. Petrovich, and D. J. Richardson, "Multi-kilometer long, longitudinally uniform hollow core photonic bandgap fibers for broadband low latency data transmission," J. Light. Technol. **34**, 104–113 (2016).

[77] G. T. Jasion, J. S. Shrimpton, Y. Chen, T. Bradley, D. J. Richardson, and F. Poletti, "Microstructure element method (msem): viscous flow model for the virtual draw of microstructured optical fibers," Opt. Express **23**, 312–329 (2015).

[78] G. T. Jasion, E. N. Fokoua, J. S. Shrimpton, D. J. Richardson, and F. Poletti, "Studying the limits of production rate and yield for the volume manufacturing of hollow core photonic band gap fibers," Opt. Express **23**, 32179–32190 (2015).

[79] X. Zhang, S. Gao, Y. Wang, W. Ding, X. Wang, and P. Wang, "7-cell hollow-core photonic bandgap fiber with broad spectral bandwidth and low loss," Opt. Express **27**, 11608–11616 (2019).

[80] M. H. Frosz, J. Nold, T. Weiss, A. Stefani, F. Babic, S. Rammler, and P. S. J. Russell, "Five-ring hollow-core photonic crystal fiber with 1.8 db/km loss," Opt. Lett. **38**, 2215–2217 (2013).

[81] S. Février, B. Beaudou, and P. Viale, "Understanding origin of loss in large pitch hollow-core photonic crystal fibers and their design simplification," Opt. Express **18**, 5142–5150 (2010).

[82] F. Gérôme, R. Jamier, J.-L. Auguste, G. Humbert, and J.-M. Blondy, "Simplified hollow-core photonic crystal fiber," Opt. Lett. **35**, 1157–1159 (2010).

[83] F. Yu, W. J. Wadsworth, and J. C. Knight, "Low loss silica hollow core fibers for 3–4 μm spectral region," Opt. Express **20**, 11153–11158 (2012).

[84] J. R. Hayes, F. Poletti, M. S. Abokhamis, N. V. Wheeler, N. K. Baddela, and D. J. Richardson, “Anti-resonant hexagram hollow core fibers,” Opt. Express **23**, 1289 (2015).

[85] Y. Y. Wang, N. V. Wheeler, F. Couny, P. J. Roberts, and F. Benabid, “Low loss broadband transmission in hypocycloid-core Kagome hollow-core photonic crystal fiber,” Opt. Lett. **36**, 669 (2011).

[86] A. D. Pryamikov, A. S. Biriukov, A. F. Kosolapov, V. G. Plotnichenko, S. L. Semjonov, and E. M. Dianov, “Demonstration of a waveguide regime for a silica hollow - core microstructured optical fiber with a negative curvature of the core boundary in the spectral region > 3.5 μm,” Opt. Express **19**, 1441–1448 (2011).

[87] A. N. Kolyadin, A. F. Kosolapov, A. D. Pryamikov, A. S. Biriukov, V. G. Plotnichenko, and E. M. Dianov, “Light transmission in negative curvature hollow core fiber in extremely high material loss region,” Opt. Express **21**, 9514 (2013).

[88] P. Uebel, M. C. Günendi, M. H. Frosz, G. Ahmed, N. N. Edavalath, J.-M. Ménard, and P. S. Russell, “Broadband robustly single-mode hollow-core PCF by resonant filtering of higher-order modes,” Opt. Lett. **41**, 1961 (2016).

[89] M. B. S. Nawazuddin, N. V. Wheeler, J. R. Hayes, S. R. Sandoghchi, T. D. Bradley, G. T. Jasion, R. Slavík, D. J. Richardson, and F. Poletti, “Lotus-shaped negative curvature hollow core fiber with 10.5 db/km at 1550 nm wavelength,” J. Light. Technol. **36**, 1213–1219 (2018).

[90] J. R. Hayes, S. R. Sandoghchi, T. D. Bradley, Z. Liu, R. Slavík, M. A. Gouveia, N. V. Wheeler, G. Jasion, Y. Chen, E. N. Fokoua, M. N. Petrovich, D. J. Richardson, and F. Poletti, “Antiresonant hollow core fiber with an octave spanning bandwidth for short haul data communications,” J. Light. Technol. **35**, 437–442 (2017).

[91] S. Gao, “Hollow-core conjoined-tube negative-curvature fibre with ultralow loss,” Nat. Commun. **9** (2018).

[92] A. F. Kosolapov, G. K. Alagashev, A. N. Kolyadin, A. D. Pryamikov, A. S. Biryukov, I. A. Bufetov, and E. M. Dianov, “Hollow-core revolver fibre with a double-capillary reflective cladding,” Quantum Electron. **46**, 267–270 (2016).

[93] T. D. Bradley, G. T. Jasion, J. R. Hayes, Y. Chen, L. Hooper, H. Sakr, M. Alonso, A. Taranta, A. Saljoghei, H. C. Mulvad, M. Fake, I. A. K. Davidson, N. V. Wheeler, E. Numkam Fokoua, W. Wang, S. R. Sandoghchi, D. J. Richardson, and F. Poletti, “Antiresonant hollow core fibre with 0.65 db/km attenuation across the c and l telecommunication bands,” in *45th European Conference on Optical Communication (ECOC 2019),* (2019), pp. 1–4.

[94] F. Amrani, J. H. Osorio, F. Delahaye, F. Giovanardi, L. Vincetti, B. Debord, F. Gerome, and F. Benabid, “Low-loss single-mode hybrid-lattice hollow-core photonic-crystal fibre,” LIGHT-SCIENCE & APPLICATIONS **10** (2021).

[95] H. Sakr, T. D. Bradley, G. T. Jasion, E. N. Fokoua, S. R. Sandoghchi, I. A. Davidson, A. Taranta, G. Guerra, W. Shere, Y. Chen, J. R. Hayes, D. J. Richardson, and F. Poletti, “Hollow core nanfs with five nested tubes and record low loss at 850, 1060, 1300 and 1625nm,” in *2021 Optical Fiber Communications Conference and Exhibition (OFC),* (2021), pp. 1–3.

[96] F. Couny, F. Benabid, and P. S. Light, “Large-pitch kagome-structured hollow-core photonic crystal fiber,” Opt. Lett. **31**, 3574–3576 (2006).

[97] F. Poletti, J. R. Hayes, and D. J. Richardson, “Optimising the performances of hollow antiresonant fibres,” in *2011 37th European Conference and Exhibition on Optical Communication,* (2011), pp. 1–3.

[98] C. Wei, R. Joseph Weiblen, C. R. Menyuk, and J. Hu, “Negative curvature fibers,” Adv. Opt. Photonics **9**, 562 (2017).

[99] F. Yu and J. C. Knight, “Negative Curvature Hollow-Core Optical Fiber,” IEEE J. Sel. Top. Quantum Electron. **22**, 146–155 (2016).

[100] W. Ding, Y. Y. Wang, S. F. Gao, M. L. Wang, and P. Wang, “Recent Progress in Low-Loss Hollow-Core Anti-Resonant Fibers and Their Applications,” IEEE J. Sel. Top. Quantum Electron. **26** (2020).

[101] F. Poletti, “Nested antiresonant nodeless hollow core fiber,” Opt. Express **22**, 23807–23828 (2014).

[102] W. Belardi and J. C. Knight, “Hollow antiresonant fibers with reduced attenuation,” Opt. Lett. **39** (2014).

[103] F. Yu, M. Cann, A. Brunton, W. Wadsworth, and J. Knight, “Single-mode solarization-free hollow-core fiber for ultraviolet pulse delivery,” Opt. Express **26**, 10879–10887 (2018).

[104] J. H. Osório, F. Amrani, F. Delahaye, A. Dhaybi, K. Vasko, G. Tessier, F. Giovanardi, L. Vincetti, B. Debord, F. Gérôme, and F. Benabid, “Hollow-core fibers with ultralow loss in the ultraviolet range and sub-thermodynamic equilibrium surface-roughness,” (2021).

[105] X. Zhang, W. Song, Z. Dong, J. Yao, S. Wan, Y. Hou, and P. Wang, “Low loss nested hollow-core anti-resonant fiber at 2 μm spectral range,” Opt. Lett. **47**, 589–592 (2022).

[106] N. V. Wheeler, T. D. Bradley, J. R. Hayes, M. A. Gouveia, S. Liang, Y. Chen, S. R. Sandoghchi, S. M. A. Mousavi, F. Poletti, M. N. Petrovich, and D. J. Richardson, “Low-loss kagome hollow-core fibers operating from the near- to the mid-ir,” Opt. Lett. **42**, 2571–2574 (2017).

[107] F. Yu, P. Song, D. Wu, T. Birks, D. Bird, and J. Knight, “Attenuation limit of silica-based hollow-core fiber at mid-IR wavelengths,” APL Photonics **4** (2019).

[108] I. A. Davidson, S. Rikimi, H. Sakr, G. T. Jasion, T. D. Bradley, N. V. Wheeler, F. Poletti, and D. J. Richardson, “Anti-resonant, mid-infrared silica hollow-core fiber,” in *OSA Advanced Photonics Congress (AP) 2020 (IPR, NP, NOMA, Networks, PVLED, PSC, SPPCom, SOF),* (Optica Publishing Group, 2020), p. SoW1H.7.

[109] G. T. Jasion, T. D. Bradley, K. Harrington, H. Sakr, Y. Chen, E. Numkam Fokoua, I. A. Davidson, A. Taranta, J. R. Hayes, D. J. Richardson, and F. Poletti, “Hollow core nanf with 0.28 db/km attenuation in the c and l bands,” in *2020 Optical Fiber Communications Conference and Exhibition (OFC),* (2020), pp. 1–3.

[110] S. Gao, Y. Wang, W. Ding, Y. Hong, and P. Wang, “Conquering the Rayleigh scattering limit of silica glass fiber at visible wavelengths with a hollow-core fiber approach,” Laser Photonics Rev. **14** (2020).

[111] H. Sakr, Y. Chen, G. T. Jasion, T. D. Bradley, J. R. Hayes, H. C. H. Mulvad, I. A. Davidson, E. Numkam Fokoua, and F. Poletti, “Hollow core optical fibres with comparable attenuation to silica fibres between 600 and 1100 nm,” Nat. Commun. **11**, 1–10 (2020).

[112] A. W. Snyder, "Leaky-ray theory of optical waveguides of circular cross section," Appl. Phys. **4**, 273 – 298 (1974).

[113] A. W. Snyder and J. D. Love, *Optical Waveguide Theory* (Chapman and Hall, 1983).

[114] J. Pomplun, L. Zschiedrich, R. Klose, F. Schmidt, and S. Burger, "Finite element simulation of radiation losses in photonic crystal fibers," physica status solidi (a) **204**, 3822–3837 (2007).

[115] E. A. Marcatili and R. A. Schmeltzer, "Hollow Metallic and Dielectric Waveguides for Long Distance Optical Transmission and Lasers," Bell Syst. Tech. J. **43**, 1783–1809 (1964).

[116] M. Zeisberger and M. A. Schmidt, "Analytic model for the complex effective index of the leaky modes of tube-type anti-resonant hollow core fibers," Sci. Reports **7**, 1–13 (2017).

[117] D. Bird, "Attenuation of model hollow-core, anti-resonant fibres," Opt. Express **25**, 23215 (2017).

[118] G. Li, R. F. Ando, M. Zeisberger, T. Weiss, and M. A. Schmidt, "Interpreting light guidance in antiresonant and photonic bandgap waveguides and fibers by light scattering: analytical model and ultra-low guidance," Opt. Express **30**, 2768–2779 (2022).

[119] T. Grujic, B. T. Kuhlmey, A. Argyros, S. Coen, and C. M. de Sterke, "Solid-core fiber with ultra-wide bandwidth transmission window due to inhibited coupling," Opt. Express **18**, 25556–25566 (2010).

[120] C. W. Hsu, B. Zhen, A. D. Stone, J. D. Joannopoulos, and M. Soljacic, "Bound states in the continuum," NATURE REVIEWS MATERIALS **1** (2016).

[121] B. Debord, A. Amsanpally, M. Chafer, A. Baz, M. Maurel, J. M. Blondy, E. Hugonnot, F. Scol, L. Vincetti, F. Gérôme, and F. Benabid, "Ultralow transmission loss in inhibited-coupling guiding hollow fibers," Optica **4**, 209 (2017).

[122] J. M. Fini, "Suppression of higher-order modes in aircore microstructure fiber designs," in *Conference on Lasers and Electro-Optics/Quantum Electronics and Laser Science Conference and Photonic Applications Systems Technologies,* (Optica Publishing Group, 2006), p. CMM4.

[123] K. Saitoh, N. J. Florous, T. Murao, and M. Koshiba, "Design of photonic band gap fibers with suppressed higher-order modes: Towards the development of effectively single mode large hollow-core fiber platforms," Opt. Express **14**, 7342–7352 (2006).

[124] J. M. Fini, "Aircore microstructure fibers with suppressed higher-order modes," Opt. Express **14**, 11354–11361 (2006).

[125] J. M. Fini, J. W. Nicholson, R. S. Windeler, E. M. Monberg, L. Meng, B. Mangan, A. DeSantolo, and F. V. DiMarcello, "Low-loss hollow-core fibers with improved single-modedness," Opt. Express **21**, 6233–6242 (2013).

[126] B. Debord, M. Alharbi, T. Bradley, C. Fourcade-Dutin, Y. Wang, L. Vincetti, F. Gérôme, and F. Benabid, "Hypocycloid-shaped hollow-core photonic crystal fiber part i: Arc curvature effect on confinement loss," Opt. Express **21**, 28597–28608 (2013).

[127] M. Alharbi, T. Bradley, B. Debord, C. Fourcade-Dutin, D. Ghosh, L. Vincetti, F. Gerome, and F. Benabid, "Hypocycloid-shaped hollow-core photonic crystal fiber Part II: Cladding effect on confinement and bend loss," Opt Express **21**, 28609–28616 (2013).

[128] W. Belardi and J. C. Knight, “Effect of core boundary curvature on the confinement losses of hollow antiresonant fibers,” Opt. Express **21**, 21912 (2013).

[129] E. Numkam Fokoua, D. J. Richardson, and F. Poletti, “Impact of structural distortions on the performance of hollow-core photonic bandgap fibers,” Opt. Express **22**, 2735–2744 (2014).

[130] C. Wei, C. R. Menyuk, and J. Hu, “Impact of Cladding Tubes in Chalcogenide Negative Curvature Fibers,” IEEE Photonics J. **8**, 1–9 (2016).

[131] L. Provino, “Effect of nested elements on avoided crossing between the higher-order core modes and the air-capillary modes in hollow-core antiresonant optical fibers,” Fibers **6** (2018).

[132] M. S. Habib, O. Bang, and M. Bache, “Low-loss hollow-core silica fibers with adjacent nested anti-resonant tubes,” Opt. Express **23**, 17394–17406 (2015).

[133] K. Saitoh, N. A. Mortensen, and M. Koshiba, “Air-core photonic band-gap fibers: the impact of surface modes,” Opt. Express **12**, 394–400 (2004).

[134] H. K. Kim, M. J. F. Digonnet, G. S. Kino, J. Shin, and S. Fan, “Simulations of the effect of the core ring on surface and air-core modes in photonic bandgap fibers,” Opt. Express **12**, 3436–3442 (2004).

[135] R. Amezcua-Correa, N. G. R. Broderick, M. N. Petrovich, F. Poletti, D. J. Richardson, V. Finazzi, and T. M. Monro, “Realistic designs of silica hollow-core photonic bandgap fibers free of surface modes,” in *Optical Fiber Communication Conference and Exposition and The National Fiber Optic Engineers Conference,* (Optica Publishing Group, 2006), p. OFC1.

[136] L. Vincetti and V. Setti, “Confinement loss in kagome and tube lattice fibers: Comparison and analysis,” J. Light. Technol. **30**, 1470–1474 (2012).

[137] L. Vincetti and V. Setti, “Waveguiding mechanism in tube lattice fibers,” Opt. Express, Vol. 18, Issue 22, pp. 23133-23146 **18**, 23133–23146 (2010).

[138] R. F. Ando, A. Hartung, B. Jang, and M. A. Schmidt, “Approximate model for analyzing band structures of single-ring hollow-core anti-resonant fibers,” Opt. Express **27**, 10009 (2019).

[139] L. Vincetti, “Empirical formulas for calculating loss in hollow core tube lattice fibers,” Opt. Express **24**, 10313 (2016).

[140] L. Vincetti and L. Rosa, “A simple analytical model for confinement loss estimation in hollow-core Tube Lattice Fibers,” Opt. Express **27**, 5230 (2019).

[141] A. D. Pryamikov and G. Alagashev, “Features of light leakage from the negative curvature hollow core fibers,” Opt. Eng. **57**, 1 – 7 (2018).

[142] G. T. Jasion, D. J. Richardson, and F. Poletti, “Novel antiresonant hollow core fiber design with ultralow leakage loss using transverse power flow analysis,” in *Optical Fiber Communication Conference (OFC) 2019,* (Optica Publishing Group, 2019), p. Th3E.2.

[143] A. Pryamikov, G. Alagashev, G. Falkovich, and S. Turitsyn, “Light transport and vortex-supported wave-guiding in micro-structured optical fibres,” Sceientific Reports **10** (2020).

[144] F. Urbach, "The long-wavelength edge of photographic sensitivity and of the electronic absorption of solids," Phys. Rev. **92**, 1324–1324 (1953).

[145] J. D. Dow, "Urbach's rule," in *Optical Properties of Highly Transparent Solids,* S. S. Mitra and B. Bendow, eds. (Springer US, Boston, MA, 1975), pp. 131–143.

[146] M. Lines, "Can the minimum attenuation of fused silica be significantly reduced by small compositional variations? i. alkali metal dopants," J. Non-Crystalline Solids **171**, 209–218 (1994).

[147] O. Humbach, H. Fabian, U. Grzesik, U. Haken, and W. Heitmann, "Analysis of oh absorption bands in synthetic silica," J. Non-Crystalline Solids **203**, 19–26 (1996). Optical and Electrical Propertias of Glasses.

[148] M. Bredol, D. Leers, L. Bosselaar, and M. Hutjens, "Improved model for oh absorption in optical fibers," J. Light. Technol. **8**, 1536–1540 (1990).

[149] N. Frateschi and A. De Castro, "Perturbation theory for the wave equation and the "effective refractive index" approach," IEEE J. Quantum Electron. **22**, 12–15 (1986).

[150] K. Zhang and D. Li, *Electromagnetic Theory for Microwaves and Optoelectronics* (Springer, 2008).

[151] A. Villeneuve, "Orthogonality relationships for waveguides and cavities with inhomogeneous anisotropic media," IRE Transactions on Microw. Theory Tech. **7**, 441–446 (1959).

[152] P. McIsaac, "Mode orthogonality in reciprocal and nonreciprocal waveguides," IEEE Transactions on Microw. Theory Tech. **39**, 1808–1816 (1991).

[153] B. Z. Katsenelenbaum, L. Mercader del Rio, M. Pereyaslavets, M. Sorolla Ayzaand, and M. Thumm, *Theory of Nonuniform Waveguides: the cross-section method*, Electromagnetic Waves (Institution of Engineering and Technology, 1998).

[154] D. Wu, F. Yu, and M. Liao, "Understanding the material loss of anti-resonant hollow-core fibers," Opt. Express **28**, 11840–11851 (2020).

[155] E. Numkam Fokoua, V. Michaud-Belleau, J. Genest, R. Slavík, and F. Poletti, "Theoretical analysis of backscattering in hollow-core antiresonant fibers," APL Photonics **6**, 096106 (2021).

[156] "Transmission and extinction of suprasil glasses," https://www.heraeus.com/en/hca/fused_silica_quartz_knowledge_base_1/t_calc_1/transmission_calc_opt/transmission_calculator_opt.html?selection=suprasil_3001_3002_300&rangeX=120%2C4500&chartIndex=2&thickness=10. [Online; accessed 30-March-2022].

[157] N. V. Wheeler, M. N. Petrovich, N. K. Baddela, J. R. Hayes, E. N. Fokoua, F. Poletti, and D. J. Richardson, "Gas absorption between 1.8 and 2.1 μm in low loss (5.2 db/km) hc-pbgf," in *2012 Conference on Lasers and Electro-Optics (CLEO),* (2012), pp. 1–2.

[158] J. K. Lyngsø, B. J. Mangan, C. Jakobsen, and P. J. Roberts, "7-cell core hollow-core photonic crystal fibers with low loss in the spectral region around 2 μm," Opt. Express **17**, 23468–23473 (2009).

[159] S. Rikimi, Y. Chen, M. C. Partridge, T. D. Bradley, I. A. K. Davidson, A. A. Taranta, F. Poletti, M. N. Petrovich, D. J. Richardson, and N. V. Wheeler, "Growth of ammonium chloride on cleaved end-facets of hollow core fibers," in *2020 Conference on Lasers and Electro-Optics (CLEO),* (2020), pp. 1–2.

[160] S. Rikimi, Y. Chen, M. C. Partridge, I. A. Davidson, G. T. Jasion, T. D. Bradley, A. A. Taranta, F. Poletti, M. N. Petrovich, D. J. Richardson, and N. V. Wheeler, "Pressure in as-drawn hollow core fibers," in *OSA Advanced Photonics Congress (AP) 2020 (IPR, NP, NOMA, Networks, PVLED, PSC, SPPCom, SOF),* (Optica Publishing Group, 2020), p. SoW1H.4.

[161] S. Rikimi, Y. Chen, T. W. Kelly, I. Davidson, G. Jasion, M. Partridge, K. Harrington, T. Bradley, A. Taranta, F. Poletti, M. Petrovich, D. J. Richardson, and N. V. Wheeler, "Internal gas composition and pressure in as-drawn hollow core optical fibers," J. Light. Technol. pp. 1–1 (2022).

[162] I. Gris-Sanchez and J. C. Knight, "Time-dependent degradation of photonic crystal fiber attenuation around oh absorption wavelengths," J. Light. Technol. **30**, 3597–3602 (2012).

[163] A. Bucholtz, "Rayleigh-scattering calculations for the terrestrial atmosphere," Appl. Opt. **34**, 2765 (1995).

[164] D. Marcuse, "Radiation Losses of the He11 Mode of a Fiber With Sinusoidally Perturbed Core Boundary." Appl. Opt. **14**, 3021–3025 (1975).

[165] D. Marcuse, *Theory of Dielectric Optical Waveguides* (Academic Press, 1991), 2nd ed.

[166] S. G. Johnson, M. Ibanescu, M. A. Skorobogatiy, O. Weisberg, J. D. Joannopoulos, and Y. Fink, "Perturbation theory for Maxwell's equations with shifting material boundaries," Phys. Rev. E - Stat. Physics, Plasmas, Fluids, Relat. Interdiscip. Top. **65**, 1–7 (2002).

[167] A. Yariv, "Coupled-mode theory for guided-wave optics," IEEE J. Quantum Electron. **9**, 919–933 (1973).

[168] M. Skorobogatiy, S. Jacobs, S. Johnson, and Y. Fink, "Geometric variations in high index-contrast waveguides, coupled mode theory in curvilinear coordinates," Opt. Express **10**, 1227 (2002).

[169] W.-P. Huang and J. Mu, "Complex coupled-mode theory for optical waveguides," Opt. Express **17**, 19134–19152 (2009).

[170] W. Chen, Z. Xiong, J. Xu, and Y. Chen, "Generalized coupled-mode formalism in reciprocal waveguides with gain, loss, anisotropy, or bianisotropy," Phys. Rev. B **99**, 195307 (2019).

[171] H. Haus, W. Huang, S. Kawakami, and N. Whitaker, "Coupled-mode theory of optical waveguides," J. Light. Technol. **5**, 16–23 (1987).

[172] D. Marcuse, "Coupled-mode theory for anisotropic optical waveguides," The Bell Syst. Tech. J. **54**, 985–995 (1975).

[173] W.-P. Huang, "Coupled-mode theory for optical waveguides: an overview," J. Opt. Soc. Am. A **11**, 963–983 (1994).

[174] E. Numkam Fokoua, F. Poletti, and D. J. Richardson, "Analysis of light scattering from surface roughness in hollow-core photonic bandgap fibers," Eur. Conf. on Opt. Commun. ECOC **20**, 3783–3789 (2012).

[175] A. W. Snyder, "Radiation Losses Due to Variations of Radius on Dielectric or Optical Fibers," IEEE Transactions on Microw. Theory Tech. **18**, 608–615 (1970).

[176] I. A. White, "Radiation From Bends In Optical-waveguides - Volume-current Method," IEE Journal on Microwaves Optics and Acoustics **3**, 186–188 (1979).

[177] M. Kuznetsov and H. A. Haus, "Radiation Loss In Dielectric Waveguide Structures By The Volume Current Method," IEEE Journal of Quantum Electronics **19**, 1505–1514 (1983).

[178] J. P. R. Lacey and F. P. Payne, "Radiation loss from planar waveguides with random wall imperfections," IEE Proc. **137**, 282–288 (1990).

[179] S. G. Johnson, M. L. Povinelli, M. Soljačić, A. Karalis, S. Jacobs, and J. D. Joannopoulos, "Roughness losses and volume-current methods in photonic-crystal waveguides," Appl. Phys. B: Lasers Opt. **81**, 283–293 (2005).

[180] C. H. Papas, *Theory of Electromagnetic Wave Propagation* (Dover Publications, Inc., New York, 1988).

[181] T. Sarlat, A. Lelarge, E. Søndergård, and D. Vandembroucq, "Frozen capillary waves on glass surfaces: An AFM study," Eur. Phys. J. B **54**, 121–126 (2006).

[182] M. C. Phan-Huy, J. M. Moison, J. A. Levenson, S. Richard, G. Mélin, M. Douay, and Y. Quiquempois, "Surface Roughness and Light Scattering in a Small Effective Area Microstructured Fiber," J. Light. Technol. **27**, 1597–1604 (2009).

[183] C. Brun, X. Buet, B. Bresson, M. S. Capelle, M. Ciccotti, A. Ghomari, P. Lecomte, J. P. Roger, M. N. Petrovich, F. Poletti, D. J. Richardson, D. Vandembroucq, and G. Tessier, "Picometer-scale surface roughness measurements inside hollow glass fibres," Opt. Express **22**, 29554–29567 (2014).

[184] X. Buet, C. Brun, B. Bresson, M. Ciccotti, M. N. Petrovich, F. Poletti, D. J. Richardson, D. Vandembroucq, and G. Tessier, "Picometer-scale surface roughness measurements inside hollow glass fibres," Conf. on Lasers Electro-Optics Eur. - Tech. Dig. **2015-Augus**, 4351–4358 (2015).

[185] X. Buet, C. Brun, J. Gâteau, B. Bresson, S. R. Sandoghchi, E. N. Fokoua, M. Petrovich, F. Poletti, D. Richardson, D. Vandembroucq, and G. Tessier, "Nondestructive measurement of the roughness of the inner surface of hollow core-photonic bandgap fibers," Opt. Lett. **41**, 5086 (2016).

[186] B. Bresson, C. Brun, X. Buet, Y. Chen, M. Ciccotti, J. Gâteau, G. Jasion, M. N. Petrovich, F. Poletti, D. J. Richardson, S. R. Sandoghchi, G. Tessier, B. Tyukodi, and D. Vandembroucq, "Anisotropic Superattenuation of Capillary Waves on Driven Glass Interfaces," Phys. Rev. Lett. **119**, 1–6 (2017).

[187] V. Dangui, M. J. Digonnet, and G. S. Kino, "Modeling of the propagation loss and backscattering in air-core photonic-bandgap fibers," J. Light. Technol. **27**, 3783–3789 (2009).

[188] E. Numkam Fokoua, N. Wong, D. J. Richardson, and F. Poletti, "Analysis and comparison of intermodal coupling coefficient of standard and hollow core few moded fibres," in *2015 European Conference on Optical Communication (ECOC),* (2015), pp. 1–3.

[189] E. Numkam Fokoua, Y. Chen, D. J. Richardson, and F. Poletti, "Microbending effects in hollow-core photonic bandgap fibers," in *ECOC 2016; 42nd European Conference on Optical Communication,* (2016), pp. 1–3.

[190] Y. Chen, N. V. Wheeler, N. K. Baddela, J. R. Hayes, S. R. Sandoghchi, E. N. Fokoua, M. Li, F. Poletti, M. N. Petrovich, and D. J. Richardson, "Understanding wavelength scaling in 19-cell core hollow-core photonic bandgap fibers," in *Optical Fiber Communication Conference,* (Optica Publishing Group, 2014), p. M2F.4.

[191] P. S. J. Russell, P. J. Roberts, and P. Willians, "Photonic bandgap optical waveguide with antiresonant core boundary," (U.S. Patent 7,346,249 B2, Mar 2008).

[192] E. Numkam Fokoua, S. R. Sandoghchi, Y. Chen, G. T. Jasion, N. V. Wheeler, N. K. Baddela, J. R. Hayes, M. N. Petrovich, D. J. Richardson, and F. Poletti, "Accurate modelling of fabricated hollow-core photonic bandgap fibers," Opt. Express **23**, 23117–23132 (2015).

[193] A. Nespola, S. Straullu, T. D. Bradley, H. C. Mulvad, J. R. Hayes, G. T. Jasion, M. A. Gouveia, S. R. Sandoghchi, S. Bawn, F. Forghieri, D. J. Richardson, F. Poletti, and P. Poggiolini, "Record pm-16qam and pm-qpsk transmission distance (125 and 340 km) over hollow-core-fiber," in *45th European Conference on Optical Communication (ECOC 2019),* (2019), pp. 1–4.

[194] A. Nespola, S. Straullu, T. D. Bradley, K. Harrington, H. Sakr, G. T. Jasion, E. Numkam Fokoua, Y. Jung, Y. Chen, J. R. Hayes, F. Forghieri, D. J. Richardson, F. Poletti, G. Bosco, and P. Poggiolini, "Transmission of 61 c-band channels over record distance of hollow-core-fiber with l-band interferers," J. Light. Technol. **39**, 813–820 (2021).

[195] A. Nespola, S. R. Sandoghchi, L. Hooper, M. Alonso, T. D. Bradley, H. Sakr, G. T. Jasion, E. Numkam Fokoua, S. Straullu, F. Garrisi, G. Bosco, A. Carena, A. M. Rosa Brusin, Y. Chen, J. R. Hayes, F. Forghieri, D. J. Richardson, F. Poletti, and P. Poggiolini, "Ultra-long-haul wdm transmission in a reduced intermodal interference nanf hollow-core fiber," in *2021 Optical Fiber Communications Conference and Exhibition (OFC),* (2021), pp. 1–3.

[196] P. Poggiolini and F. Poletti, "Opportunities and challenges for long-distance transmission in hollow-core fibres," J. Light. Technol. **40**, 1605–1616 (2022).

[197] G. Goubau, "On the excitation of surface waves," Proc. IRE **40**, 865–868 (1952).

[198] M. Nakazawa, "Rayleigh Backscattering Theory for Single-Mode Optical Fibers." J. Opt. Soc. Am. **73**, 1175–1180 (1983).

[199] M. R. Henderson, S. Afshar V., A. D. Greentree, and T. M. Monro, "Dipole emitters in fiber: interface effects, collection efficiency and optimization," Opt. Express **19**, 16182 (2011).

[200] A. Taranta, E. Numkam Fokoua, S. Abokhamis Mousavi, J. R. Hayes, T. D. Bradley, G. T. Jasion, and F. Poletti, "Exceptional polarization purity in antiresonant hollow-core optical fibres," Nat. Photonics **14**, 504–510 (2020).

[201] J. Nicholson, L. Meng, J. Fini, R. Windeler, A. DeSantolo, E. Monberg, F. DiMarcello, Y. Dulashko, M. Hassan, and R. Ortiz, "Measuring higher-order modes in a low-loss, hollow-core, photonic-bandgap fiber," Opt. Express **20**, 20494–20505 (2012).

[202] T. D. Bradley, N. V. Wheeler, G. T. Jasion, D. Gray, J. Hayes, M. A. Gouveia, S. R. Sandoghchi, Y. Chen, F. Poletti, D. Richardson, and M. Petrovich, "Modal content in hypocycloid kagomé hollow core photonic crystal fibers," Opt. Express **24**, 15798–15812 (2016).

[203] W. Shere, G. T. Jasion, E. N. Fokoua, and F. Poletti, "Design rules for multi-mode anti-resonant hollow-core fibres," in *Optical Fiber Communication Conference (OFC) 2021,* (Optica Publishing Group, 2021), p. F4C.4.

[204] C. Goel and S. Yoo, "Multimode nested antiresonant hollow core fiber," J. Light. Technol. **39**, 6592–6598 (2021).

[205] M. S. Habib, E. Antonio-Lopez, C. Markos, A. Schülzgen, and R. Amezcua-Correa, "Single mode, low-loss 5-tube nested hollow-core anti-resonant fiber," in *Optical Fiber Communication Conference (OFC) 2019,* (Optica Publishing Group, 2019), p. W2A.12.

[206] W. B. Gardner, "Microbending Loss in Optical Fibers," Bell Syst. Tech. J. **54**, 457–465 (1975).

[207] D. Gloge, "Optical-Fiber Packaging and Its Influence on Fiber Straightness and Loss," Bell Syst. Tech. J. **54**, 245–262 (1975).

[208] D. Marcuse, "Microbending Losses of Single-Mode Step-Index and Multimode Fibers," The Bell Syst. Tech. J. (1976).

[209] R. Olshansky, "Mode coupling effects in graded-index optical fibers," Appl. Opt. **14**, 935–945 (1975).

[210] M. Ohashi, K. ichi Kitayama, and S. Seikai, "Mode coupling effects in a graded-index fiber cable," Appl. Opt. **20**, 2433–2438 (1981).

[211] T. Hayashi, T. Sasaki, E. Sasaoka, K. Saitoh, and M. Koshiba, "Physical interpretation of intercore crosstalk in multicore fiber: effects of macrobend, structure fluctuation, and microbend," Opt. Express **21**, 5401–5412 (2013).

[212] P. Sillard, D. Molin, M. Bigot-Astruc, K. De Jongh, F. Achten, J. E. Antonio-Lopez, and R. Amezcua-Correa, "Micro-bend-Resistant Low-Differential-Mode-Group-Delay Few-Mode Fibers," J. Light. Technol. **35**, 734–740 (2017).

[213] John A Jay, "An overview of Macrobending and Microbending of Optical Fibers," Corning White paper, doi:10.1117/3.1445658.ch5 (2017).

[214] H. F. Taylor, "Power Loss at Directional Change in Dielectric Waveguides," Appl. Opt. **13**, 642 (1974).

[215] H. F. Taylor, "Losses at corner bends in dielectric waveguides," Appl. Opt. **16**, 711 (1977).

[216] H. F. Taylor, "Bending Effects in Optical Fibers," J. Light. Technol. **LT-2**, 617–628 (1984).

[217] K. Petermann, "Microbending loss in monomode fibres," Electron. Lett. **12**, 107–109(2) (1976).

[218] K. Petermann, "Fundamental mode microbending loss in graded-index and W fibres," Opt. Quantum Electron. **9**, 167–175 (1977).

[219] K. Petermann and R. Kühne, "Upper and Lower Limits for the Microbending Loss in Arbitrary Single-Mode Fibers," J. Light. Technol. **4**, 2–7 (1986).

[220] M. Artiglia, G. Coppa, and P. di Vita, “New analysis of microbending losses in single-mode fibres,” Electron. Lett. **22**, 623 – 625 (1986).

[221] Robert Olshansky, “Distortion Losses in Cabled Optical Fibers,” Appl. Opt. **14**, 1974–1975 (1975).

[222] J. I. Sakai and T. Kimura, “Practical Microbending Loss Formula for SingleMode Optical Fibers,” IEEE J. Quantum Electron. **15**, 497–500 (1979).

[223] J. I. Sakai, “Microbending Loss Evaluation in Arbitrary-lndex Singlemode Optical Fibers. Part II: Effects of Core Index Profiles,” IEEE J. Quantum Electron. **16**, 44–49 (1980).

[224] J.-i. Sakai, “Microbending Loss Evaluation in Arbitrary-Index,” IEEE J. Quantum Electron. **QE-16**, 36–44 (1980).

[225] Z. Várallyay, T. Mihálffy, S. Bilicz, G. Varga, and K. Mukasa, “Microbending loss properties of different fiber designs,” in *Optical Fiber Communication Conference (OFC) 2021,* (Optica Publishing Group, 2021), p. Th1A.49.

[226] S. H. K.J. Blow, N.J. Doran, “Power spectrum of microbends in monomode optical fibres,” Electron. Lett. **18**, 448–450(2) (1982).

[227] S. Hornung, N. J. Doran, and R. Allen, “Monomode fibre microbending loss measurements and their interpretation,” Opt. Quantum Electron. **14**, 359–362 (1982).

[228] D. Marcuse, “Coupled power equations for lossy fibers,” Appl. Opt. **17**, 3232–3237 (1978).

[229] P. Sillard, S. Richard, L.-A. de Montmorillon, and M. Bigot-Astruc, “Micro-bend losses of trench-assisted single-mode fibers,” in *36th European Conference and Exhibition on Optical Communication,* (2010), pp. 1–3.

[230] T. Yabuta, C. Tanaka, N. Yoshizawa, and K. Ishihara, “Structural analysis of jacketed optical fiber under lateral pressure,” J. Light. Technol. **1**, 529–535 (1983).

[231] F. Cocchini, “The lateral rigidity of double-coated optical fibers,” J. Light. Technol. **13**, 1706–1710 (1995).

[232] K. Okamoto, *Fundamentals of Optical Waveguides* (Academic Press, Burlington, 2006), 2nd ed.

[233] M. Skorobogatiy, S. G. Johnson, S. A. Jacobs, and Y. Fink, “Dielectric profile variations in high-index-contrast waveguides, coupled mode theory, and perturbation expansions,” Phys. Rev. E - Stat. Physics, Plasmas, Fluids, Relat. Interdiscip. Top. **67**, 11 (2003).

[234] F. Melli, F. Giovanardi, L. Rosa, and L. Vincetti, “Non-idealities in hollow core inhibited coupling fibers,” Int. Conf. on Transparent Opt. Networks **2020-July**, 4–7 (2020).

[235] M. Skorobogatiy, M. Ibanescu, S. G. Johnson, O. Weisberg, T. D. Engeness, M. Soljacˇic´, S. A. Jacobs, and Y. Fink, “Analysis of general geometric scaling perturbations in a transmitting waveguide: fundamental connection between polarization-mode dispersion and group-velocity dispersion,” J. Opt. Soc. Am. B **19**, 2867–2875 (2002).

[236] M. Heiblum and J. Harris, “Analysis of curved optical waveguides by conformal transformation,” Quantum Electron. IEEE J. **11**, 75–83 (1975).

[237] W. A. Gambling, H. Matsumura, and C. M. Ragdale, “Curvature and microbending losses in single-mode optical fibres,” Opt. Quantum Electron. **11**, 43–59 (1979).

[238] D. Marcuse, "Influence of curvature on the losses of doubly clad fibers," Appl. Opt. **21**, 4208–4213 (1982).

[239] R. T. Schermer and J. H. Cole, "Improved Bend Loss Formula Verified for Optical Fiber by Simulation and Experiment," IEEE J. Quantum Electron. **43**, 899–909 (2007).

[240] J. B. Pendry, D. Schurig, and D. R. Smith, "Controlling electromagnetic fields," Science **312**, 1780–1782 (2006).

[241] Z. Han, P. Zhang, and S. I. Bozhevolnyi, "Calculation of bending losses for highly confined modes of optical waveguides with transformation optics," Opt. Lett. **38**, 1778–1780 (2013).

[242] M. Bigot-Astruc, F. Gooijer, N. Montaigne, and P. Sillard, "Trench-assisted profiles for large-effective-area single-mode fibers," in *2008 34th European Conference on Optical Communication,* (2008), pp. 1–2.

[243] M.-J. Li, P. Tandon, D. C. Bookbinder, S. R. Bickham, K. Wilbert, J. S. Abbott, and D. Nolan, "Designs of bend-insensitive multimode fibers," in *2011 Optical Fiber Communication Conference and Exposition and the National Fiber Optic Engineers Conference,* (2011), pp. 1–3.

[244] M. Skorobogatiy, K. Saitoh, and M. Koshiba, "Full-vectorial coupled mode theory for the evaluation of macro-bending loss in multimode fibers: application to the hollow-core photonic bandgap fibers," Opt. Express, Vol. 16, Issue 19, pp. 14945-14953 **16**, 14945–14953 (2008).

[245] M. H. Frosz, P. Roth, M. C. Günendi, and P. S. Russell, "Analytical formulation for the bend loss in single-ring hollow-core photonic crystal fibers," Photon. Res. **5**, 88–91 (2017).

[246] J. Olszewski, M. Szpulak, and W. Urbanczyk, "Effect of coupling between fundamental and cladding modes on bending losses in photonic crystal fibers," Opt. Express, Vol. 13, Issue 16, pp. 6015-6022 **13**, 6015–6022 (2005).

[247] G. K. Alagashev, A. D. Pryamikov, A. F. Kosolapov, A. N. Kolyadin, A. Y. Lukovkin, and A. S. Biriukov, "Impact of geometrical parameters on the optical properties of negative curvature hollow-core fibers," Laser Phys. **25**, 055101 (2015).

[248] R. M. Carter, F. Yu, W. J. Wadsworth, J. D. Shephard, T. Birks, J. C. Knight, and D. P. Hand, "Measurement of resonant bend loss in anti-resonant hollow core optical fiber," Opt. Express **25**, 20612–20621 (2017).

[249] V. Setti, L. Vincetti, and A. Argyros, "Flexible tube lattice fibers for terahertz applications," Opt. Express **21**, 3388 (2013).

[250] Y. Wang and W. Chang, "Understanding bending-induced loss and bending-enhanced higher-order mode suppression in negative curvature fibers," Opt. Express **29**, 23622–23636 (2021).

[251] T. P. Hansen, J. Broeng, C. Jakobsen, G. Vienne, H. R. Simonsen, M. D. Nielsen, P. M. W. Skovgaard, J. R. Folkenberg, and A. Bjarklev, "Air-guiding photonic bandgap fibers: Spectral properties, macrobending loss, and practical handling," J. Light. Technol. **22**, 11 (2004).

[252] Y. Chen, S. R. Sandoghchi, E. Numkam, T. D. Bradley, J. R. Hayes, N. V. Wheeler, G. Jasion, D. R. Gray, F. Poletti, M. N. Petrovich, and D. J. Richardson, "Detailed study of macrobending effects in a wide transmission bandwidth hollow-core photonic bandgap fiber," in *Micro-Structured and Specialty Optical Fibres IV,* vol. 9886 K. Kalli and A. Mendez, eds., International Society for Optics and Photonics (SPIE, 2016), pp. 141 – 146.

[253] C. Wei, C. R. Menyuk, and J. Hu, "Bending-induced mode non-degeneracy and coupling in chalcogenide negative curvature fibers," Opt. Express **24**, 12228 (2016).

[254] S. A. Mousavi *et al.*, "Bend-induced propagation effects in hollow-core antiresonant fibers," To be published in 2022.

[255] K. Nagayama, M. Kakui, M. Matsui, T. Saitoh, and Y. Chigusa, "Ultra-low-loss (0.1484 db/km) pure silica core fibre and extension of transmission distance," Electron. Lett. **38**, 1168–1169(1) (2002).

[256] H. C. Mulvad, S. mohammad Abokhamis Mousavi, V. Zuba, L. Xu, H. Sakr, T. Bradley, J. Hayes, G. Jasion, E. N. Fokoua, A. Taranta, S. ul Alam, D. Richardson, and F. Poletti, "Kilometre-scale, kilowatt average power, single-mode laser delivery through hollow core fibre: overcoming nonlinear limits of glass fibre," accepted for publication in Nature Photonics 2022, Preprint available at Research Square [https://doi.org/10.21203/rs.3.rs-1004375/v1] (2021).